

MINISTRY OF EDUCATION



**THE ANNALS OF
“DUNAREA DE JOS”
UNIVERSITY OF GALATI**

Fascicle IX
METALLURGY AND MATERIALS SCIENCE

YEAR XLII (XLVII)
March 2024, no. 1

ISSN 2668-4748; e-ISSN 2668-4756



2024
GALATI UNIVERSITY PRESS

EDITORIAL BOARD

EDITOR-IN-CHIEF

Assist. Prof. Marius BODOR – “Dunarea de Jos” University of Galati, Romania

SCIENTIFIC ADVISORY COMMITTEE

Assist. Prof. Dragos-Cristian ACHITEI – “Gheorghe Asachi” Technical University Iasi, Romania

Assoc. Prof. Stefan BALTA – “Dunarea de Jos” University of Galati, Romania

Assist. Prof. Chenna Rao BORRA – Indian Institute of Technology, Republic of India

Prof. Acad. Ion BOSTAN – Technical University of Moldova, the Republic of Moldova

Researcher Mihai BOTAN – The National Institute of Aerospace Research, Romania

Prof. Vasile BRATU – Valahia University of Targoviste, Romania

Prof. Francisco Manuel BRAZ FERNANDES – New University of Lisbon Caparica, Portugal

Prof. Bart Van der BRUGGEN – Katholieke Universiteit Leuven, Belgium

Prof. Acad. Valeriu CANTSER – Academy of the Republic of Moldova

Prof. Valeriu DULGHERU – Technical University of Moldova, the Republic of Moldova

Prof. Gheorghe GURAU – “Dunarea de Jos” University of Galati, Romania

Assist. Prof. Gina Genoveva ISTRATE – “Dunarea de Jos” University of Galati, Romania

Assist. Prof. Nora JULLOK – Universiti Malaysia Perlis, Malaysia

Prof. Rodrigo MARTINS – NOVA University of Lisbon, Portugal

Prof. Strul MOISA – Ben Gurion University of the Negev, Israel

Assist. Prof. Priyanka MONDAL – CSIR-Central Glass and Ceramic Research Institute, India

Prof. Daniel MUNTEANU – “Transilvania” University of Brasov, Romania

Assoc. Prof. Alina MURESAN – “Dunarea de Jos” University of Galati, Romania

Prof. Maria NICOLAE – Politehnica University Bucuresti, Romania

Assist. Prof. Manuela-Cristina PERJU – “Gheorghe Asachi” Technical University Iasi, Romania

Prof. Cristian PREDESCU – Politehnica University of Bucuresti, Romania

Prof. Iulian RIPOSAN – Politehnica University of Bucuresti, Romania

Prof. Antonio de SAJA – University of Valladolid, Spain

Assist. Prof. Rafael M. SANTOS – University of Guelph, Canada

Prof. Ion SANDU – “Al. I. Cuza” University of Iasi, Romania

Prof. Mircea Horia TIHEREAN – “Transilvania” University of Brasov, Romania

Prof. Ioan VIDA-SIMITI – Technical University of Cluj Napoca, Romania

Assoc. Prof. Petrica VIZUREANU – “Gheorghe Asachi” Technical University Iasi, Romania

EDITING SECRETARY

Assist. Prof. Marius BODOR – “Dunarea de Jos” University of Galati, Romania

Assist. Nicoleta BOGATU – “Dunarea de Jos” University of Galati, Romania

Assist. Prof. Eliza DANAILA – “Dunarea de Jos” University of Galati, Romania

Assist. Prof. Florin Bogdan MARIN – “Dunarea de Jos” University of Galati, Romania

Assist. Prof. Mihaela MARIN – “Dunarea de Jos” University of Galati, Romania



Table of Contents

1. Costel UNGUREANU, Adrian PRESURĂ, Radu BOSOANCĂ, Andreea MÂNDRU, Silviu PERIJOC, Victor MIHAI, George COTOC - Review on Ship Shaped Fish Farms	5
2. Costel UNGUREANU, Adrian PRESURĂ, Radu BOSOANCĂ, Andreea MÂNDRU, Silviu PERIJOC, Victor MIHAI, George COTOC - Studies on the Conversion of a River Cargo Barge into a Floating Fish Farm	9
3. Andreea Elena ONACHE (VIJAN), Alina Maria IANCU, Adriana-Gabriela SCHIOPU, Mihai OPROESCU, Ilie STELIAN - An Overview on ZnO Reinforced Composites	18
4. Emad Toma KARASH, Amenah Faris HAMID - Comparison of the Difference in Temperature Distribution on the Surface of Two Aluminum Alloys Welded by Friction Stir Welding in Different Regions at Different Linear and Rotational Speeds	25
5. Simona STANCA - The Future of Construction from a Sustainable Materials Perspective	37
6. Simona BOICIUC - Studies and Research on the Hardening of Some Industrial Benchmarks Through Laser Cladding	43
7. Cristian ȘTEFĂNESCU, Petrică ALEXANDRU, Gheorghe GURĂU - Mathematical Modeling of the CuSn12 Alloy Sintering Process	49



THE ANNALS OF "DUNAREA DE JOS" UNIVERSITY OF GALATI
FASCICLE IX. METALLURGY AND MATERIALS SCIENCE
Nº. 1 - 2024, ISSN 2668-4748; e-ISSN 2668-4756
Volume DOI: <https://doi.org/10.35219/mms.2024.1>

REVIEW ON SHIP SHAPED FISH FARMS

**Costel UNGUREANU, Adrian PRESURĂ, Radu BOSOANĂ,
Andreea MÂNDRU, Silviu PERIJOC, Victor MIHAI, George COTOC**
"Dunarea de Jos" University of Galati, Naval Architecture Faculty, 47th Domneasă Street, Galati, Romania
e-mail: costel.ungureanu@ugal.ro

ABSTRACT

This paper presents a review on ship shaped fish farms as a first step in the research and developing of a modular floating aquaculture platform based on inland river cargo barge design to be exploited under biosecurity and sustainability conditions in the Lower Danube region, aligned with the current sustainable development strategies of the blue economy outlined by the European Union.

KEYWORDS: fish farm, aquaculture platform, river barge

1. Political context

The present paper supports and promotes fundamental, multidisciplinary, interdisciplinary and transdisciplinary scientific research and started from four current strategic development directions of the European Union:

- European Green Deal
- Strategy for a Blue Economy
- "Farm to Fork" Strategy
- Common Fisheries Policy

The European Green Deal is the European Union's (EU) new growth strategy and is a set of strategies with the main goal of the EU green transition toward climate neutrality by 2050 [1]. The interconnected transition directions like climate, transport, environment, industry, energy, agriculture are leading to the transformation of the EU member states economies into modern and sustainable ones, with zero target greenhouse gas emissions. The European Green Pact prioritizes the protection of biodiversity and ecosystems; reducing air, water, and soil pollution; the transition to the circular economy; improving waste management as well as guaranteeing the blue economy and aquaculture sectors sustainability.

The European Union's Strategy for Blue Economy can contribute to this dual challenge: if set on a more sustainable trajectory, it will become a source of action and ideas to create innovation, stimulate a rapid and sustainable recovery and protect the planet [2]. Biodiversity conservation and protection are considered fundamental principles of aquatic economic activities. From the point of view of the strategy, aquatic biodiversity represents an elementary condition necessary for the development

of economic activities such as fishing, biotechnology, and tourism. By making better use of water resources and choosing alternative sources of food and animal feed, the blue economy can help alleviate the pressure on the climate and natural resources for food production. One of the sectors responsible for carbon dioxide emissions, pollution and biodiversity loss is the current food production and consumption system. Placing the system on a sustainable path is the objective of the Commission's Farm to Fork strategy, with a comprehensive approach that intersects with many aspects of the blue economy. These include responsible fishing to bring stocks to sustainable levels, sustainable aquaculture to supplement the natural limits of wild catches, and seaweed production as an alternative to agriculture.

According to Green Deal policies, the "Farm to Fork" Strategy is a central element of the Commission's Agenda for achieving the United Nations' Sustainable Development Goals. All citizens and operators in all value chains, in and outside the EU, should benefit from a fair transition, especially because of the COVID-19 pandemic and the slowdown in economic growth. Shifting to a sustainable food system can bring environmental, social and health benefits, generate economic gains and ensure that over-coming the crisis is equivalent to embarking on a sustainable trajectory. Ensuring sustainable livelihoods for primary producers, who are still lagging in terms of in-come, is critical to the success of the crisis and transition [3]. The COVID-19 pandemic has made society extremely aware of the interconnectedness of health, ecosystems, supply chains, consumption patterns and the limits of the planet. The increasing frequency of droughts, floods, wildfires, and new pests are a constant reminder that

our food system is under threat and must become more sustainable and resilient. The European Green Deal and the Farm to Fork Strategy highlight the potential of aquaculture food as a source of protein for food and feed with a low carbon footprint, which plays an important role in building a sustainable food system.

In the vision of the Common Fisheries Policy [4], aquaculture creates jobs and economic development opportunities in the EU's coastal and rural communities. With a long-term strategy this sector can also contribute to the de-carbonization of the economy; combating climate change and mitigating its impact; reducing pollution; better conservation of ecosystems and can be part of a more circular management of resources. According to [5], the self-sufficiency rate for fishery and aquaculture products was around 42% in 2018. The self-sufficiency rate is defined as the ability of EU member states to meet demand from their own production and can be calculated as the ratio of domestic production to domestic consumption. In terms of resilience, two aspects are particularly challenging for the aquaculture sector: managing animal and human health risks and the impact of climate change. Particularly for freshwater aquaculture, predators and drought also pose a challenge to profitability. Water is becoming a limited resource due to climate change. There is also increasing competition for both space and access to water between different economic activities, including aquaculture.

2. Offshore fish farms

Moving fish farms to offshore locations can be a sustainable alternative to farmed fish production. Floating farms utilize the water surface, allowing for efficient utilization of space without occupying land and can be moved to more suitable locations as needed, adjusting to changing environmental conditions or optimizing for better water quality and fish health. They enable better control over water quality parameters by positioning in areas with cleaner water or equipped with filtration systems to maintain optimal conditions for fish growth. Properly designed floating fish farms can minimize the impact on the surrounding environment by employing systems to manage waste and prevent the release of excess feed or pollutants into the water. Being elevated on water, floating farms can offer protection from some ground-based predators, reducing risks to the fish stock. With proper management and monitoring, floating fish farms can potentially increase productivity due to controlled environments and optimized conditions for fish growth. Floating farms can be more adaptable to changes in water

levels due to factors like seasonal variations or climate change, compared to fixed land-based farms.

The potential of offshore fish farms was identified by [6] who presented the development of offshore aquaculture from economical perspective. The economic potential for offshore aquaculture is dependent by growing population, the relative cost of offshore aquaculture and the relative values of competing uses of potential inshore farming areas will increase.

According to [7] the farming concepts must enable the fish to get the required water exchange and prevent high current velocities from being exposed directly to the fishes. The farming concept shall be proactive by design-out potential failures, predictive to detect unexpected failures, easy to be maintained and preventive for bio-fouling communities. These design requirements aim to cut-off the maintenance cost. One of the most critical criteria is the escaped fish rate. There is a Norwegian Standard 9415 for cage farming equipment to prevent fish escape. However, farming concepts might differ in their mechanism to avoid or mitigate any escaping events.

A comprehensive review was performed by [8] on the existing design standards and procedures issued by classification societies (Det Norske Veritas or Bureau Veritas) and/or national or international technical guidelines with applicability to offshore fish farming installations. Marine loads as currents, waves, wind and mooring of fish farms were found to be the main challenges to offshore fish farming.

As per Bureau Veritas vision about future of offshore fish farming, it's estimated that by 2050, global population growth will require 60% more sustainably produced food. At the same time, the impacts of climate change will be felt across all agricultural sectors. The aquaculture – also called fish farming – could rise as one of the most efficient forms of food production on the planet. Already, it's one of the fastest-growing food production sectors, and its further expansion could help ease pressure on wild fish stocks [9]. The main risks of fish farming are the diseases, pollution, and fish escape, while the main operational challenges are the open water, waves, winds and water currents.

As stated by [10] the continuously demand of fish is leading to disease and environmental challenges and in the lack of space onshore it is expected a migration of fish farming offshore. This trend is also highlighted by OECD [11] and FAO [12] studies. With a forecast of more than 100 million tons in growth of fish farming production by 2027, clean waters, constant water temperatures and low risk of diseases can be the key factors contributing to migration offshore of the fish farms.

3. Ship shaped fish farms

Starting from the current development strategies of the EU and from the difficulties of terrestrial fish farms such as the lack of water and the high price of land but also the lack of labour force, the development of a modular floating fish farm systems is proposed.

As presented by [13], in 2018, Chinese shipyard CIMC Raffles started the construction the first Havfarm fish farm design for Norwegian fish farming company, Nordlaks. With a capacity of 10000 tons of salmon per production cycle, the fish farm, Havfarm 1, entered in operations in 2020 as moored structure at 5 km offshore.

A numerical investigation on the mooring of a vessel-shaped floating fish farm in open sea application was performed by [14]. The largest tension was observed when the current and waves are 90 degrees misaligned.

In 2019 started the construction of the first movable fish farm ship shaped of 100 thousand tons of the fifty such ships [15]. The annual production is estimated at approx. 200 thousand tons of sea fruits or fish. According to design, it is a structure 250 meters long, 45 meters wide, and can reach a speed of 10 knots for relocation or avoiding exceptional severe weather conditions.

Culturing tests were conducted from May to August 2021 on a test aquaculture vessel in the sea regions of Zhejiang, China [16]. The growth rate of *Pseudosciaena crocea* reaches 100 g per month, and the survival rate gets to 95 %, which proves the feasibility of the Shipborne mariculture system.

Recently, a semi-submersible vessel-shaped fish farm platform was proposed by Pang *et al.* The diving the main hull through the water it is conducting to improvement of seakeeping performance. Therefore, the small waterplane area provided a reference for the design of a large fish farm platform [17].

Wang *et al.* investigated the effect of the interaction among the ship shaped floating fish farm, disturbed wave field and hydrodynamic loads on the steel frames and nets under irregular waves. Combining the global response of the cage and velocity, the disturbed irregular wave field is rebuilt to calculate the hydrodynamic forces on slender structures in time domain. Also, the global response is updated by solving the motion equation of the cage in time domain [18].

The idea of a vessel shaped fish farm for maritime exploitation is not new. Instead, for inland rivers and channels the available data is rather poor. Contrary to maritime fish farms, the inland rivers and channels offers to fish farms, either moored or anchored, a more protected area. In this case the wave loads are negligible and in the case of farms with

large superstructures the influence of the wind loads must be investigated.

4. Conclusions

Designing a modular floating fish farm for inland rivers and channels offers several advantages and considerations. Inland rivers and channels might have limited available space along their banks for traditional fish farms.

From modular point of view the cargo hold of one barge can be separated into small modular tanks or more barges can be exploited side by side in modular system. From a constructive point of view, the barge can be equipped with alternative energy recovery systems: wind, flow currents, and solar energy, but also with greenhouses with an aquaponic operating principle. The aquaponic system combines the aquaculture of fish in limited spaces with hydroponics, the cultivation of plants in a liquid environment, and its use starts from the constant need to filter water with nitrites and nitrates from fish tanks and implicitly meaning energy consumption. Instead of classic mechanical filters, aquaponics involves filtering water through vegetable growing beds. From an economic point of view, at the same energy consumption, the fish farm can also produce fresh vegetables, bringing additional income but also fitting into the European paradigm of sustainable and sustainable development. If the aquaculture system allows development without the administration of drugs or chemical feeds, the plants grown with fish water can be considered ecological, bringing added value. Such a barge can be purchased at a scrap price and repaired and customized with minimal expense respecting at the same time the decarbonization strategy of the European Green policy by considerably reducing CO₂ emissions from the steel production process. Also, in case of severe weather conditions these fish farms can be moved easily to a safer position with the help of a river tug or pusher, either single or multiple combination as convoy.

Acknowledgement

This project was financed through the financing program for Sustaining and developing research activities CDI-TT of "Dunarea de Jos" University of Galati, Contract no. 9416/30.03.2023.

References

- [1]. ***, European Commission, *European Green Deal*, Brussels, 2019.
- [2]. ***, European Commission, *European Green Deal: Developing a sustainable blue economy in the*

- European Union, Brussels, <https://www.consilium.europa.eu/en/policies/green-deal/>, 2021.
- [3]. ***, European Commission, *European Green Deal: Farm to Fork Strategy*, Brussels, Farm to Fork Strategy - European Commission (europa.eu), <https://www.cerealdocks.it/en/farm-to-fork-strategy-fair-and-eco-friendly-food-supply-chains/>, 2020.
- [4]. ***, European Commission, *Common Fisheries Policy*, Brussels, 2023.
- [5]. ***, European Commission, *EUMOFA, EU Fish Market Report*, Brussels, 2020.
- [6]. Knapp G., *The development of offshore aquaculture: an economic perspective*, In A. Lovatelli, J. Aguilar-Manjarrez & D. Soto, eds. Expanding mariculture farther offshore: technical, environmental, spatial and governance challenges. FAO Technical Workshop, 22–25 March 2010, Orbetello, Italy. FAO Fisheries and aquaculture Proceedings No. 24. Rome, FAO, p. 201-244, 2013.
- [7]. El-Thalji I., *IOP Conf. Ser.: Mater. Sci. Eng.*, 700 012065, 2019.
- [8]. Chu Y. I., Wang C. M., Zhang H., Abdussamie N., Karampour H., Jeng D. S., Baumeister J., Aland P. A., *Offshore Fish Farms: A Review of Standards and Guidelines for Design and Analysis*, *J. Mar. Sci. Eng.*, 11, 762. <https://doi.org/10.3390/jmse11040762>, <https://www.mdpi.com/2077-1312/11/4/762>, 2023.
- [9]. ***, <https://marine-offshore.bureauveritas.com/insight/business-insights/promising-future-offshore-fish-farming>.
- [10]. ***, <https://www.dnv.com/focus-areas/offshore-aquaculture/>.
- [11]. ***, www.oecd.org.
- [12]. ***, www.fao.org.
- [13]. ***, <https://www.ship-technology.com/features/havfarm-fish-farm-vessel/>.
- [14]. Li L., Jiang Z., Høiland A. V., Ong M. C., *Numerical Analysis of a Vessel-Shaped Offshore Fish Farm*, *J. Offshore Mech. Arct. Eng.*, 140(4): 041201, <https://asmedigitalcollection.asme.org/offshoremechanics/article/140/4/041201/442728/Numerical-Analysis-of-a-Vessel-Shaped-Offshore>, 2018.
- [15]. Times G., *Construction begins on world as first 100,000 farming vessels in Qingdao*, <https://www.globaltimes.cn/content/1210431.shtml>, 2020.
- [16]. Zhisong L., Xiaoyu G., Mingchao C., *Numerical investigation of flow characteristics in a rearing tank aboard an aqua-culture vessel*, *Aquacultural Engineering*, vol. 98, 102272, <https://doi.org/10.1016/j.aquaeng.2022.102272>, 2022.
- [17]. Pang G., Zhang S., Liu H., Zhu S., Yuan T., Li G., Han X., Huang X., *Hydrodynamic response analysis for a new semi-submersible vessel-shaped fish farm platform based on numerical simulation*, *Front. Mar. Sci.*, 10:1135757. doi: 10.3389/fmars.2023.1135757, <https://www.frontiersin.org/journals/marine-science/articles/10.3389/fmars.2023.1135757/full>, 2023.
- [18]. Wang Y., Fu S., Xu Y., Cheng T., Li S., Moan T., Fu Q., Liu F., *Load effects on vessel-shaped fish cage steel structures, nets and connectors considering the effects of diffraction and radiation waves under irregular waves*, *Elsevier Marine Structures*, vol. 91, 103468, September 2023.
- [19]. Martinez M. A., Brons A., Wertheim-Heck S. C. O., *How do the people that feed Europe feed themselves? Exploring the (in)formal food practices of Almería's migrant and seasonal food workers*, *Agriculture and Human Values*, 41:731–748, <https://doi.org/10.1007/s10460-023-10513-8>, 2024.
- [20]. Iures M. V. C., *The Main Differences Between the Updated Bioeconomy Strategy and the European Green Deal*, *Annals - Economy Series*, Constantin Brancusi University, Faculty of Economics, vol. 5, p. 228-233, October.
- [21]. ***, https://ec.europa.eu/commission/presscorner/api/files/document/print/en/ip_19_6691/IP_19_6691_EN.pdf.
- [22]. ***, <https://eucalls.net/blog/the-basics-of-the-european-green-deal>.
- [23]. Adamos G., Caucci S., Charpentier L., et al., *Exploring nexus policy insights for water-energy-food resilient communities*, *SNF* 31, p. 69-82, <https://doi.org/10.1007/s00550-024-00534-0>, 2023.

STUDIES ON THE CONVERSION OF A RIVER CARGO BARGE INTO A FLOATING FISH FARM

Costel UNGUREANU, Adrian PRESURĂ, Radu BOSOANCĂ, Andreea MÂNDRU, Silviu PERIJOC, Victor MIHAI, George COTOC
"Dunarea de Jos" University of Galati, Naval Architecture Faculty, Romania
e-mail: costel.ungureanu@ugal.ro

ABSTRACT

This paper presents results of the research and developing of a modular floating aquaculture platform based on inland river cargo barge design to be exploited under biosecurity and sustainability conditions in the Lower Danube region, aligned with the current sustainable development strategies of the blue economy outlined by the European Union. The new design combines the capabilities of growing fish in modular tanks with the growing vegetables in recirculating systems in the greenhouse superstructure of the floating platform. The first step of this interdisciplinary and multidisciplinary research is a full naval architecture study, meaning both aerodynamically and strength calculation, as a starting point for the design and evaluation of the growing fish and cultivating vegetables systems.

KEYWORDS: fish farm, aquaculture platform, river barge, CFD, FEM, wind tunnel

1. Introduction

In 2019 the construction of the world's first 100,000-tonne large-scale fish farming ship started in China, pioneering a new mode of industrial farming with "movable fish farms" on distant seas [1]. The Conson Group plans to invest in the construction of an aquaculture armada consisting of 50 such ships with a gross tonnage of 100,000 tons each, which are expected to annually produce about 200,000 tons of seawater fish with an annual output value exceeding 11 billion yuan (\$1.68 billion). With a length of 249.9 meters, a width of 45 meters, and a designed speed of 10 knots, the vessel can avoid typhoons, red tides and other severe weather and disasters, conducting aquaculture operations in seas around the world.

Culturing tests were conducted from May to August 2021 on a test aquaculture vessel in the sea regions of Zhejiang, China [2]. The growth rate of *Pseudosciaena crocea* reaches 100 g per month, and the survival rate gets to 95 %, which proves the feasibility of the Shipborne mariculture system.

Recently, a semi-submersible vessel-shaped fish farm platform was proposed [3] Pang *et al.* (2023). By diving its main body through the water its seakeeping performance under extreme conditions improved. Therefore, the small waterplane area

provided a reference for the design of a large fish farm platform.

Chu *et al.* performed a comprehensive review on the existing design guidelines and technical guidance from maritime classification rules/standards and national and inter-national standards with applicability to offshore fish farming installations with direct interest to aquaculture engineers and designers when developing offshore fish farming infrastructure [4].

The aquaculture industry is aiming to move fish farms from nearshore areas to open seas because of many attractive advantages in the open water [5]. However, the major challenge is to design the structure to withstand the harsh environmental loads due to wind, waves, and currents. Contrary to maritime fish farms, the inland rivers and channels offers to fish farms, either moored or anchored, a more protected area. In this case the wave loads are negligible and in the case of farms with large superstructures the influence of the wind loads must be investigated.

This paper presents the results of the research on the conversion of a cargo river barge into a floating fish farm, for the inland rivers in the Lower Danube region of Romania. The study is developed based on the following objectives:

- Analysis of existing floating fish farms and definition of parameters and conditions for the design of the floating structure
- General arrangement of the barge as a floating fish farm
- Numerical investigations of barge strength using FEM
- Numerical investigations of barge superstructure aerodynamic characteristics using CFD
- Wind tunnel investigations of barge superstructure aerodynamic characteristics using EFD.

2. Fish farm design

The 3000 tons typical barge was considered as base for the conversion into a fish farm for which the main dimensions are presented in Table 1. As can be seen in Figure 1 a greenhouse was considered above the main deck, covering fish tanks and aquaponics systems, and the cargo hull was separated into 12 modular tanks. At midship a pump room was considered below main deck, and a technological container was placed above.

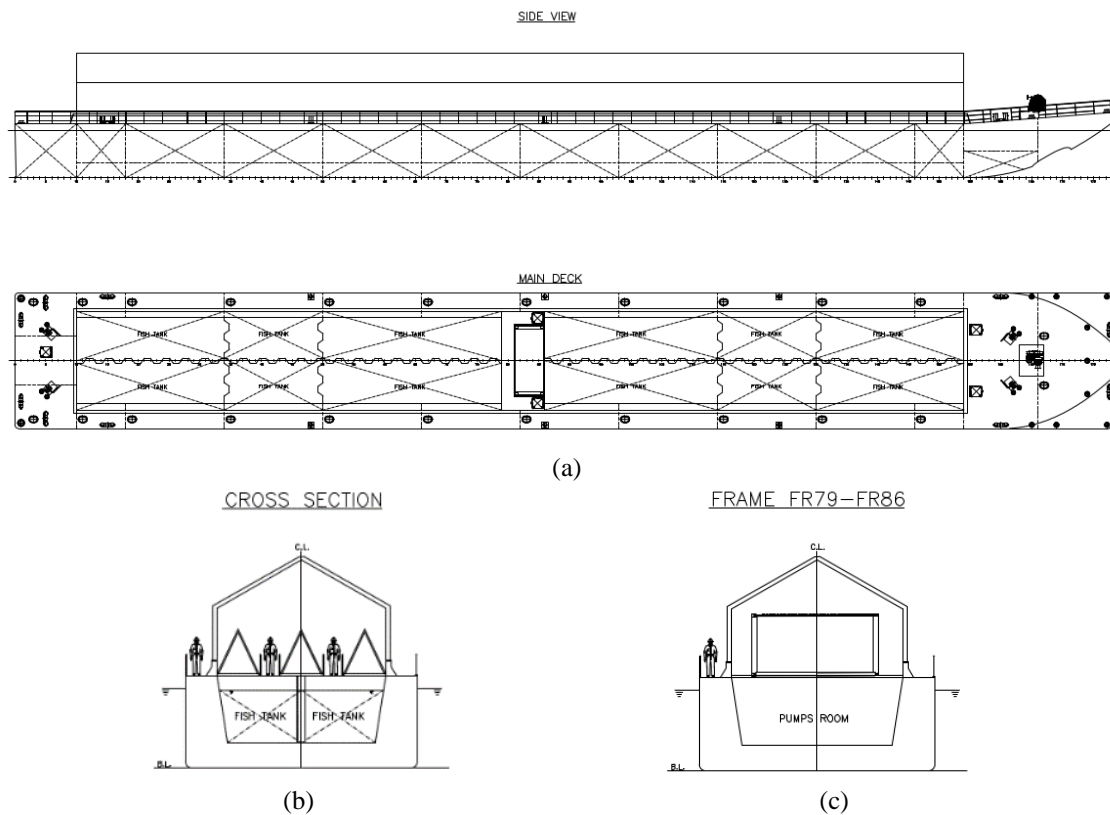


Fig. 1. General arrangement of the fish farm: (a) Side and top view; (b) Transversal view -typical section, (c) Transverse section at midship

Table 1. Barge main dimensions

Main dimensions	Value	Units
Length overall	89.0	meters
Height overall	10.5	
Beam	11.0	meters
Depth	4.4	meters
Draught	3.8	meters
Bloc coefficient	0.935	-
Displacement	3459	tons

As stated before, solar panels can be mounted either above fish tanks, providing direct sun protection to fish water, or to greenhouse top

providing both electrical energy and shade to plant growing systems. The latter was considered in the present research. Knowing that the average tilt angle

of photovoltaic panels during warm months was found to be approximately 29° [6] in an area close to the main target area of this project, lead to a 30°

inclination design angle for the greenhouse roof. In Figure 2 the proposed conceptual design is presented.



Fig. 2. The fish farm concept: (a) Fore starboard view; (b) Greenhouse interior view

Based on the proposed design a numerical strength verification is performed to assess the loading capacity of fish farm. After that, an aerodynamical, both numerically and experimentally, investigation is performed from floating establishment naval architecture point of view.

3. Strength verification

Performing a 3D-FEM (Finite Element Method) analysis on extended FE models has become nowadays relatively accessible, allowing more improvements to be included in a single design step, resulting in a final product that meets the safety criteria over its entire life cycle [7]. The slender body of the barge, combined with a large main deck opening and a shallow draught result in a low bending and torsional rigidity. The sum of the above facts can lead to local failure and loss of structural integrity if

stress levels are not evaluated properly in the design stage [8]. Since the structure of typical inland barge is subjected throughout its life cycle to structural changes due to minor collisions, either ship-to-ship or ship-to-quay, shallow-water groundings, corrosion, fatigue, the strength, and stability of the barge structure can be drastically reduced [9]. This part is aiming to investigate 3D-FEM global structural analysis of an inland barge retrofitted as floating fish farm considering the still water condition and full load condition based on the equivalent quasi-static approach [10-12].

A surface 3D-CAD model of the barge with greenhouse was generated using the Ansys built-in modeler Space Claim (Figure 2). The steel grade A material formulation with yield stress limit of 235 MPa and rupture stress limit of around 400 MPa is provided.

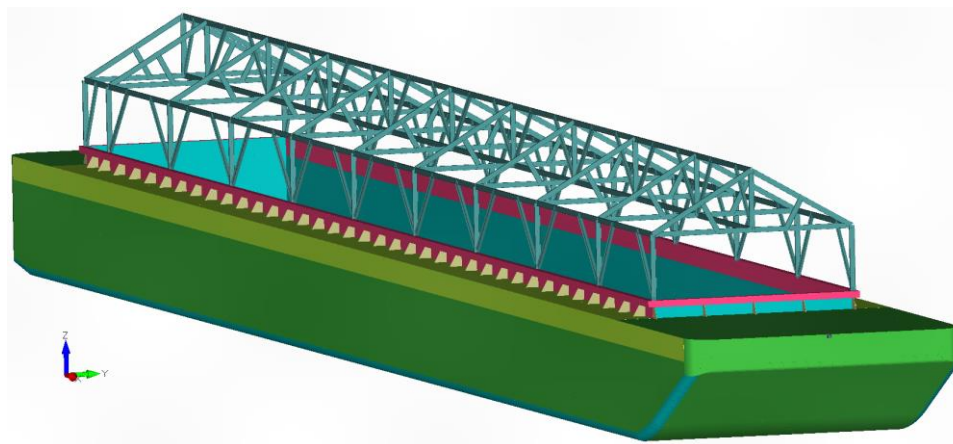


Fig. 2. CAD model of barge with greenhouse

Next, the results obtained following the analysis of the 3D-FEM model for the river barge in full loading condition are presented. The loading cases sets are as following:

- LC_1 - Still water condition;
- LC_2 - Full loading condition -hogging;
- LC_3 - Full loading condition - sagging.

Hydrostatic pressure on the outside shell and on inner hull was applied and together with the numerical results for the LC1 is presented in Figure 3.

The fish farm was designed to be anchored or moored to quay, but waves generated by the shipping on rivers and channels may reach the local position.

Therefore, a study for the evaluation of stress assessment in respect to wave loads was performed for both cases hogging and sagging. The numerical results are plotted as deformed view in Figure 4. The wave height for was considered 1.2 m.

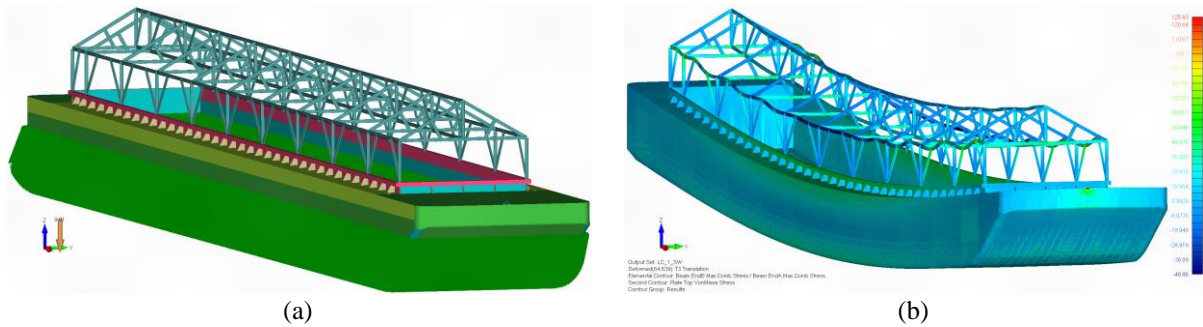


Fig. 3. LC1-Still water condition:(a) Model with applied hydrostatic pressure, (b)FEM results, deformed view

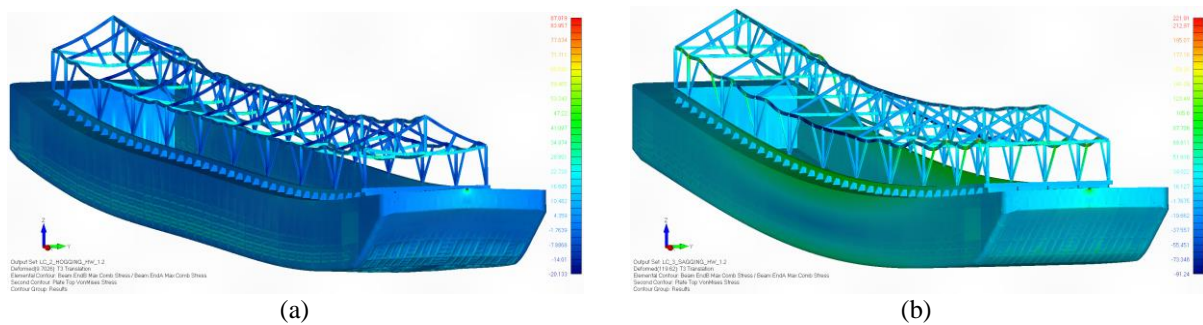


Fig. 4. Von Mises stress, deformed view: (a) LC2-Hogging, (b) LC3-Sagging

It was observed that the maximum Von Mises stress obtained was 125 MPa for the still water case, 87 MPa for hogging case and 222 MPa for sagging case.

The current study presents a global structural 3D-FEM analysis of a typical open-top, double-hull barge, having a cargo capacity of 3000 dwt with a greenhouse superstructure. In the framework of analysis and data interpreting processes it can be concluded that the current structural layout of the barge does not present any structural risk. The FE results examination pointed out some structural hot-spots, especially for LC3 case where yielding ratio found to be higher than 0.8, that require updates for a better distribution of the local occurring stresses. Further investigations must be performed after the structural update of the identified hot-spot areas, completed by other strength criteria.

4. Aerodynamic investigations

Two types of methods are known for the study of aerodynamic flow around the barge as fish farm

with greenhouse mounted on main deck: experimental and numerical. Experimental investigation involves complex research infrastructure, such as wind tunnels and measuring equipment. The experiments provide a quantitative description of the flow measurements individually for each investigated physical quantity, in a limited number of points in the flow field for a small range of problems and experimental conditions. Experiments are also expensive, slow, sequential, and repetitive. Another important element in experimental research is model manufacturing. So, in this research, the experimental study on the model is used only for the validation of the global aerodynamic performances of the new concepts.

4.1. Experimental investigations

The experiments were carried out in the Wind tunnel of the Naval Architecture Faculty, “Dunarea de Jos” University of Galati, presented in Figure 5a, [13]. The main dimensions of the wind tunnel are length = 17 m, width = 3.7 m and height = 3.4 m.

Also, the main dimensions of the measuring section of the tunnel are length = 2.5 m, width = 0.82 m and height = 0.58 m. The maximum air velocity of 23.5 m/s can be obtained, and the maximum physical model length of 2 m can be used in the wind tunnel. The wind tunnel drive system includes an axial flow blower with variable speed and a motor power of 55 kW and 1450 RPM.

Using a 3D printer, the experimental model presented in Figure 5b was printed at a scale of 1:150, having the following main dimensions, where m is for model: $L_m = 600$ mm, $B_m = 73$ mm, Air draft surface model $2.58222 \times 10^{-3} \text{ m}^2$. Only the upper part of the model containing the new superstructure and all exposed surfaces to wind loads was tested.

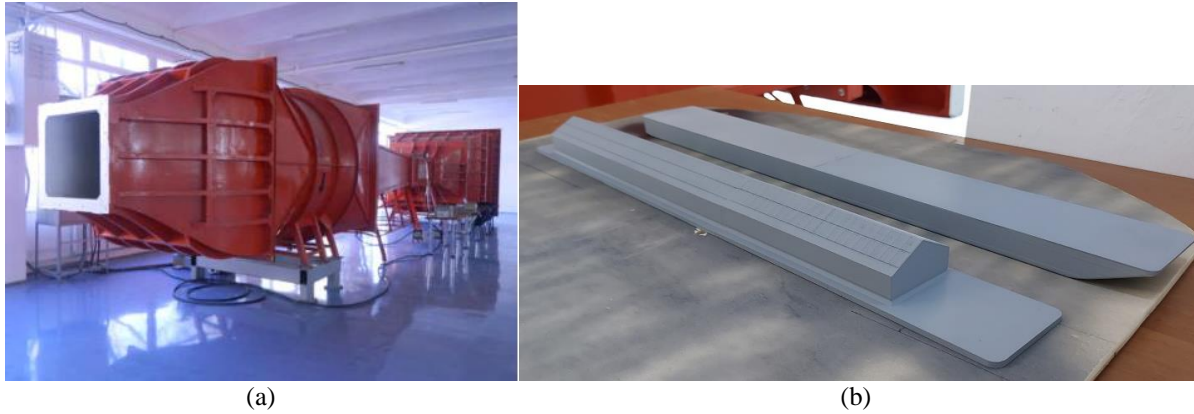


Fig. 5. Wind tunnel: (a) Global view; (b) Experimental model

For this experimental model, specific equipment was used to be able to accurately measure the air velocity and the forces and moments that apply on the model. For this reason, a highly accurate Pitot tube was used conned to a 16-channel pressure scanner, which was used to measure differential pressure (dynamic pressure) in the measuring section. The scanner has its own software for measuring the analogical data and changing it to digital data to calculate air velocity. Once knowing the dynamic pressure (P_{dyn}) value, the air velocity (v) can be extracted from the following formula:

$$P_{dyn} = 0.5 \rho v^2 \quad (1)$$

where density (ρ) varies with the air temperature inside the testing facility.

The air temperature throughout the day of testing was 20° C and consequently the air density, used in the calculation for the air velocity, was 1.025 kg/m³.

In Figure 6, the results for longitudinal, F_x , and lateral, F_y , drag force components are presented in respect of angle of attack.

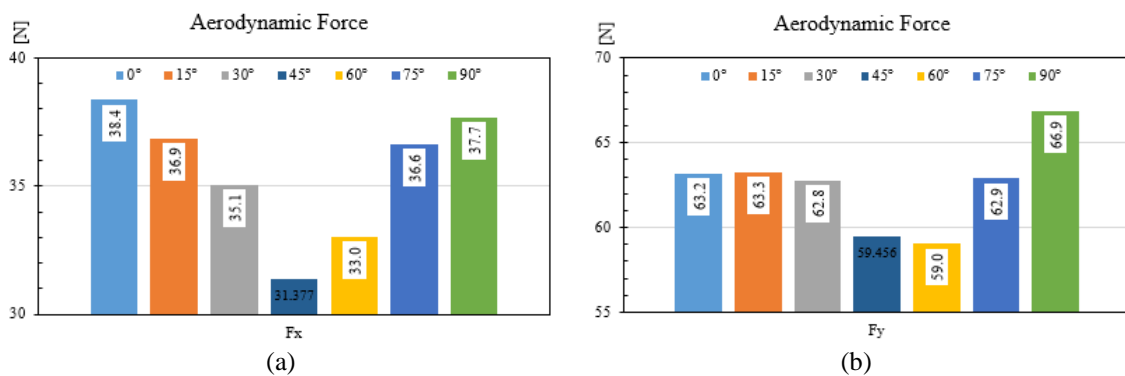


Fig. 6. Measured aerodynamic forces diagrams (a) F_x ; (b) F_y

4.2. Numerical investigations

The alternative to experimental investigations is numerical simulations (CFD-computational Fluid

Dynamics), which have gained significant popularity, especially after the development of advanced numerical methods and the advent of digital machines with high computing power. In general, numerical

simulations offer a wide range of advantages over similar experimental research. First, numerical simulations provide a quantitative prediction of the flow simultaneously for all investigated physical quantities, in a very large number of points in time and space. Second, a numerical solution substantially reduces design and production times and costs. At the same time consumed by a case, as many cases can be studied as there are computing machines available.

In this study, the governing equations were solved using the Reynolds-Averaged Navier-Stokes (RANS) method. The commercial CFD code NUMECA/FineMarine, was used to solve these mass and momentum conservation equations. In the Cartesian coordinate system, the averaged continuity and momentum equations for incompressible flows, including external forces (2 and 3), can be expressed in tensor form as:

$$\frac{\partial(\rho \bar{u}_i)}{\partial x_i} = 0 \quad (2)$$

$$\frac{\partial(\rho \bar{u}_i)}{\partial t} + \frac{\partial}{\partial x_j} (\rho \bar{u}_i \bar{u}_j + \rho \overline{u'_i u'_j}) = -\frac{\partial \bar{p}}{\partial x_i} + \frac{\partial \bar{\tau}_{ij}}{\partial x_j} \quad (3)$$

where ρ is density, u_i is the relative averaged velocity vector of flow between the fluid and the control volume, $u'_i u'_j$ is the Reynolds stresses, \bar{p} is the mean pressure, and τ_{ij} is the mean viscous stress tensor component for Newtonian fluid under the incompressible flow assumption, and it can be written as in equation 4:

$$\bar{\tau}_{ij} = \mu \left(\frac{\partial \bar{u}_i}{\partial x_j} + \frac{\partial \bar{u}_j}{\partial x_i} \right) \quad (4)$$

in which μ is the dynamic viscosity.

To solve the incompressible steady RANSE in a global approach, the solver uses the finite volume method to generate the spatial discretization for the governing equations [14]. The RANSE's convection and diffusion terms are discretized using a second-order upwind scheme and a central difference scheme. The velocity field is calculated using

momentum conservation equations, while the pressure field is determined using the mass conservation constraint, which is then transformed into a pressure equation. Additional transport equations for modelled variables are discretized and solved in the case of turbulent flows using the same principles, as described by [15]. In this study, the k- ω SST turbulence model with wall function formulation and wall roughness model implemented is employed for turbulence closure.

Being designed as a floating establishment, the fish farm is associated with a land construction and the wind velocity value is calculated based on the imposed dynamic pressure which in the subject area is equal to 0.6 [16]. Also, multiple wind direction was taken into consideration, as can be seen in Figure 6 (a), for one side covering of 180° with a step of 15°. The other side is considered symmetrical, and it was not investigated.

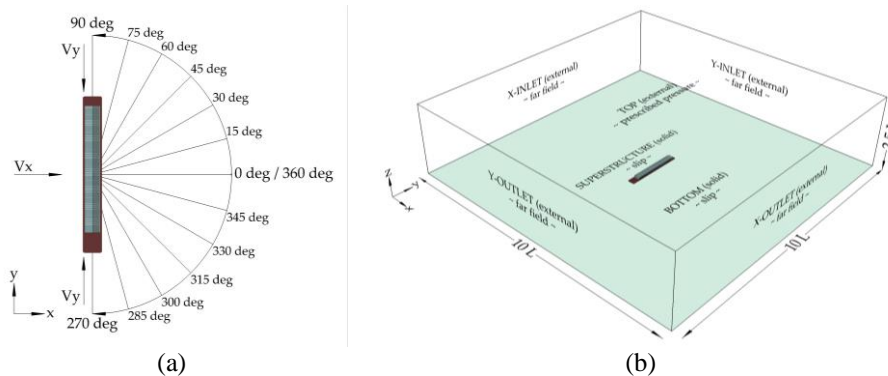


Fig. 6. Numerical model: (a) Angle map of wind directions in respect to barge; (b) Computational domain with boundary conditions

To avoid the reflection of the wind from the lateral boundaries, producing numerical instabilities a box type computational domain was generated with

10 x 10 x 2.5 L dimensions. The boundary conditions, shown in Figure 6 (b), have been chosen to be compatible with the numerical wind tunnel principle

calculation, namely farfield with the imposition of the velocity. The solid wall condition was imposed on the model and on the bottom boundary to simulate the flow inside wind tunnel.

An unstructured hexahedral mesh has been generated to cover the entire computational domain along the barge model. The grid topology is an H-H type. Details of the near-hull corner grids and on the hull, itself are presented in Figure 7.

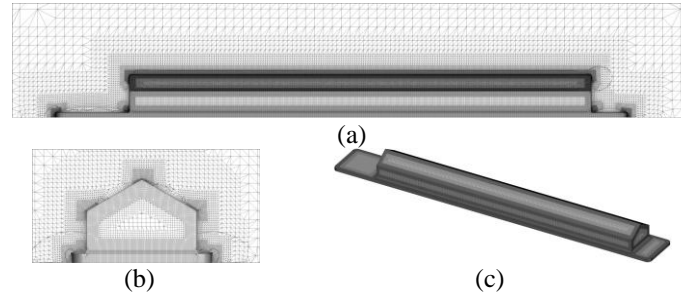


Fig. 7. Numerical grid: (a) Longitudinal section; (b) Transverse section; (c) Gridlines on barge model

Next, the results for full scale numerical investigations are presented. The pressure effect of wind on a greenhouse can have significant implications for its structural integrity and the well-being of the plants inside. Wind creates both positive and negative pressure on the surfaces of the greenhouse. Positive Pressure: Wind hitting the windward side of the greenhouse creates positive pressure. It pushes against the structure, potentially causing stress on the materials, joints, and supports. Negative Pressure: On the leeward side or the sides where the wind flows around, it creates a negative pressure zone. This can cause suction forces that may try to pull the structure outward. These pressure

effects can vary based on factors such as wind speed, direction, the design of the greenhouse, its orientation to prevailing winds, and the materials used in its construction. Aligning the greenhouse in a direction that minimizes exposure to prevailing winds can reduce direct impact. This is possible on lakes or open seas where the fish farm can be anchored and can easily rotate to be properly aligned with the wind direction. For rivers and channels the available space for manoeuvring is limited. Therefore, the pressure and the turbulence on the greenhouse are computed and presented next. The pressure is presented for both sides positive and negative in Figure 8.

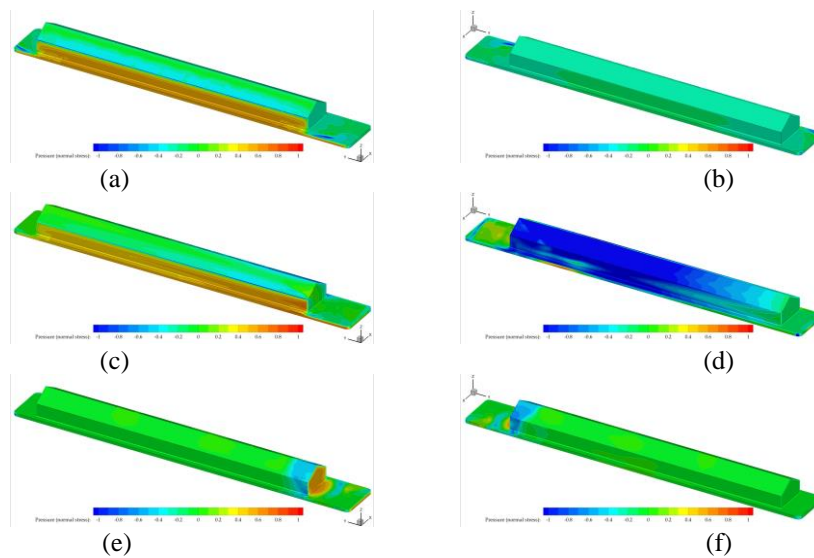


Fig. 8. Pressure distribution on greenhouse and on hull above free surface: (a) 0° - positive side, (b) 0° - negative side, (c) 45° - positive side, (d) 45° - negative side, (e) 90° - positive side, (f) 90° - negative side

Turbulence caused by wind loads on a greenhouse can create complex airflow patterns that affect the structure and the plants within it. Wind turbulence is characterized by irregular fluctuations in wind speed and direction. Turbulence creates varying pressure points on different parts of the greenhouse. This can lead to uneven stress distribution across the structure, potentially causing weak points or areas

prone to damage. Understanding the potential effects of turbulence and taking proactive measures during the design, construction, and maintenance of the greenhouse can help minimize its negative impact on the structure and the plants grown within it. Next, Figure 9 presents the turbulence evolution in respect to wind direction.

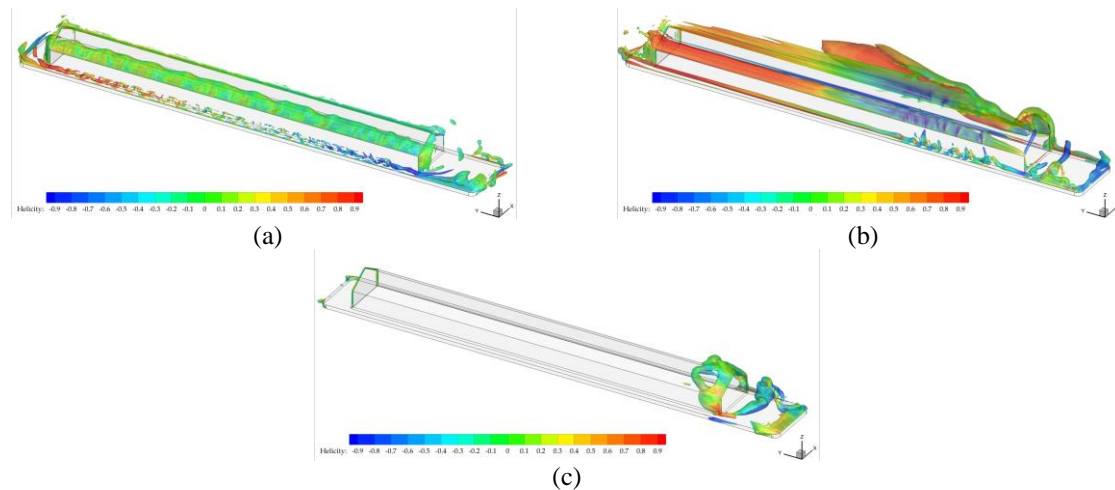


Fig. 9. The turbulence evolution in respect to wind direction

5. Conclusions

This research proposed for the first part of this interdisciplinary and multidisciplinary research a conversion from a cargo river barge to a modular floating fish farm. Before evaluating the fish and vegetables cultivation systems a full naval architecture study, meaning both aerodynamic and strength calculation, was performed.

The novelty of this study is the realization of a pilot project of a modular aquaculture platform for exploitation under biosecurity and sustainability conditions in the Lower Danube region, aligned with the current sustainable development strategies of the blue economy outlined by the European Union.

Acknowledgement

This project was financed through the financing program for Sustaining and developing research activities CDI-TT of „Dunarea de Jos” University of Galati, Contract no. 9416/30.03.2023. All studies were performed using the research facilities of the Naval Architecture Faculty and of the Naval Architecture Research Center, such as the numerical hydrodynamics laboratory, the numerical structural analysis laboratory, the wind tunnel, as well as the integrated design systems for hull and ship systems.

References

- [1]. Times G., *Construction begins on world as first 100,000 farming vessels in Qingdao*, <https://www.globaltimes.cn/content/1210431.shtml>, 2020.
- [2]. Zhisong L., Xiaoyu G., Mingchao Cui., *Numerical investigation of flow characteristics in a rearing tank aboard an aquaculture vessel*, *Aquacultural Engineering*, vol. 98, 102272, <https://doi.org/10.1016/j.aquaeng.2022.102272>, August 2022.
- [3]. Pang G., Zhang S., Liu H., Zhu S., Yuan T., Li G., Han X., Huang X., *Hydrodynamic response analysis for a new semi-submersible vessel-shaped fish farm platform based on numerical simulation*, *Front. Mar. Sci.*, 10:1135757. doi: 10.3389/fmars.2023.1135757, 2023.
- [4]. Chu Y. I., Wang C. M., Zhang H., Abdussamie N., Karampour H., Jeng D. S., Baumeister J., Aland P. A., *Offshore Fish Farms: A Review of Standards and Guidelines for Design and Analysis*, *J. Mar. Sci. Eng.*, 11, 762. <https://doi.org/10.3390/jmse11040762>, 2023.
- [5]. Li L., Jiang Z., Høiland A., Ong M., *Numerical Analysis of a Vessel-Shaped Offshore Fish Farm*, *Journal of Offshore Mechanics and Arctic Engineering*, 140. 041201. 10.1115/1.4039131, 2018.
- [6]. Manolache A. I., Andrei G., Rusu L., *An Evaluation of the Efficiency of the Floating Solar Panels in the Western Black Sea and the Razim-Sinoe Lagunar System*, *J. Mar. Sci. Eng.*, 11, 203. <https://doi.org/10.3390/jmse11010203>, 2023.
- [7]. Domnisoru L., *Numerical approach for global ship strength analysis based in 1D-Beam model, under oblique equivalent quasi-static wave loads*, Galati University Press: Shipbuilding, 38, p. 27-36, 2015.
- [8]. Savin M., Presura A., Chirica I., *Environmental protection using structural analysis of ships*, *Sea Conf. IOP Conference Series: Journal of Physics (1297)*, Article 012015, 2019.



- [9]. **Meinken A., Schlüter H. J.**, *Collapse behavior of a push-barge*, Marine Structures, 15(2), p. 193-209, 2002.
- [10]. **Domnisoru L.**, *Special chapters on ship's structures analysis*, Applications (Galati: The University Foundation „Dunarea de Jos” Publishing House), 2017.
- [11]. **Domnisoru L.**, *Strength assessment in oblique design waves for a Europe B2 1740T river barge type*, Galati University Press: Shipbuilding, 41, p. 23-28, 2019.
- [12]. **Domnisoru L.**, *On the strength assessment of a small liquid petroleum gas carrier in oblique waves by 1D and 3D-FEM analyses*, ModTech. IOP Conference Series: Materials Science and Engineering, (916) Article 012027, 2020.
- [13]. **Obreja D.**, *Experimental Techniques in the Wind Tunnel of Naval Architecture Faculty*, Annals of "Dunarea de Jos" University Galati. Fascicle XI, Shipbuilding, 2021.
- [14]. **Guilmineau E., Deng G. B., Leroyer A., Queutey P., Visonneau M., Wackers J.**, *Influence of the turbulence closures for the wake prediction of a marine propeller*, Proc. of the 4th International Symposium on Marine Propulsors, 2015.
- [15]. **Duvigneau R., Visonneau M., Deng G. B.**, *On the role played by turbulence closures in hull shape optimization at model and full-scale*, Journal of Marine Science and Technology, 8 (1) p. 1-25, 2003.
- [16]. ***, CR 1-1-4/2012. Cod de proiectare, *Evaluarea actiunii vantului asupra constructiilor*.

AN OVERVIEW ON ZnO REINFORCED COMPOSITES

**Andreea Elena ONACHE (VIJAN)¹, Alina Maria IANCU²,
Adriana-Gabriela SCHIOPU³, Mihai OPROESCU⁴, Ilie STELIAN⁵**

¹ Doctoral School Materials Science and Engineering, National University of Science and Technology POLITEHNICA Bucharest, Romania

² Pitești University Centre, Faculty of Theology, Letters, History and Arts, National University of Science and Technology POLITEHNICA Bucharest, Romania

³ Pitești University Centre, Faculty of Mechanics and Technology, National University of Science and Technology POLITEHNICA Bucharest, Romania

⁴ Faculty of Electronics, Communication and Computer Science, Pitești University Centre, National University of Science and Technology POLITEHNICA Bucharest, Romania

⁵ Mira Technologies Group

e-mail: ¹ elena_andreea.vijan@stud.sim.upb.ro, ² alyna_aly68@yahoo.com, ³ gabriela.schiopu@upb.ro, ⁴ mihai.oproescu@upb.ro, ⁵ ilie.stelian@miratechnologies.ro

ABSTRACT

Zinc oxide reinforced composites are a promising class of materials with a wide range of potential applications. By combining ZnO with other materials, scientists and engineers can achieve advanced functionalities that go beyond the properties of the individual components. The article offers to researchers and specialists an organized and thoughtful overview on outlining the impacts of composites, emphasis on ZnO nanoparticles reinforced composites.

KEYWORDS: ZnO, composites, reinforced, bonds in composites, ZnO reinforced composites

1. Introduction

Composites are combinations of two (or more) materials in which one of them, called the reinforcement phase, is in the form of fibres, plates, or particles, and included in other materials called the matrix phase. Reinforcement and matrix materials can be metals, ceramics, or polymers. Particles used for reinforcement include ceramics and glasses such as small mineral particles, metallic particles, or metallic oxides such as alumina and amorphous materials including polymers and carbon. Composite materials can be reinforced by dispersion with nano and microparticles particles or large particles preferentially or randomly oriented. Nanoparticles have an atomic profile that can be utilized to control the physical and chemical properties of advanced composite materials.

The era of advanced composite materials is noteworthy for tending to the issues of standard composites totally different applications.

The dispersed phase is, as a rule, a stable oxide of aluminium oxide (Al₂O₃), thorium oxide (ThO₂), zirconium oxide (ZrO₂), beryllium oxide (BeO), magnesium oxide (MgO) or zinc oxide (ZnO). The

dispersed phase must have certain dimensions, shape, quantity, and distribution to obtain the best properties for the composite material. At the same time, it must have low solubility in the matrix material and no chemical reaction between the particles and the matrix.

Researchers have made approaches to refit the properties of typical fiber-reinforced composites by treating the fiber with zinc oxide nanoparticles (ZnO NP).

This review looks at the potential advantage of treating typical strands with ZnO nanoparticles to modify the surface geography of features to move forward the properties of common fiber reinforced composites. The article also depicts the utilize of ZnO NPs to obtain different levelled fibres that can help update the properties of fiber composites and highlight avenues for future investigation in this area.

To endorse the researchers' interest in developing, characterizing, and investigating the properties of composites reinforced with ZnO particles, the types of publications were analysed: article, proceeding paper, review article, early access, book chapters, meeting abstract, letter, editorial

materials the search was performed in the Web of Science database [1], as presented in Fig. 1.

The according bibliometric study was conducted to the following keywords: ZnO nanoparticles, reinforced composites, ZnO reinforced composites, ZnO reinforced fiber composites, for the period 2016-

2023. The refinement of the articles was done later considering the authors from Romania. Fig. 2 shows interest in disseminating results for the study of ZnO nanoparticles and reinforced composites. There is a continuous increase in the experimentation of these research topics.

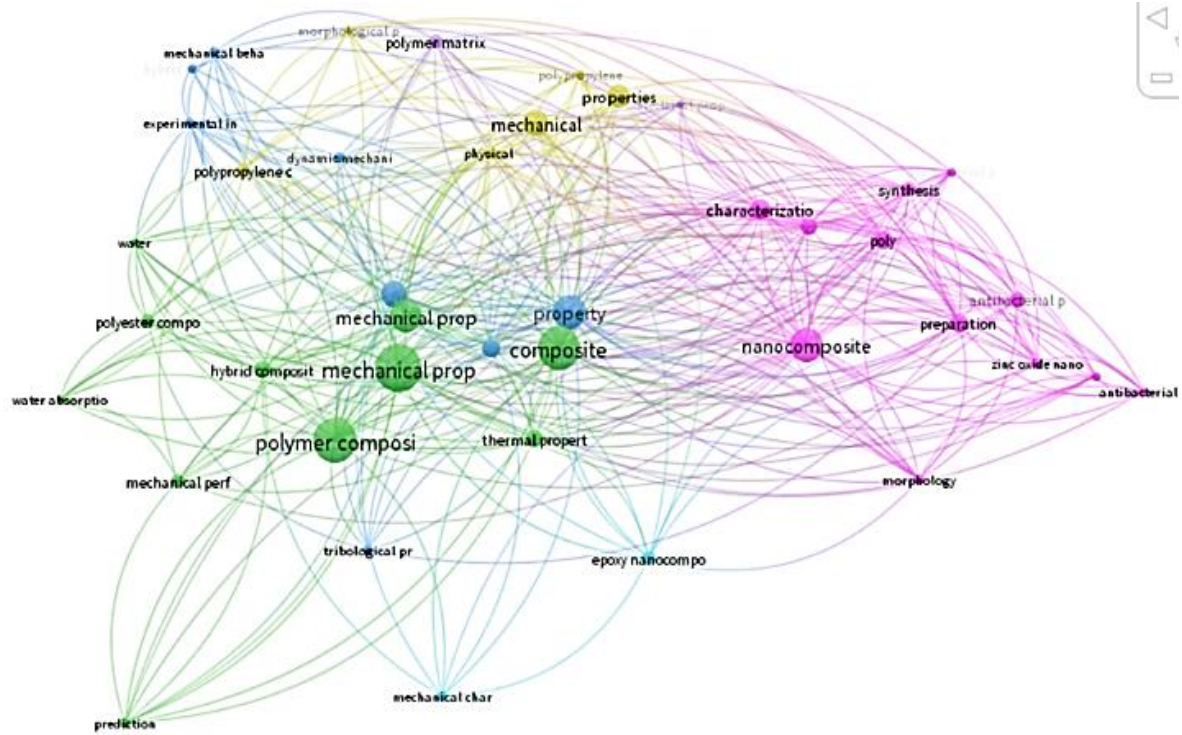


Fig. 1. Occurrence of keywords composites-ZnO nanoparticles-reinforced particles, top cited papers published in Web of Science

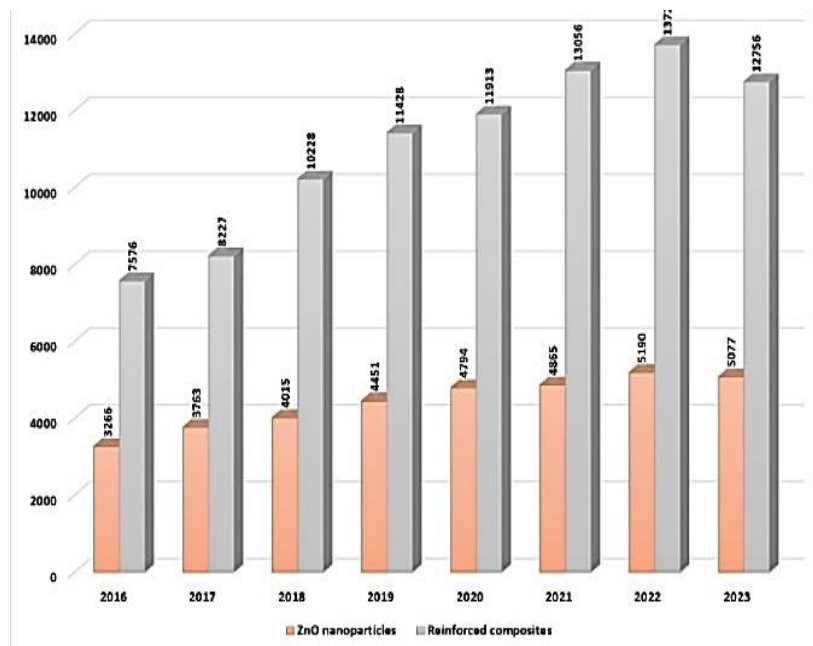


Fig. 2. Publication' evolution regarding the topics: ZnO nanoparticles and Reinforced composites

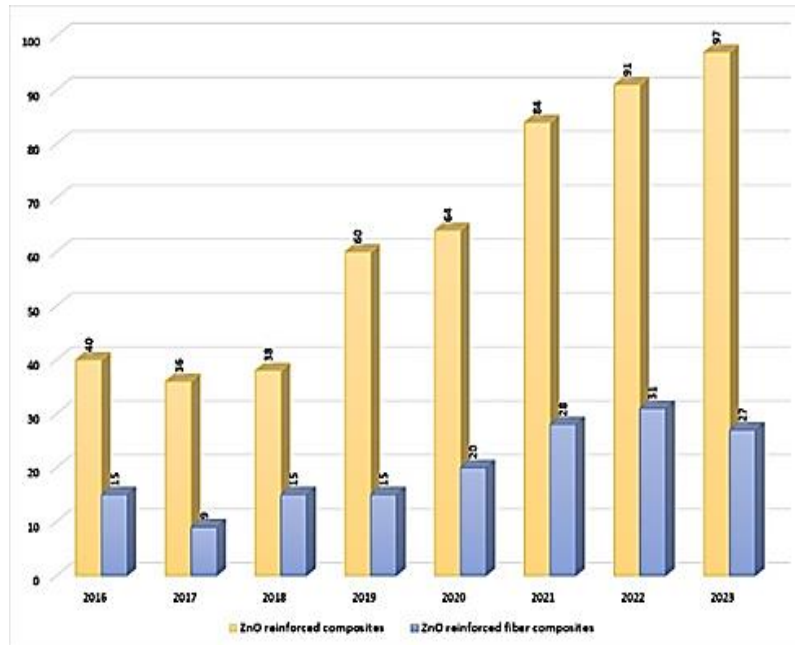


Fig. 3. Publication' evolution in WOS regarding the topics: ZnO nanoparticles and Reinforced fiber composites

By refining the results by introducing the key terms ZnO reinforced composites and ZnO reinforced fiber composites, the small number of research results is highlighted at international level in Fig. 3. The number of publications varies between 15 and 97, between 2016-2023. This leads us to the conclusion

that there are unexplored areas and emerging themes. Regarding the scientific research of the Romanian authors on the above-mentioned topics, it is noted that the elaboration and characterization of ZnO nanoparticles and reinforced composite materials were studied separately, as presented in Fig. 4.

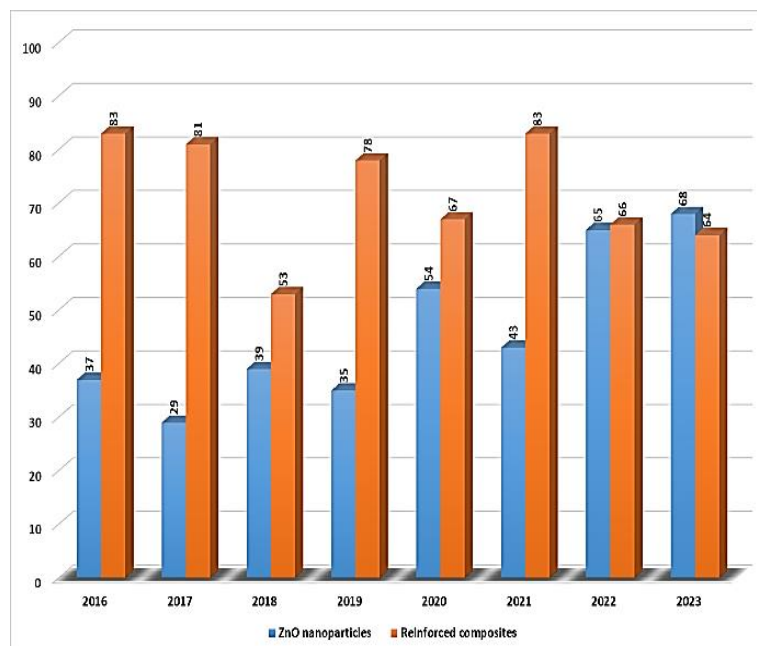


Fig. 4. Publication' evolution, Romanian authors, in WOS database

2. Characteristics of composites

2.1. Characteristics of Matrix

The classic classification of- through intergranular segregation, composites is according to the matrix, in the order of the temperature of use. Composite materials with an organic matrix can only be used on a temperature scale that does not exceed from 200 to 300 °C, while other types of composites exceed 600 °C for a metal matrix and 1000 °C for a ceramic matrix. Thus, composite materials can be classified into:

a) polymer matrix composites are certainly the most developed from the point of view of commercial importance and due to the capacity of the manufacturing process. Polymer composites have revolutionized various industries due to their superior properties compared to neat polymers.

b) metal matrix composites - some of their manufacturing processes are inspired by the processes used in powder metallurgy. The reinforcements can be oxides, borons, carbides, nitrides. Metal-matrix composites, also called MMCs (metal-matrix composites), have developed thanks to the manufacturing processes and thanks to the low costs.

c) ceramic matrix composites for high temperature applications such as oxides, carbides, or nitrides. The use of ceramics is limited precisely because of their fracture toughness, resistance to fatigue and thermal shocks. To solve these problems, the incorporation of a second ductile phase in the ceramic matrix is a solution. This process can be done in two ways:

- through intergranular segregation;
- by intragranular dispersion.

2.2. Reinforced composites

Composites offer exceptional strength and stiffness while being significantly lighter than traditional materials like metals. This makes them ideal for applications demanding weight reduction, such as aerospace, construction, sport, medicine, biomedical engineering, and automotive industries. By varying the type, amount, and orientation of the reinforcement, it can be tailoring the composite's properties to meet specific needs. For instance, unidirectional fiber orientation offers high strength in that direction, while a woven structure provides more balanced properties.

Within the vast world of reinforced composites lies a sub-category known as particle-reinforced composites. These composites, unlike their fiber-reinforced counterparts, utilize particles – typically smaller and more dispersed – to enhance the

properties of the matrix. A schema of reinforced composites is presented in Fig. 5. Large particles have diameters exceeding 1 micrometre and volume concentrations ranging from 25-50%.

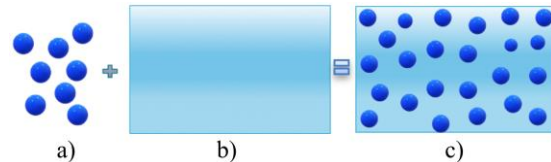


Fig. 5. Schema of particle reinforcement: a) particles; b) matrix; c) reinforced composites

Ceramic particles (oxides, nitrides, borures) are dispersed in a metal matrix, used for cutting tools due to their hardness and wear resistance.

2.3. Benefits of ZnO Armatures Particles

2.3.1. ZnO properties

ZnO is a common compound, and it's generally considered safe for human use. ZnO is a versatile and interesting material with a wide range of potential applications. ZnO can be an insulator, a semiconductor (3.37 eV, band gap), or even transparent conductor. This makes it useful in a variety of applications, from sunscreens and gels to solar cells and transistors. Also, ZnO to convert pressure into electricity, making it potentially useful for energy harvesting.

ZnO is sensitive to various gases, making it useful in gas sensors for detecting harmful gases in industrial and environmental monitoring applications.

Depending on the type of polymer matrix and the processing techniques, ZnO/polymer composites can exhibit enhanced electrical conductivity compared to the neat polymer. This opens doors for applications in antistatic materials, electromagnetic interference (EMI) shielding, and even transparent conductive films.

ZnO can absorb ultraviolet radiation, which is why it's found in many sunscreens. ZnO nanoparticles have been shown to exhibit antibacterial properties, which can be utilized in medical applications such as wound dressings, antibacterial coatings for medical devices, and textile treatments. When dispersed in a polymer matrix, they can create UV-protective films for various applications, such as coatings for sunscreens, textiles, and building materials.

ZnO nanoparticles can exhibit catalytic activity, which finds applications in environmental remediation, such as water purification and air pollution control.

Among the wide range of nanostructured metal oxides, ZnO nanoparticles can be synthesized by all synthesis methods: mechanical, chemical, physical [2, 3].

2.3.2. Methods to ZnO NP synthesis

Mechanical methods are a type of bottom-up approach for synthesizing nanoparticles. They involve applying physical forces to break down bulk materials into nanoparticles. The zinc salt or zinc oxide microparticles break down into nanoparticles, using high energy ball milling.

Hydrolysis and hydrothermal are the most common methods which use a combination of hydrolysis and condensation reactions. A soluble zinc salt, like zinc nitrate ($Zn(NO_3)_2$) or zinc acetate ($Zn(CH_3COO)_2$), is dissolved in water. This solution acts as the precursor for ZnO formation. Hydrolysis agent (like NaOH) is added to the solution, which increases the pH and initiates the hydrolysis reaction. The zinc ions (Zn^{2+}) from the precursor react with OH^- ions from hydroxide to form zinc hydroxide ($Zn(OH)_2$). $Zn(OH)_2$ further undergoes condensation reactions, where water molecules are eliminated, leading to the formation of ZnO nanoparticles. The reaction mixture is then placed in an autoclave and heated to a specific temperature (typically between 100-200 °C). The high-pressure and high-temperature conditions (in the case of hydrothermal process) promote the growth and crystallization of ZnO nanoparticles with desired size and morphology [4].

The physical methods used a focused fascicle beam on a zinc precursor target. The high energy of the beam ablates(vaporate) the target. The vapours are condensed on cooled substrate in form of films or can be collected in form of powders. Compared with already presented methods these one offers the advantage of achieving pure ZnO nanoparticles without impurities from elaboration process [3, 5].

2.4. ZnO reinforced polymer composites

2.4.1. ZnO reinforced polymer composites

ZnO reinforced polymer composites are formed by incorporating zinc oxide particles into a polymer matrix. ZnO nanoparticles can be readily incorporated into various polymer matrices using conventional processing techniques like solution casting and melt blending. ZnO nanoparticles are particularly attractive for this purpose due to their high aspect ratio and large surface area, which can lead to significant improvements in the properties of the composite material. ZnO can improve the strength, stiffness, and toughness of polymers. This is because the ZnO

particles act as stress concentrators, which transfer the applied load from the polymer matrix to the particles themselves. ZnO is a semiconductor material, which means that it can conduct electricity. This makes ZnO-reinforced polymer composites useful for a variety of electrical applications, such as electrostatic discharge (ESD) protection and electromagnetic interference (EMI) shielding. ZnO has excellent UV absorption properties, which can be beneficial for polymers that are susceptible to degradation from UV light exposure. ZnO-reinforced polymer composites can therefore be used for applications such as outdoor furniture and automotive parts.

2.4.2. Types of bonding in ZnO reinforced nanocomposites

ZnO reinforced nanocomposites are materials that combine the unique properties of zinc oxide (ZnO) nanoparticles with a polymer matrix. The incorporation of ZnO nanoparticles can significantly enhance the mechanical, electrical, and thermal properties of the composite material.

Ionic bonding occurs between positively charged ions (cations) from the ZnO nanoparticles and negatively charged ions (anions) from the polymer matrix, as presented in Fig. 6. The electrostatic attraction between these oppositely charged ions creates a strong bond at the interface between the nanoparticle and the polymer.

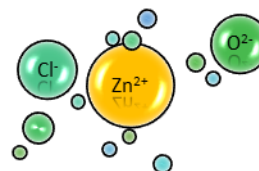


Fig. 6. Ionic bond in ZnO reinforced composites

Covalent bonding involves the sharing of electrons between atoms from the ZnO nanoparticles and the polymer matrix, as shown in Fig. 7. Covalent bonding can create very strong and directional bonds, which can improve the mechanical properties of the composite.

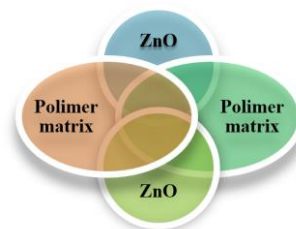


Fig. 7. Scheme of covalent bonding

Hydrogen bonding occurs between a hydrogen atom bonded to an electronegative atom (such as oxygen or nitrogen) in the polymer matrix and a lone pair of electrons on an oxygen atom from the ZnO nanoparticle, as shown in Fig. 8. Hydrogen bonding can create a weaker interaction than ionic or covalent bonding, but it can still play a role in improving the interfacial adhesion between the nanoparticle and the polymer.

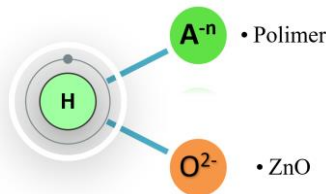


Fig. 8. Scheme of hydrogen bonding

Van der Waals forces are weak, temporary attractive forces that arise between neutral atoms or molecules. Van der Waals forces can exist between the ZnO nanoparticles and the polymer matrix, and they can contribute to the overall interfacial adhesion, as presented in Fig. 9.

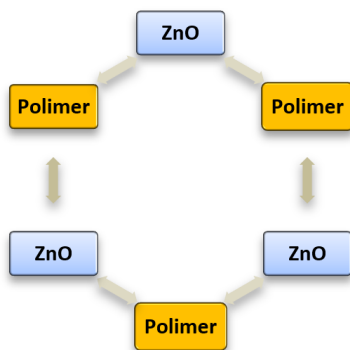


Fig. 9. Scheme of Van der Waals bonds in polymer composites

In some polymer-based composites, especially those with non-polar polymers, van der Waals forces may contribute to interactions between individual polymer chains within the matrix. This can influence the overall mechanical properties like stiffness and creep resistance of the composite. In many composites, the primary load transfer mechanism relies on stronger chemical bonds or mechanical interlocking between the fiber and matrix.

3. Multifunctional approach

Recent advancements in ZnO reinforced polymer composites focus on their enhanced

mechanical, barrier, antimicrobial, and functional properties. The synergistic effects of ZnO incorporation on the performance of various polymer matrices are explored [1, 6] This involves controlling the arrangement of ZnO particles within the composite material. Introducing nanostructures like nanorods, wires, and tubes can significantly enhance mechanical properties and electrical conductivity. Additionally, controlling the size and distribution of ZnO grains can optimize the composite's strength and toughness [7].

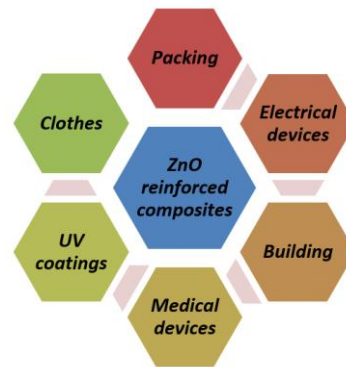


Fig. 10. Multifunctional approach of ZnO reinforced composites

Doping involves introducing foreign elements into the ZnO crystal lattice. Elements like aluminum (Al) and gallium (Ga) can create point defects that modify electrical properties, such as conductivity and carrier concentration. Alloying ZnO with other metal oxides, like magnesium oxide (MgO), can improve its stability and introduce new functionalities [3].

ZnO nanoparticles act as effective reinforcing agents, improving the tensile strength, flexural modulus, and impact strength of polymer composites. This is attributed to strong interfacial adhesion between the nanoparticles and the polymer matrix, leading to efficient stress transfer [7]. Modifying the surface of ZnO particles can enhance their compatibility with other materials in the composite or introduce entirely new functionalities. Coating ZnO with polymers or functional molecules can improve compatibility and promote specific interactions at the interface. Creating surface roughness or hierarchical structures can improve adhesion between ZnO and other phases or enhance tribological properties like wear resistance [8].

ZnO nanoparticles create an indirect path for gas molecules, significantly enhancing the gas barrier properties of polymer composites. This is particularly beneficial for food packaging applications, where it helps to maintain product freshness and extend shelf life [9]. These composites offer superior gas barrier

properties, improved mechanical strength, and inherent antimicrobial activity.

ZnO nanoparticles exhibit inherent antimicrobial activity, making the composites effective against various bacteria and fungi. This property finds applications in food packaging, medical devices, and hygiene products [6]. ZnO nanoparticles can impart various functionalities to the composites depending on their size, shape, and dispersion. For example, ZnO can enhance electrical conductivity, UV-shielding ability, and flame retardancy, opening doors for applications in electronics, sunscreens, and fire-resistant materials [10]. ZnO reinforced composites can be used in building materials to enhance their mechanical strength, UV resistance [11], and self-cleaning properties [4]. The electrical conductivity and semiconducting behavior of ZnO nanoparticles make these composites suitable for applications in sensors, solar cells, and electronic [12].

The biocompatibility and antimicrobial properties of ZnO make these composites promising candidates for drug delivery systems, implants, and wound dressings [13, 14].

4. Conclusions

Combining ZnO with other materials like polymers or ceramics allows researchers to create composites with synergistic properties. This means that the combined properties of the composite are greater than the sum of the individual components.

Perspective research in nanomaterials delves beyond the current state of the field, analysing trends and identifying future directions. It often focuses on the broader implications of nanomaterials and raises critical questions that need to be addressed for responsible development. Some perspective research in nanomaterials can be:

- Perspective research can explore ways to assess these risks, develop safer nanomaterials by design, and implement regulations for responsible use.
- Future research can identify areas for improvement, such as reducing energy use in synthesis or developing methods for safe and sustainable recycling of nanomaterials.
- Ethical regulations about their potential impact on society can focus on issues like the democratization of nanotechnology (who has access and control?), the potential for misuse in military applications, and the need for public education and engagement.
- Developing frameworks for regulation that balance innovation with risk qualification can

help the standardized methods for characterizing and testing nanomaterials.

By carefully designing the composite structure and choosing the appropriate reinforcing phases, scientists can achieve tailored electrical, mechanical, and chemical functionalities for specific applications.

References

- [1]. Kirby A., *Exploratory Bibliometrics: Using VOSviewer as a Preliminary Research Tool*, Publications, vol. 11, no. 1, p. 10, doi: 10.3390/publications11010010, Feb. 2023.
- [2]. Turlybekuly A., et al., *Synthesis, characterization, in vitro biocompatibility and antibacterial properties study of nanocomposite materials based on hydroxyapatite-biphasic ZnO micro- and nanoparticles embedded in Alginate matrix*, Materials Science and Engineering C, vol. 104, doi: 10.1016/j.msec.2019.109965, 2019.
- [3]. Schiopu A.-G., et al., *Synthesis and Characterization of ZnO-Nanostructured Particles Produced by Solar Ablation*, Materials, vol. 16, no. 19, p. 6417, doi: 10.3390/ma16196417, Sep. 2023.
- [4]. Pudukudy M., Yaakob Z., *Facile Synthesis of Quasi Spherical ZnO Nanoparticles with Excellent Photocatalytic Activity*, J Clust Sci, vol. 26, no. 4, doi: 10.1007/s10876-014-0806-1, 2015.
- [5]. Zhu Y., Tan S., Xu G., Guo T., *Effect of annealing time and annealing atmosphere on infrared emissivity property of Zn 1-x Co x O by solid state reaction*, 2017.
- [6]. Islam H., Hoque M. E., *Polymer nanocomposites for packaging*, Advanced Polymer Nanocomposites: Science, Technology and Applications, p. 415-441, doi: 10.1016/B978-0-12-824492-0.00008-8, Jan. 2022.
- [7]. Abdullin K. A., et al., *Composite materials based on nanostructured zinc oxide*, Semiconductors, vol. 48, no. 4, p. 471-475, doi: 10.1134/S1063782614040022, 2014.
- [8]. Mario J. C. C., Shaji Y. C., Brucely Y. S., Sinthuja A., Bejaxhin A. B. H., Ramanan N., *ZnO Polymer Nano Composites Synthesis, Characterization, and Thermo-Mechanical Property Comparison*, Journal of Mines, Metals and Fuels, vol. 70, no. 10, doi: 10.18311/jmmf/2022/31218, 2022.
- [9]. Olad A., Nosrati R., *Preparation, characterization, and photocatalytic activity of polyaniline/ZnO nanocomposite*, Research on Chemical Intermediates, vol. 38, no. 2, doi: 10.1007/s11164-011-0349-0, 2012.
- [10]. Theerthagiri J., et al., *A review on ZnO nanostructured materials: Energy, environmental and biological applications*, Nanotechnology, vol. 30, no. 39, doi: 10.1088/1361-6528/ab268a, 2019.
- [11]. Noreen S., et al., *ZnO, MgO and FeO adsorption efficiencies for direct sky-blue dye: Equilibrium, kinetics and thermodynamics studies*, Journal of Materials Research and Technology, vol. 9, no. 3, doi: 10.1016/j.jmrt.2020.03.115, 2020.
- [12]. Oproescu M., Schiopu A.-G., Calinescu V. M., Iana V.-G., Bizon N., Sallah M., *Influence of Supplementary Oxide Layer on Solar Cell Performance*, Engineering, Technology & Applied Science Research, vol. 14, no. 2, p. 13274-13282, doi: 10.48084/etasr.6879, Apr. 2024.
- [13]. Suryanegara L., et al., *Novel antimicrobial bioplastic based on PLA-chitosan by addition of TiO₂ and ZnO*, J Environ Health Sci Eng, vol. 19, no. 1, doi: 10.1007/s40201-021-00614-z, 2021.
- [14]. Balen R., et al., *Structural, thermal, optical properties and cytotoxicity of PMMA/ZnO fibers and films: Potential application in tissue engineering*, Appl Surf Sci, vol. 385, doi: 10.1016/j.apsusc.2016.05.122, 2016.

COMPARISON OF THE DIFFERENCE IN TEMPERATURE DISTRIBUTION ON THE SURFACE OF TWO ALUMINUM ALLOYS WELDED BY FRICTION STIR WELDING IN DIFFERENT REGIONS AT DIFFERENT LINEAR AND ROTATIONAL SPEEDS

Emad Toma KARASH¹, Amenah Faris HAMID²

¹Northern Technical University / Technical Institute Mosul, Iraq

²Northern Technical University / Technical College of Engineering - Refrigeration Department, Iraq
e-mail: ¹ emadbane2007@ntu.edu.iq, ² amina.hamed@ntu.edu.iq

ABSTRACT

Friction stir welding is a modern process that is used commercially on a large scale in various industries and in many countries to connect materials together without reaching the melting point of the metal during the welding process, so it is called the solid-state welding process.

In this research, a three-dimensional mathematical model was designed for friction stir welding of aluminium alloys (AA7075-T6 & AA2024-O) with dimensions (100 x 100 x 6 mm), using (ANSYS 15.0) program to compare the results of temperature distribution with distance from the welding centre to the end of the welded piece, as well as the temperature distribution from the beginning of the welding process to its end, using different rotational speeds (900, 1050, 1200 rpm) and different linear speeds (20, 40, 60, 100 mm/min). In the beginning, the rotational speed was fixed and the linear speed was made variable, and then the linear speed was fixed and the rotational speed was changed.

The experimental results showed that the increase in the rotation speed of the welding tool leads to an increase in the temperatures on the surfaces of the models that were welded by the friction stir welding method. Among the other results obtained, it was found that the increase in the traveling speed of the trolley carrying the models when the stir welding process decreases the temperatures on the surface of the models when the welding process is performed. We note the convergence of the theoretical results with the applied results.

KEYWORDS: AA2024-O, travel speed, ANSYS 15.0, rotational speed, friction stir welding, AA7075-T6

1. Introduction

During the friction stir welding process, the heat generated as a result of friction between the welding tool and the pieces to be welded and the plastic deformation in the welding area leads to changes in the metallurgical and mechanical properties in the welding area. These changes are affected by a number of operational and engineering factors, including the rotational velocity of the welding tool, the travel velocity of the welding table, the design and shape of the welding tool, the amount of heat entering the welding area and some other factors.

There is a different of research that has studied the stir welding processes for aluminium alloys [1]. In this study, a different rotational velocity of the

welding tool and a different velocity of the travel velocity of the cart carrying the model were used in order to know the relationship between these variables and prayer in aluminium alloy 7050. The required characteristics were obtained in this study [2]. The researcher studied the temperature of the welding tool with the friction stir welding process and modeling the process for 6061-T6 aluminium alloy. The model is developed to investigate the FSW phenomena inside the tool and work piece and the heat transfer coefficient of the aluminium alloy is improved to ($h = 2.0 \text{ kW/m}^2/\text{kW}$). The results showed that the temperature the probe is in the middle of the upper surface, 440 °C and 400 °C at the bottom of the probe and the measured surface temperature and the temperature inside the instrument are different by

about 40 °C to 50 °C [3]. The researcher has developed an analytical model for aluminium alloy AA 6061-T6 friction stir welding to simulate the contact temperature in the welding process. The results showed that the high heating temperature of the welding process not only improves the welding quality, but also reduces the processing time [4]. The researcher provided an overview and compared the methods of measuring temperature. The thermocouples included in the instrument were experimentally evaluated in two different location types. The results showed that the thermocouple temperatures inside the probe had higher readings and a faster response from the thermocouple on the shoulder. Both have lower response time and lower temperature readings during the welding process compared to TWT [5]. The researcher carried out a study on the FSW welding tool using the fluid dynamic code, FLAFT, to model a knight in a metal AA2017A box. The results showed that the best flow of materials around the welding tool, in addition to the production of a larger amount of heat in this region, and from this it is possible to estimate the temperatures more accurately through the viscosity generated near the solidus softening region [6]. The researcher studied the effect of tool rotation on temperatures during the stir welding process for copper and aluminium materials, using the CEL finite element model. The numerical model has been validated by thermal imaging and infrared thermometry. The results showed values close to the experimental temperatures that were found by numerical simulation, and the highest temperature was recorded for the joint line at a distance l [mm] behind the shoulder of the welder and the direction of the welder turn clockwise compared to the turn of the welder counterclockwise [7]. The researcher has developed a numerical model for aluminium alloy AA2024 and AA7075 based on computational fluid dynamics (CFD) to predict temperature and material distribution, flux during welding process FSW via cylindrical rotation tool. Stable plastic viscous laminate. The results indicate when increasing Tool rotation speed (TRS) and shoulder diameter (SD), during the welding process the temperature of the welding area increases and the material flow increases and when the welding speed (WS) is increased. The temperature of the welding area decreases the flow of materials in the stirring area decreases during the welding process [8, 9]. The researcher studied the so-called curing window, through which the quality is good. Friction stir welding welds can be produced from AA5083 to AA6082. To this end systematically a set of nine welds equipped using rotation speeds of 280, 560, 840 rpm and Traverse speeds of 100, 200 and 300 mm/min with AA5083 in the advanced side and nine

more with reversible material, for comparison a series smaller than the AA5083 - AA5083 and AA6082 - AA6082. It was found through the results that the temperature rise under the welding tool depends on the rotational speed compared to the travel speed [10]. The researcher conducted an experimental and numerical analysis of aluminium alloy 2195 to study the heat flux and temperature of the welding tool and work piece during the stir welding process. The results showed that the temperature resulting from the friction between the welding tool and the work piece is 5% of the tool and the rest of the heat flows into the work piece [11]. The researcher studied the material flow for friction stir welding (UFSW) of low carbon steel and how the welding process is carried out under water using a thermo mechanical model to understand the relationship between the phenomenon of thermal friction during the welding process between the welding tool and the work piece and the knowledge of welding properties. The results showed that the generated heat recorded the highest friction stir welding temperature 1228 °C and the highest friction stir welding temperature is 1008 °C. Simulation results showed the tensile strength of the steel in the stirring zone (SZ) of the FS Wed joint is higher compared to friction stir welding status. The microstructure of SZ for welded parts in the friction stir welding condition is more accurate than the friction stir welding condition because the water-cooling rate is high [12]. The researcher has developed a model in FSW of alloy AA 7068 with high strength in 3D computational fluid dynamics (CFD) to study the effect of welding tool pin profile on material flow and temperature improvement. Simulations were performed using the k-perturbative RNG model. The higher temperature obtained in the experiment is lower than the temperature obtained by simulation. The hardness was checked in different welds about 71% of the hardness of the base metal was obtained [13]. The researcher studied the heat transfer behavior of friction stir welding of aluminium alloy AA5052-AA6061 and their dimensions are 300 mm in length and 150 mm in width by determining the temperature distribution on the welded aluminium alloys and using the program ANSYS Finite Elements. The results indicate that the temperature distribution for each of the aluminium alloys AA5052 and AA6061 due to the similarity of the properties of the alloys and the maximum temperature resulting in the simulation agree with the results experimental [14]. The researcher has developed a finite element model for the friction stir welding process based on the mechanics of solid materials using ABAQUS to study the material flow for the welding process, particle tracking technology. The simulation results showed that the flow pattern the particles follow around the welder moving in a

spiral motion to the upper surface and vortex to the lower part. And the velocity of material flow to the surrounding part the welding tool is higher than the lower part of the welding tool [15]. The researcher welded aluminium alloy 2024-T4 With a thickness of 1.9 mm by friction stir welding; the tool used in the welding process is FWS-C conical probe and FWS-H hexagonal conical probe. The results for the FSW-C sample show temperatures are high at the bottom of the screw end and the temperature results for the FSW-H sample are the highest stretching temperature, from the probe tip to the adjacent area towards the forward side. The use of a hexagonal probe has a good metal effect, which increases the heat input and improves the flow of materials [16]. The researcher made a model of friction stir welding for AA6061 Alloy and AA5086, and a study of the effect of temperature on the welding tool, the displacement of the tool, and the position of the alloys. The results showed that the temperature increases in the position of the hardest aluminium alloy AA6061 on the advancing side compared to the position of the alloy on the declining side. The displacement of the tool has a significant effect on the temperature [17]. The researcher distributed the temperature on aluminium alloy 6082 during the friction process, welding noise, by placing eight thermocouples, four on the forward side and four on the back side, with different tilt angle and stopping time, the tool rotation speed is constant and travel speed. The results showed a higher temperature in the position of the alloy on the advancing side compared to its position on the retreating side. Many other studies have adopted the study of the effect of rotational speeds, linear speeds, and types of pens on temperature distribution and mechanical properties, and many metals were used, including metals subject to heat treatments, and different and valuable results were drawn for friction welding, especially for aluminium alloys [18-30].

In this study, the results of the effect of these factors on the temperature distribution on the surfaces of the welded models, and the temperature values from the starting of the welding stir friction process to the end of this process, will be presented, as well as a study of the effect of temperature changes on the surfaces of welded models in different places on the hardness resistance of these models.

Experimental work in this model included preparing aluminium sheet models (AA-2024-O & AA-7075-T6) and the models manufactured in the specified places, to know the temperature distribution during welding operation.

2. Experimental work

2.1. Metal Property

In this study, aluminium alloys (AA-2024 – O & AA-7075-T6) heat treated sheets were used as a metal base in this work. – Northern Technical University- Mosul Technical Institute Department of Mechanical Engineering - Mosul. Table 1 shows chemical analysis of alloy component proportions and their comparison with the standard ratios values approved by the European Aluminium Association (EAA). Table (2) shows a comparison of the mechanical properties of the tested alloy (AA 2024–O) with the standard values of the alloy itself according to the American specifications (ASTM E 3-01), Table 3 shown thermal properties of aluminium alloys [30-33].

Table 1. The chemical composition of aluminium alloys

Elements	Zn %	Si %	Fe %	Cu %	Mn %	Mg %	Cr %	Ti %	Al %
Nominal value AA-2024 – T6 [31 - 33]	0.21 - 0.25	0.33 - 0.5	0.41 - 0.5	3.8 - 4.9	0.3 - 0.9	1.2 - 1.8	0.08 - 0.1	0.13 - 0.25	Rem.
Actual value	0.23	0.38	0.47	4.1	0.48	1.62	0.09	0.15	92.48
Nominal value AA-7075 – O [31 - 33]	5.1 - 6.4	0.4 - 1.5	0.15 - -	1.2 - 2	0.3 - -	2.1 - 2.9	0.18 - 0.28	0.2 - -	Rem.
Actual value	5.43	0.32	0.49	1.6	0.28	2.35	0.23	0.18	89.12

Table 2. Mechanical properties of aluminium alloys

	Density, Kg/m ³	Tensile Yield Strength, MPa	Ultimate Tensile Strength MPa	% EL	Modulus of Elasticity, GPa	Shear modulus, Gpa	Hardness, Vickers	Hardness, Brinell	Poisson's ratio, μ
Nominal value, A-2024 [31 - 33]	2780	345	483	10	73.1	28	56	46	0.33
Actual value	2780	95	220	12	73.1	28	57	47	0.33
Nominal value, AA-7075 – T6 [31 - 33]	2810	503	572	5	71.7	26.9	175	150	0.33
Actual value	2840	501	570	5	71.72	26.9	177	153	0.33

Table 3. Thermal properties of aluminium alloys

	CTE, Travel 205, e ^o	Specific heat capacity, $\frac{j}{g.c^o}$	Thermal conductivity, $\frac{W}{m.c^o}$	Melting point, e ^o
Nominal value, AA-2024 – T6 [31 - 33]	24.7	0.875	121	638
Actual value	24.3	0.873	121	638
Nominal value, AA-7075 – T6 [31 - 33]	52.5	0.96	130	635
Actual value	52.6	0.97	130	635

2.2. Machines and equipment used

The traditional vertical milling machine was used to carry out all the friction stir welding operations in the mechanical workshop, and we also manufactured a simple carbon steel fixture tool for the pieces to be welded to fix the pieces during the operations. In the current study, two factors were chosen among the factors of frictional mixing processes, namely the travel velocity of the milling machine table and the rotational velocity of the friction tool, where three rotational velocity (1000, 1225, 1525 rpm) and three travel velocity (30, 40, 60 mm/min) were chosen, and the rotation was the tool is clockwise (CW) to perform the entire process of friction stir welding. Figure 1 shows the milling machine used in the friction stir welding.



Fig. 1. Milling machine used in the friction stir welding

A tit device was used to measure temperatures on the surfaces of the welded models, during the friction stir welding process, and the device measures temperatures between (-50-550 °C). Figure 2 shows device that measures the temperature by distance.



Fig. 2. Shows device those measurers the temperature by distance

Tapered threaded left-toothed with a diameter of (18 mm) and a pin with a diameter of (18 mm) and a diameter of (5.5 mm) at the base and (4.7 mm) at the end and a height of (2.9 mm), and using the tilt angle of the welding tool (tilt angle) is (2°) from the vertical axis to obtain a high quality of welding, and the tool rotates clockwise (CW). It is worth mentioning here, that the optimum value of the angle of inclination of the welding tool is within (2°-4°), and Figure 3 shows the shape and dimensions of the welding tools, while Table 4 shows the chemical composition and mechanical properties of the welding tools used in the test, and Tables 4 and 5 types of materials used in the manufacture of welding tools.

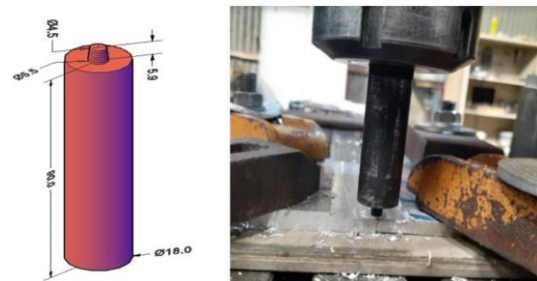


Fig. 3. shows the shape and dimensions of the welding tool, which are a cylindrical tool with a conical serrated protrusion

2.3. Materials and working methods

The metal used in this study is two aluminium alloys (AA-2024 - O & AA-7075-T6), which have poor weld ability by fusion welding methods.

The alloy plates with a thickness of (6 mm) were cut into strips and using coolant to avoid affecting their original structure by means of an electric disk saw, and the dimensions were adjusted using a milling machine to obtain the required dimensions (100 * 100 * 6 mm) and prior to the welding stir process. Friction The oxide layer is removed from the surface of the parts to be welded, especially in the joint area, using grinding paper and cleaned with acetone solution to remove dirt and contaminants. (Rolling direction) as shown in Figure 4.

The models prepared by the friction stir welding method were welded at different rotational velocity of the welding tool (1000, 1250, 1525 rpm), as well as the travel velocity of the welding table on which the welded models are fixed (20, 40, 60 mm / min) using a welding tool of length (90 mm).

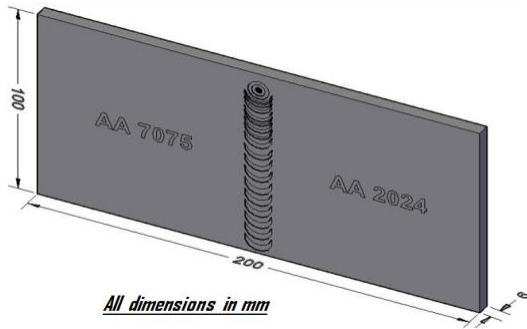


Fig. 4. Shows the shape and dimensions of the parts to be welded

2.4. Distributing temperatures when performing friction stir welding

The temperatures were measured on the surfaces of the models when friction mix welding was performed, as in Figure 5, which shows the points where the temperatures were measured for the models that were welded by friction mix welding method. Temperatures were measured using the laser device to measure the temperatures on the surfaces of the models when performing frictional mixing welding operations.

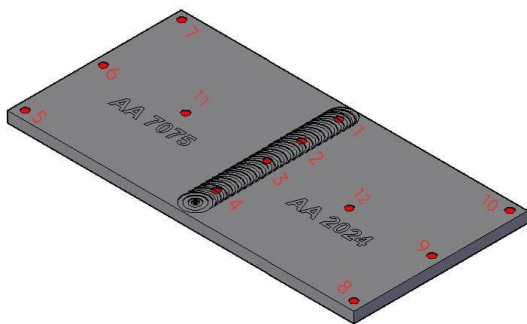


Fig. 5. Shows the points where the temperatures were measured for the models

Points on the vertical line were also determined from the starting of the friction stir welding process to the end of the welding process, and the temperatures were measured using a laser device, which are the points (1, 2, 3, 4) in order to study the effect of changing temperatures when changing the travel velocity of the welding cart and the rotational velocity of the tool. Figure 6 shows those points.

The temperatures were taken in five points on one horizontal line, which are the points between (3, 6, 9, 11, and 12) in order to study the distribution of temperatures in the middle of the welded pieces, and the Figure 7, shows those points.

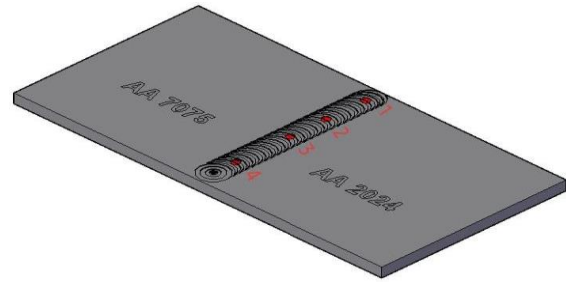


Fig. 6. shows the vertical points where the temperatures were measured for the models

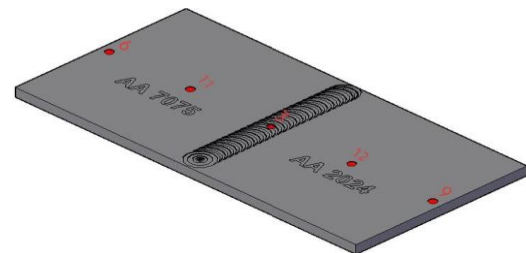


Fig. 7. shows the horizontal points that have been identified in order to take the temperature values in them

2.5. Steps to do the friction stir welding process

First, we install the two alloys with each other (1) on the cart of the milling machine, by means of the brackets of the installation tool, and we put under the alloys a sheet of steel to retain heat when performing the friction stir welding process.

Secondly, we tilt the welding tool at an angle of ($\alpha = 2^\circ$) from the vertical axis to obtain a high quality of welding.

Thirdly, we then choose the required travel velocity and rotational velocity, and the chosen travel velocity is (20, 40, 60 mm/min) and rotational velocity (1000, 1225, 1525 rpm) in each process, either the travel velocity or the rotational velocity was changed according to the work platform.

Fourth, we operate the milling machine, and then we carry out the process of lowering the tool weld down until it touches the contact area of the two alloys, and this process continues to go down until the tooth of tool enters the inside of the alloys so that the shoulder of the tool is on the surface of the two alloys by touching them, so that the metal is confined within the concavity on the shoulder of the welding tool, through the rotation of the welding tool, heat is generated and the two alloys are welded together in the contact area between them and the process takes place from starting to end, with the use of a laser device to measure the temperature in the areas identified on the surface of the alloys, and before the

welding tool reaches the end of the model by less than two millimetres, the process is stopped, the welding tool is raised and cooled in order to preserve it, Figure 8.

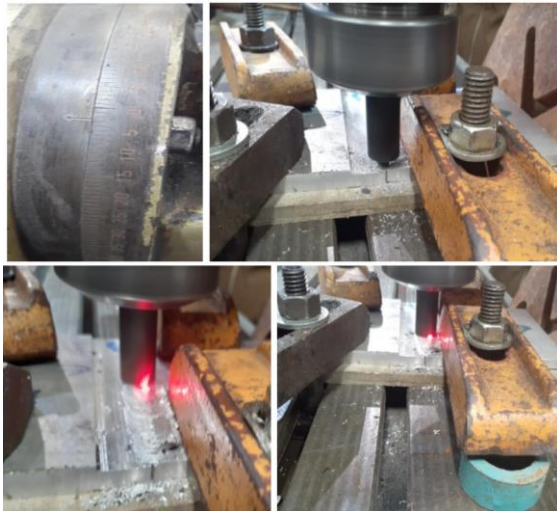


Fig. 8. It shows the method of fixing the alloys, calibration and the welding process from starting to end

3. Results and discussion

3.1. Distributing the degree of heat to the surfaces of welded patterns

After preparing the models that were composed of aluminium ingots (AA-2024 - O) and nine other models of aluminium ingots (AA-7075 T6) and after welding these pieces together by friction stir welding, at different rotational and travel velocities, welded models were obtained.

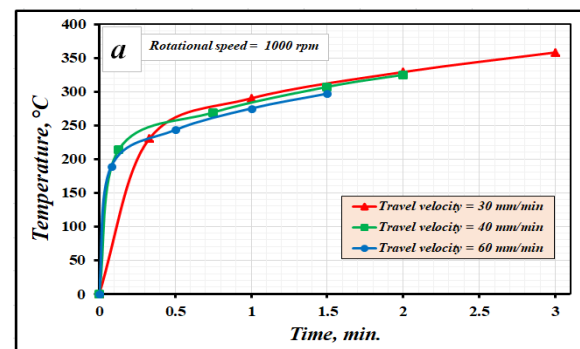
The results of the temperature distribution test on the surfaces of the models when the friction stir welding is performed for the samples appear in the Table 4.

Table 4. shows the distribution of temperatures during the friction stir welding process on the models

Model	Rotational velocity (rpm)	travel velocity (mm/min)	Temperature (°C)											
			T1	T2	T3	T4	T5	T6	T7	T8	T9	T10	T11	T12
1	1000	30	230	290	329	358	50	54	59	50	52	57	158	162
		40	214	269	307	325	50	53	57	50	51	55	145	155
		60	189	243	275	297	50	51	55	50	50	53	138	146
2	1225	30	248	324	357	375	50	58	65	50	56	62	188	182
		40	232	300	334	348	50	56	63	50	54	60	175	175
		60	214	273	308	326	50	55	60	50	52	58	162	166
3	1525	30	287	347	373	385	50	62	70	50	59	68	198	192
		40	265	328	353	363	50	60	68	50	57	65	185	185
		60	232	305	329	340	50	59	65	50	55	62	172	176

3.2. Effect of constant of rotational velocity and change of travel velocity

The results obtained in Figure 6 were analysed in the Excel program to compare these results with the Figures 9 and 10. Figure 9 shows the relationship between the time spent in the friction stir welding process of the two alloys from the starting of the welding process to its end with the temperature distribution on the welded models on the vertical line of the welding process from the starting point of the welding process to its end for different travel velocities (30, 40, 60 mm/min) and different rotation velocities of the tool welding (1000, 1225, 1525 rpm). The results indicate a decrease in temperature with an increase in the travel velocity of the trolley carrying the models and a constant rotational velocity, and this indicates a noticeable increase in temperature as the time spent in the welding process increases. It is clear from the results presented in Figure 9-a constant rotational velocity (1000 rpm) that the highest temperatures were at the traveling velocity (30 mm/min) and the time taken for the welding process (3 minute). Also, the Figure 9-b in which the constant rotational velocity was (1225 rpm) and at different travel velocity (30, 40, 60 mm/min) shows an increase in temperatures with the passage of welding time and highly during the first thirty seconds from the start of the welding process, and after that the increase is in the form of a curve and it was higher an increase in temperature when the travel velocity was (30 mm/min), where the highest value (375 °C) was recorded after a time of (3) minutes after the welding process started. Figure 9-c where the rotational velocity was constant (1525 rpm) and at different travel velocity (30, 40, 60 mm/min) shows a marked increase in temperatures with the passage of welding time and at a high velocity during the first thirty seconds of the start of the welding process and then the increase is in the form of a curve. The highest temperatures in the welding processes were recorded when the travel velocity was (30 mm/min), where the highest value was (385) after the time (3) minutes from the start of the welding process.



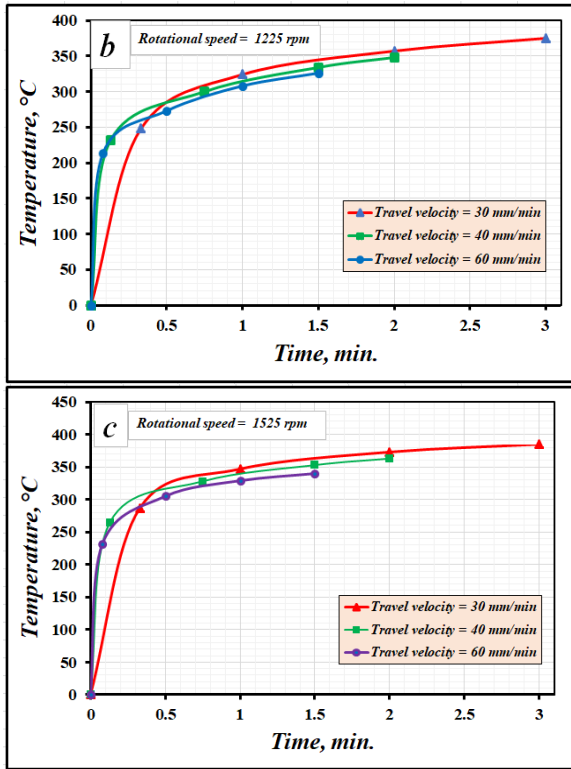


Fig. 9. shows the relationship between temperatures with time from the starting of the friction stir welding process to its end when the rotational velocity is fixed and the travel velocity change

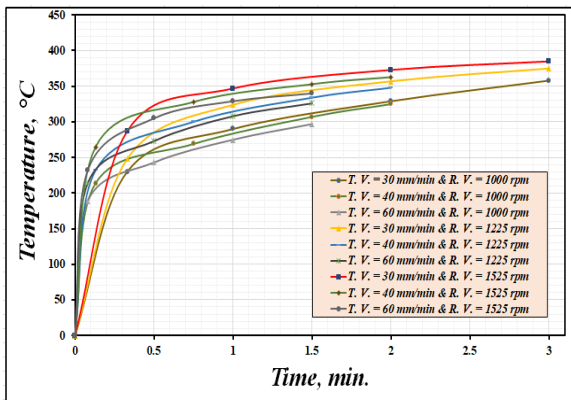


Fig. 10. Shows the temperature change over time from the starting of the welding process to its end, at variable velocities of travel and rotational

Figure 10 shows the relationship between the time spent in the friction stir welding process of the two alloys from the starting of the welding process to its end with the temperature distribution on the welded models on the vertical line of the welding process from the starting point of the welding process

to its end for different rotation velocities of the welding tool (1000, 1225, 1525 rpm) and different travel velocities of the milling trolley (30, 40, 60 mm/min). The results indicate an increase in the temperature with an increase in the time spent in the friction stir welding process, where the highest degree and its amount (385 °C) was recorded when comparing all the results obtained from the friction stir welding processes at different rotational velocities of the welding tool as well as different travel velocities.

3.3. Effect of constant of travel velocity and change of rotational velocity

The results obtained in Figure 7 were analysed in the Excel program to compare these results with the Figures 11 and 12. Figure 11 shows the results of the relationship between the time spent in the welding process, mixing friction, during the welding process from its starting to its end with the temperatures on the vertical line in the welding area, at different travel velocity of the carriage (30, 40, 60 mm/min), and different rotational velocity of the welding tool (1000, 1225, 1525 rpm). It is appeared from the results presented in Figure 11-a, at a constant travel velocity (30 mm/min) that the highest temperatures were at the travel velocity (1525 rpm) and the time taken for the welding process three minutes and its value (385 °C). Also, Figure 11-b, in which a constant travel velocity (40 mm/min) and a different rotational velocity (1000, 1225, 1525 rpm) was shown to increase in temperatures with the passage of welding time and at a high degree. During the first thirty seconds of starting the welding process and after that the increase will be in the form of a curve and the temperature increase will be higher when the travel velocity was (40 mm/min) and rotational velocity (1525 rpm), where the highest value (363 °C) after a time of two minutes after the start of the friction stir welding process.

Figure 11-c where the travel velocity was constant (60 mm/min) and at a different rotational velocity (1000, 1225, 1525 rpm), the results indicate that the highest temperature was recorded when the rotational velocity was (1525 rpm) and the highest value was recorded (340 °C) after a time of minute and a half, and this indicates that the increase in the rotational velocity and the increase in the travel velocity leads to an increase in temperatures during the welding process.

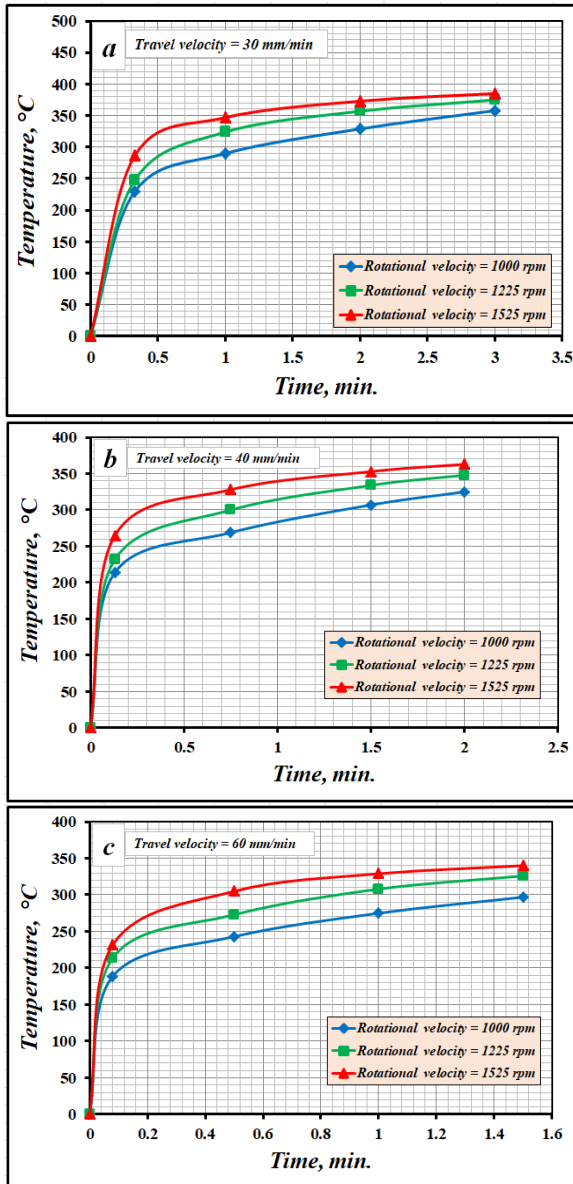


Fig. 11. Shows the relationship between temperature and time taken in the welding process from starting to end, with constant travel velocity and change in rotational velocities of the welding tool

Figure 12 shows the relationship between the time spent in the welding process of the two alloys using the friction stir welding method from its beginning to its end with the temperature distribution on the welded models on the vertical line of the welding process from the starting point of the welding process to its end for different travel velocity (30, 40, 60 mm/min) and each at a different rotation velocity of the welding tool (1000, 1225, 1525 rpm). The results indicate an increase in the temperature with an increase in the rotational velocity of the

welding tool at constant travel velocity, and this indicates a significant increase in temperature with the increase in the rotational velocity.

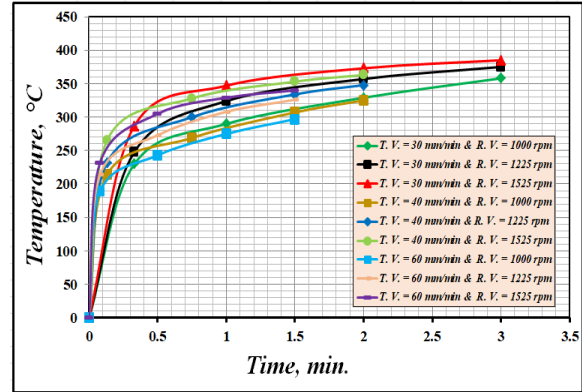


Fig. 12. Shows the temperature change over time from the starting of the welding process to its end, at variable velocities of travel and rotational

3.4. Effect of change travel velocity

Figure 7 shows the areas that have been identified in which the temperatures were measured during the friction stir welding process on a horizontal line in the middle of the models at constant rotational velocity of welding tool, and Figures 13 and 14 show those results.

Figure 15 shows the analysis of results when fixing the rotational velocity of the welding tool at (1000, 1225, 1525 rpm) and changing the travel velocity of the welding cart at each rotational velocity to compare between them, and the Figure 13-a shows the results of the temperature distribution when the rotational speed of the welding tool was (1000 rpm) and the travel speed of the welding cart (30, 40, 60 mm/min) It is evident from the figure that the highest temperature was recorded when the travel velocity of the welding cart was (30 mm/min), where the highest temperature was recorded in the welding centre and its value was (319 °C), while the lowest temperature recorded in the welding centre was when the travel velocity was (60 mm/min) and its value was (270 °C). Figure 14-b shows when the rotational velocity of the welding tool was constant at (1225 rpm) and the travel velocity of the welding cart was variable (30, 40, 60 mm/min), where the results showed that the highest temperatures were recorded when the travel velocity of the welding cart was (30 mm/min) and it was the highest value in the welding centre its value is (354 °C), while the lowest value was recorded in the welding centre when the travel velocity of the welding cart was (60 mm/min) and its value was (308 °C). Figure 14-c shows the temperature distribution

when the rotational velocity of the welding pen was (1525 rpm) and the travel velocity of the welding cart is (30, 40, 60 mm/min), and it is clear from the figure that the highest temperature recorded in the welding centre was when the travel velocity of the welding cart was (30 mm/min) and its value was (375 °C), while the lowest value was recorded in the welding centre when the travel velocity of the welding cart was (60 mm/min) and its value (335 °C).

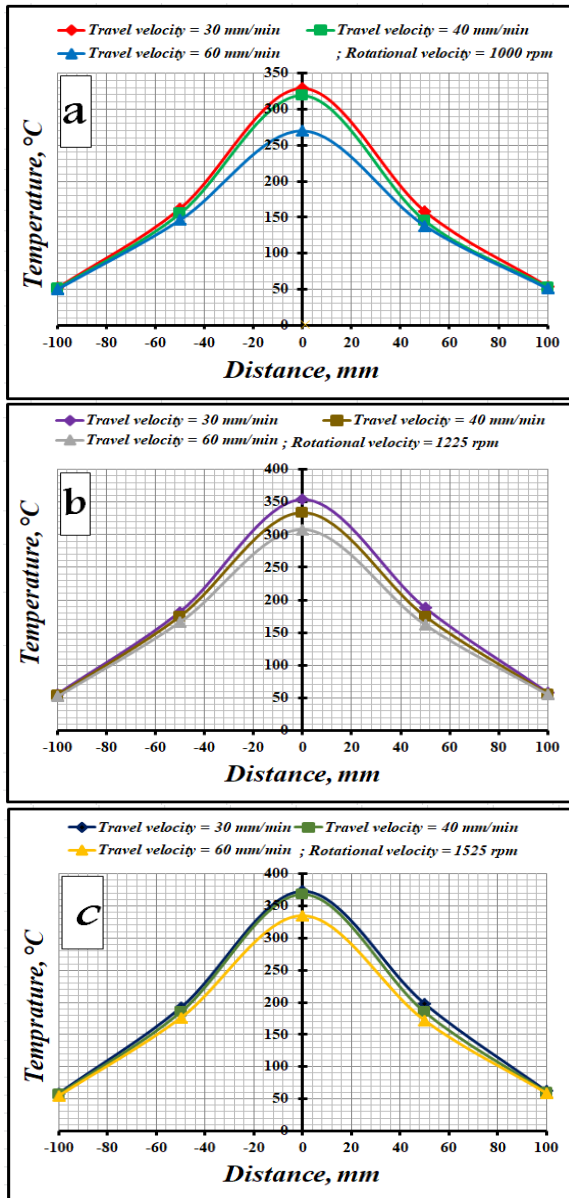


Fig. 14. The temperature distribution with the distance from the welding centre of the two alloys on the horizontal line located in the middle of the two models: a. at T.S. = 1000 rpm, b. at T.S. = 1225 rpm, c. T.S. = 1525 rpm

Figure 15 shows the results of the temperature distribution on the surface of the two alloys welded together in the friction stir welding method when the rotational velocity was variable (1000, 1225, 1525 rpm) and the travel velocity of the welding cart was also variable (30, 60, 40 mm/min), and it appears from the figure that the highest temperatures it was recorded when the rotational velocity of the welding stylus was (1525 rpm) and the rotational velocity of the welding cart (60 mm/min) where the highest value was recorded in the welding centre and its value was (373 °C) at these velocities. While the lowest value was recorded in the welding centre and its value was (270 °C) when the rotational velocity of the welding tool was (1000 rpm) and the travel speed of the welding cart was (60 mm/min). This indicates that when the rotational velocity of the welding tool is constant and the travel velocity of the welding cart changes, the temperatures decrease with the increase in the travel velocity of the welding cart, and the temperature increases with the increase in the rotational velocity of the welding tool.

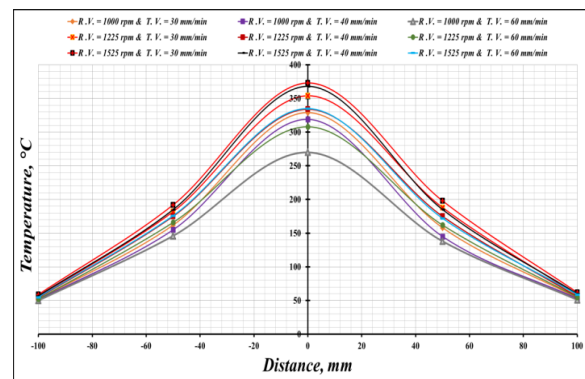


Fig. 15. Shows the temperature distribution with distance along the weld horizontal line on the centre of the models: R.V. = 1000, 1225, 1525 rpm

3.5. Effect of change rotational velocity of welding tool

Figure 7 shows the areas that have been identified in which the temperatures were measured during the friction stir welding process on a horizontal line in the middle of the models at constant travel velocity of milling cart, and Figures 16 and 17 show those results.

Figure 16 also proves these results. The (a, b, c) Figures that make up this figure show a noticeable increase in temperatures with an increase in the rotational velocity of the welding tool.

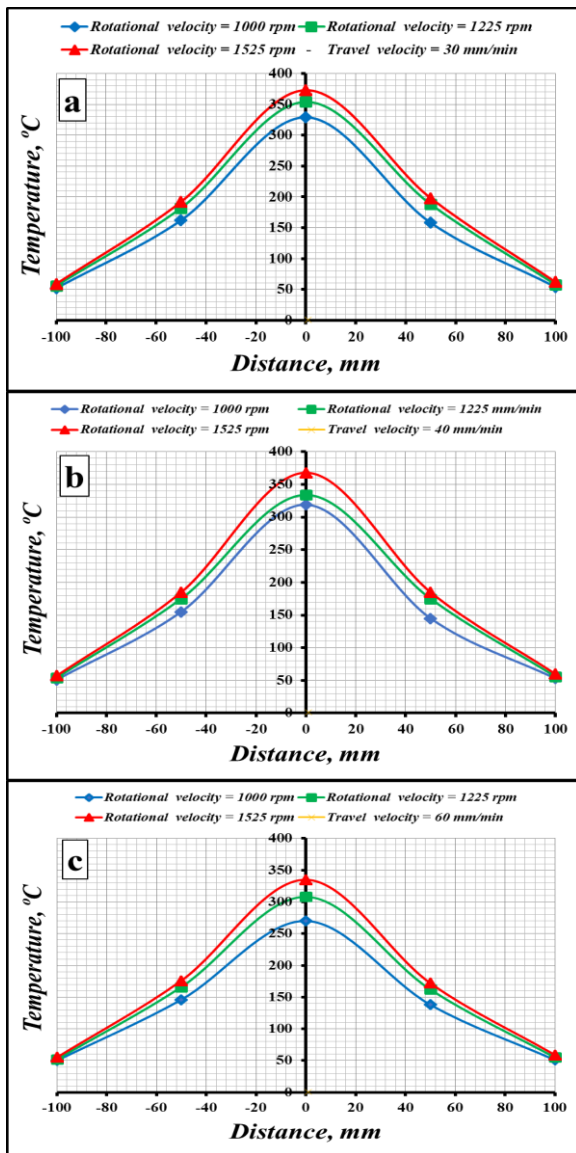


Fig. 16. The temperature distribution with the distance from the welding centre of the two alloys on the horizontal line located in the middle of the two models: a. at T.V. = 30 mm/min, b. at T.V. = 40 mm/min, c. T.V. = 60 mm/min

Figure 17 shows the results of the temperature distribution on the horizontal line passing through the middle of the models when the travel velocity of the welding cart is constant at (30, 60, 40 mm/min) and in each of them the rotary speeds of the welding stylus are changed by three different speeds which are (1000, 1225, 1525 rpm), and it appears from the figure that the highest temperatures were recorded when the travel velocity of the welding cart was equal to (60 mm/min) and the rotational speed of the welder was (1525 rpm) where the highest value was recorded

in the centre of welding and its value was (373 °C) at these speeds. While the lowest value was recorded in the welding centre and its value (270 °C) when the travel speed of the welding cart (60 mm/min) and the rotational speed of the welding tool (1000 rpm). This indicates that when the travel speed of the welding cart is constant and the rotating speed of the welding pen changes at it, the temperature increases with the increase in the rotational speed of the welding pen when the travel speed of the welding car remains constant, and the reason for this is the intensity of friction between the welding tool and the welded metal.

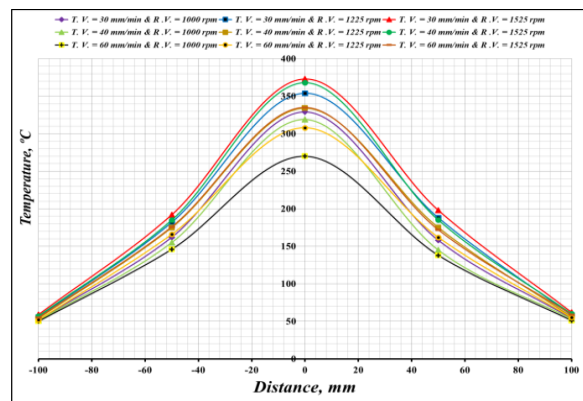


Fig. 17. Shows the temperature distribution with distance along the weld horizontal line on the centre of the models: T.V. = 30, 40, 60 mm/min

4. Conclusions

After conducting practical experiments for welding the models using the friction stir welding method, and after studying, analysing and discussing the practical results extracted from them, the following conclusions can be drawn:

1. The results showed that when the rotational speed is increased, the temperatures increase at constant travel velocity and the temperatures decrease when the travel velocity increases at constant rotational speed.

2. The lowest temperature recorded from the beginning to the end of welding was (287 °C) at a rotational speed (1000 rpm) and a constant travel speed (60 mm/min) and the time taken in the welding process was three minutes. The highest temperature recorded horizontally in the middle of the two alloys was in the welding area and its value was (373 °C) at a rotational speed (1225 rpm) and a constant travel speed (30 mm/min) while the lowest temperature was recorded horizontally in the middle of the two alloys from the weld centre to the edges of the alloy (270 °C) at a rotational velocity (1000 rpm)

and a constant travel velocity (60 mm/min), we notice that the temperatures decrease as we move away from the welding line.

3. The temperature distribution of both alloys is close to the similarity of the alloy properties, and that the temperatures of the alloy of the advance side are higher than the temperatures of the alloy of the retreating part.

4. We note the convergence of the theoretical results with the applied results.

Acknowledgment

This research was supported by Engineering Science Research Program through the Northern Technical University/ Technical Engineering college and Technical Institute of Mosul funded by the Ministry of Higher Education and Scientific Research / Republic of Iraq. (No. 00233- 2022).

References

- [1]. Reynolds A. P., Tang W., Khandkar Z., Khan J. A., Lindner K., *Relationships between weld parameters, hardness distribution and temperature history in alloy 7050 friction stir welds*, Science and Technology of Welding and Joining Journal, 10 (2), p. 190-199, 2005.
- [2]. Takashi Nakamura, Toshiyuki Obikawa, Eitaro Yukutake, Satoru Ueda, Itaru Nishizaki, *Tool Temperature and Process Modeling of Friction Stir Welding*, Modern Mechanical Engineering, 8, p. 78-94, 2018.
- [3]. Masoud Jabbari, *Effect of the Preheating Temperature on Process Time in Friction Stir Welding of Al 6061-T6*, Journal of Engineering, p. 1-5, 2013.
- [4]. Silva A. C. F., De Backer J., Bolmsjö G., *Temperature measurements during friction stir welding*, Int J Adv Manuf Technol, 88, p. 2899-2908, 2017.
- [5]. Oussama Mimouni, Riad Badji, Mohamed Hadji, Afia Kouadri-David, Hamel Rachid, Nabil Chekroun, *Numerical Simulation of Temperature Distribution and Material Flow During Friction Stir Welding 2017A Aluminum Alloys*, MATEC Web of Conferences, 80, p. 1-8, 2016.
- [6]. Iordache Monica, Nitu Eduard, Badulescu Claudiu, Iacomi Doina, Botila Lia, Radu Bogdan, *Evaluation of Thermal Distribution in Friction Stir Welding on Dissimilar Materials (Cu-Al) Using Infrared Thermography and Numerical Simulation*. Trans Tech Publications, 1138, p. 113-118, 2016.
- [7]. Padmanaban R., Ratna Kishore V., Balusamy V., *Numerical Simulation of Temperature Distribution and Material Flow During Friction Stir Welding of Dissimilar Aluminum Alloys*, Procedia Engineering, 97, p. 854-863, 2014.
- [9]. Dan Birsan, Danut Iordachescu, Jose Luis Ocana, Pedro Vilaca, *Fem model for friction stir welding of aluminum*, The Annals of "Dunarea de Jos" University of Galati Fascicle XII, Welding Equipment and Technology, Year XIX, ISSN 1221-4639, 2008.
- [10]. Peel M. J., Steuw Er A., Withers P. J., Dickerson T., Shi Q., Shercliff H., *Dissimilar Friction Stir Welds in Aa5083-Aa6082*, Metallurgical and Materials Transactions A, 37, p. 2183-2193, 2016.
- [11]. Yuh J. Chao, Qi X., Tang W., *Heat Transfer in Friction Stir Welding-Experimental and Numerical Studies*, Journal of Manufacturing Science and Engineering, 125, p. 138-145, 2003.
- [12]. Shabbir Memon, Jacek Tomk ów, Hesamoddin Aghajani Derazkola, *Thermo-Mechanical Simulation of Underwater Friction Stir Welding of Low Carbon Steel*. Materials, 14, p. 1-17, 2021.
- [13]. Bindu M. D., Tide P. S., Bhasi A. B., *Numerical Studies on Temperature and Material Flow During Friction Stir Welding using Different Tool Pin Profiles*, Journal of Advanced Research in Fluid Mechanics and Thermal Sciences, 83, p. 91-104, 2021.
- [14]. Vishwanath M. M., Lakshamananaswamy N., Ramesh G. K., *Numerical Simulation of Heat Transfer Behavior of Dissimilar Aa5052-Aa6061 Plates in Fiction Stir Welding: An Experimental Validation*, Journal of Mechanical Engineering, 2019, 69: pp. 159 – 170.
- [15]. En-zhi Gao, Xing-xing Zhang, Chun-zhong Liu, Zong-yi Ma, *Numerical simulations on material flow behaviors in whole process of friction stir welding*, Trans. Nonferrous Met. Soc. China, 28, p. 2324-2334, 2018.
- [16]. Anton Naumov, Evgenii Rylkov, Pavel Polyakov, Fedor Isupov, Andrey Rudskoy, Jong-Ning Aoh, Anatoly Popovich, Oleg Panchenko, *Effect of Different Tool Probe Profiles on Material Flow of Al-Mg-Cu Alloy Joined by Friction Stir Welding*, Materials, 14, p. 1-14, 2021.
- [17]. Amir Ghiasvand, Mahdi Kazemi, Maziar Mahdipour Jalilian, Hossein Ahmadi Rashid, *Effects of tool offset, pin offset, and alloys position on maximum temperature in dissimilar FSW of AA6061 and AA5086*, International Journal of Mechanical and Materials Engineering, 15, 6, p. 1-14, 2020.
- [18]. Vermaa S., Meenua, Misra J. P., *Study on temperature distribution during Friction Stir Welding of 6082 aluminum alloy*, Materials Today, 4, p. 1350-1356, 2017.
- [19]. Karash E. T. B., Yassen S. R., Kassim M. T. E., *Effect of friction stir welding parameters on the impact energy toughness of the 6061-t6 aluminum alloys*, Annals of "Dunarea de Jos" University, Fascicle XII ISSN 1221-4639 Welding Equipment and Technology, vol. 29, p. 27-32, 2018.
- [20]. Abdul Arif, Chetan Swaroop, Pandey K. N., *Temperature Validation for Friction Stir Welding (Fsw) of Dissimilar Aluminum Alloys*, Proceedings of International Conference on Advances in Mechanical Engineering, p. 1-10, 2013.
- [21]. Birsan D., Scutelnicu E., *Modelling of thermo-mechanical effects generated by friction spot stir welding process*, Annals of "Dunarea de Jos" University, Fascicle XII ISSN 1221-4639, Welding Equipment and Technology, vol. 25, p. 29-34, 2014.
- [22]. Bušić M., Kožuh Z., Klobčar D., *Influence of the tool travel speed on friction stir processing of aluminum alloy AlCu4Mg1*, Annals of "Dunarea de Jos" University, Fascicle XII, ISSN 1221-4639, Welding Equipment and Technology, vol. 28, p. 11-14, 2017.
- [23]. Cole E. G., Fehrenbacher A., Duffie N. A., Zinn M. R., Pfeifferkorn F. E., Ferrier N. J., *Weld temperature effects during friction stir welding of dissimilar aluminum alloys 6061-t6 and 7075-t6*, Int J Adv Manuf Technol, 71, p. 643-652, 2014.
- [23]. Birsan D., Scutelnicu E., Stan F., *Hardness of friction stir welded joints of AA-6061-t6 aluminum alloy*, Annals of "Dunarea de Jos" University of Galati, Fascicle XII, Welding equipment and technology, ISSN 1221-4639, vol. 21, 2010.
- [24]. Nageeb Salman Abtan, Ataalah Hussain Jassim, Mustafa Shakir Marmoos, *Study on the Effects of Rotational and Transverse Speed on Temperature Distribution through Friction Stir Welding of AA2024- O Aluminium Alloy*, CFD Letters, 1, p. 55-69, 2019.
- [25]. Kareem N. Salloomi, Furat I. Hussein, Sanaa N. M. Al-Sumaidae, *Temperature and Stress Evaluation during Three Different Phases of Friction Stir Welding of AA 7075-T651 Alloy*, Hindawi, p. 1-11, 2020.
- [26]. Karash E. T., Ali H. M., Hamid A. F., *Mathematical Model for the Temperature Distribution on The Surface of Two Aluminum Alloys Welded by Friction Stir Welding*, Annals of "Dunarea de Jos" University of Galati Fascicle XII, Welding equipment and technology, ISSN 1221-4639, vol. 23, 2022.
- [27]. Emad Toma Karash, Jamal Nayief Sultan, Majid Khaleel Najem, Amenah Faris Hamid, *Comparison of the Influence of Temperature Change Distribution of Three Surface Regions on the*



Hardness of Two Dissimilar Aluminum Alloys Welded by Friction Stir Welding, International Journal of Heat and Technology, vol. 40, no. 4, p. 1013-1023, August, 2022.

[28]. **Emad T. B. K., Saeed R. Y., Mohammed T. E. Q.**, *The Effect of the Cutting Depth of the Tool Friction Stir Process on the Mechanical Properties and Microstructures of Aluminum Alloy 6061-T6*, American Journal of Mechanics and Applications, 3(5), p. 33-41, 2015.

[29]. **Matweb**, *Your Source for Materials Information*, <https://www.matweb.com>, 2000.

[30]. **Mishra R., Murray S., Mahoney W.**, *Friction Stir Welding and Processing*, ASM International, USA, 2007.

[31]. ***, ASTM E 3 – 01, *Standard Guide for Preparation of Metallographic Specimens*, USA, 2001.

[32]. ***, *ASM Aerospace Specifications Metals Inc.* - retrieved 18 September 2019.

[33]. ***, *Alcoa 2024 data sheet* Archived 2006-08-27 at the Way back Machine (pdf), accessed October 13, 2006.

THE FUTURE OF CONSTRUCTION FROM A SUSTAINABLE MATERIALS PERSPECTIVE

Simona STANCA

Technical University of Cluj-Napoca, Buildings and Management Department, Romania
e-mail: simona.stanca@ccm.utcluj.ro

ABSTRACT

In the context of a growing global concern for the environment and sustainability, the construction industry is facing a key shift in the use of materials to reduce impact on the planet. The future of construction is increasingly taking shape under the imprint of material sustainability, a direction aimed at creating and using environmentally friendly and sustainable materials in the construction process. Today, the future of construction is closely linked to the use of sustainable materials and environmentally friendly practices. This paradigm shift in construction is driven by concerns about environmental impact and the need to reduce the carbon footprint of the construction industry. A sustainable approach is not just an option, but a necessity to ensure a better future and protect the environment for future generations. The future of construction under the imprint of material sustainability is a key topic in the context of global concerns about the environment and the limited resources of our planet.

KEYWORDS: the future of construction, sustainable materials, environmental impact

1. Introduction

In recent decades, the construction industry has increasingly shifted towards using sustainable materials and eco-friendly practices to reduce negative environmental impacts and improve the energy efficiency of buildings.

The materials used in construction have a significant impact on the environment and natural resources. Thus, the global trend towards the use of sustainable materials in construction is becoming more and more obvious and relevant for the future of this field [3]. From recyclable and renewable materials to technological innovations and concern for environmental impact, change in this direction is essential to build a sustainable and environmentally friendly future for future generations (Fig. 1) [6].

2. The importance of using sustainable materials in construction

In the context of climate change and sustainability concerns, the use of sustainable materials in construction has become a topic of prime importance.



Fig. 1. *The sustainable and environmentally friendly future of building materials* [6]

Sustainable materials in construction are those materials that have a low impact on the environment during the production, use and disposal process. This includes recyclable, biodegradable, low-carbon and renewable materials [4].

Below are some key aspects that highlight the importance of using sustainable materials in construction:

- *Reducing carbon footprint:*

The production and use process of traditional building materials generates significant greenhouse gas emissions [1]. Sustainable materials, such as

certified wood or recycled materials, often have a much smaller carbon footprint, helping to reduce the impact on climate change (Fig. 2) [5].



Fig. 2. Reducing carbon footprint [5]

- *Energy efficiency:*

Sustainable materials can contribute to better thermal insulation and improved energy efficiency of buildings. This reduces dependence on heating and cooling systems, thereby reducing energy consumption and associated carbon emissions (Fig. 3) [12].



Fig. 3. Energy efficiency [12]

- *Conservation of natural resources:*

The use of recycled or renewable materials contributes to the conservation of limited natural resources. Materials such as recycled concrete, recycled steel or plant-based building materials can relieve pressure on natural ecosystems (Fig. 4) [21].



Fig. 4. Recycled or renewable materials in construction [21]

- *Indoor air quality:*

Certain traditional building materials can release harmful chemicals into the indoor air of buildings, affecting air quality and the health of residents. Sustainable materials, such as organic paints or natural wood tiles, can contribute to a healthier indoor environment (Fig. 5) [10].



Fig. 5. Sustainable and sustainable materials [10]

- *Durability and wear resistance:*

Sustainable materials, when chosen and used correctly, can often offer superior durability compared to traditional materials. This helps reduce the need for maintenance and replacement, thereby reducing the long-term environmental impact (Fig. 6) [21].



Fig. 6. Durability and wear resistance of materials [21]

The use of sustainable materials in construction is an essential choice to minimize negative environmental impacts and contribute to the development of more resilient and environmentally and economically sustainable communities [2].

3. Sustainable materials used in construction

Sustainable materials in construction are an essential component of an environmentally friendly

and sustainable approach in the construction industry. These materials are selected and used to minimize environmental impact throughout their life cycle, from production to disposal.

Here are some examples of sustainable materials used in construction:

- *Wood:*

It is a sustainable option for construction, as wood is considered a renewable material and can be used instead of other, less durable or less environmentally friendly materials (Fig. 6) [11].



Fig. 7. Sustainable building with recycled or processed wood [11]

- *Bamboo:*

Being a fast-growing plant, bamboo is a great alternative to traditional wood. It is durable, resilient and has a low ecological footprint [11].



Fig. 8. Sustainable building with bamboo [11]

- *Recycled materials:*

The use of recycled materials, such as glass, recycled plastic, recycled metal or recycled concrete, helps reduce waste and reduce the impact on natural resources [20].



Fig. 9. Sustainable building with glass [20]

- *Eco-friendly insulation:*

Eco-friendly insulation materials such as sheep's wool, recycled cellulose, hemp or recycled cotton are more environmentally friendly alternatives compared to traditional insulation containing harmful chemicals [19].



Fig. 10. Sustainable building with wool [19]

- *Solar tiles and roofing materials for renewable energy:*

Integrating solar elements into the building structure can provide a sustainable energy source and help reduce the carbon footprint of the building [9].



Fig. 11. Sustainable building with solar tiles [9]

- *Traditional materials such as:*

Cob, which uses earth as a base, are sustainable options, being natural and recyclable materials [11].



Fig. 12. Sustainable building with clay [11]

The use of these materials in construction helps reduce the carbon footprint of buildings, conserve natural resources and promote a more sustainable approach to construction.

4. Trends and innovations for the future of construction from the perspective of using sustainable materials

The use of sustainable materials in construction is a major trend that will continue to develop in the future, given growing concerns about climate change and environmental sustainability. Here are some trends and innovations in the use of sustainable materials in construction for the future:

- *Recyclable and renewable materials:*

Increasing the use of recyclable materials such as recycled wood, metal, plastic and glass will reduce dependence on new materials and help reduce waste and associated carbon emissions.

- *Green concrete:*

Replacing part of concrete cement with alternative materials, such as sugar ash, rice ash or power plant ash, can reduce the carbon footprint of concrete without compromising its strength and durability.

- *Bio-based building materials:*

The use of biomass-based materials such as bamboo, hemp or straw can significantly reduce the carbon footprint of construction. These materials are renewable and can be grown quickly, making them a sustainable alternative to traditional materials.

- *Use of environmentally friendly insulating materials:*

Replacing traditional insulation with environmentally friendly materials such as cellulose wool, straw or sheep's wool fibres can improve the energy efficiency of buildings and reduce energy consumption for heating and cooling.

- *Advanced construction technologies:*

The use of advanced technologies such as digital manufacturing and 3D printing can enable buildings to be constructed quickly and efficiently using sustainable materials. These technologies can reduce construction waste and associated carbon emissions.

- *Performance monitoring and optimization buildings:*

The use of sensors and building performance monitoring systems can help to effectively identify and correct deficiencies and excessive energy consumption, helping to increase the sustainability and efficiency of buildings.

- *Circular economy in construction:*

Promoting the circular economy in construction, through the reuse and recycling of building materials and construction waste, can reduce environmental impact and conserve natural resources.

These trends and innovations demonstrate the construction industry's ongoing commitment to sustainability and responsible use of natural resources, contributing to building a more sustainable and climate-resilient future [17].



Fig. 13. Sustainable building, trend and innovation [17]

In the future, the use of innovative technologies such as 3D printing of structures is expected to increase, which can reduce waste and optimize resources. Advanced materials and smart building technologies will also be developed, which will improve energy efficiency and reduce the carbon footprint of buildings.

5. Buildings made with sustainable materials

There are many examples of buildings using innovative sustainable materials to reduce environmental impact and promote energy efficiency. Here are some examples:

- *Landform House, Singapore:*

A residential project that used recyclable materials and advanced technologies for energy efficiency, including innovative water management systems [13].



Fig. 13. Landform House, Singapore [13]

- *BedZED (Beddington Zero Energy Development), London, UK:*

It is a residential project that focuses on energy efficiency and reducing the carbon footprint, using recyclable materials, rainwater collection systems and solar panels for energy generation [8, 16].

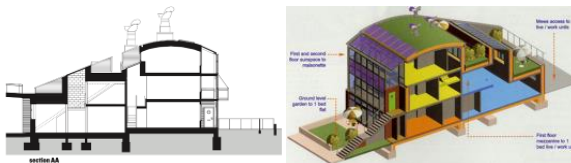


Fig. 14. BedZED (Beddington Zero Energy Development), Londra, Marea Britanie [8, 16]

- *Bamboo Sports Hall for Panyaden International School, Chiang Mai, Thailand:*

This sports hall is built entirely from bamboo, a sustainable and renewable material. Bamboo is strong, lightweight and has a low environmental impact compared to traditional materials [14].



Fig. 15. Bamboo Sports Hall for Panyaden International School, Chiang Mai, Thailanda [14]

- *Floreasca Park in Bucharest, Romania:*

Includes office buildings, green spaces and facilities designed to create a pleasant working environment. The complex is known for its contemporary architecture and is part of the city's ongoing urban development [7].



Fig. 16. Floreasca Park in Bucharest, Romania [7]

- *The Office Cluj ensemble:*

On an urban scale, evolved into a small "city within a city". The ensemble obtained the Breeam classification, thus fulfilling a series of conditions, including: an integrated system specific to a "smart" building offered by the BMS system, green terraces, passive shading systems at the most exposed facades, ventilated underground parking and naturally smoked [15].



Fig. 17. Cluj Office Ensemble [15]

6. Conclusions

The importance of using sustainable materials in construction today cannot be underestimated. It not only protects the environment, but also contributes to energy efficiency, saving resources and promoting sustainable development.

With responsibility and innovation, the construction industry can play a crucial role in creating a more sustainable future for future generations. Improving existing technologies and developing new construction methods will play a crucial role in achieving this goal. By implementing sustainable materials, buildings will become not only greener, but also more resilient, energy efficient and adapted to environmental requirements.

References

- [1]. Lin Chen, Lepeng Huang, Jianmin Hua, Zhonghao Chen, Lilong Wei, Ahmed I. Osman, Samer Fawzy, David W. Rooney, Liang Dong & Pow-Seng Yap. *Green construction for low-carbon cities: a review*, Environmental Chemistry Letters, vol. 21, p. 1627-1657, 2023.
- [2]. Stanca S., *Refurbishment of Decommissioned Buildings in the Context of Sustainable Development*, Bul. Inst. Polit. Iași, 62 (66), 1, p. 61-71, ISSN: 1224-3884 (p), ISSN: 2068-4762 (e), 2016.
- [3]. Stanca S., *Sustainability in construction*, The Annals of "Dunarea de Jos" University of Galati Fascicle IX Metallurgy and Materials Science, ISSN 2668-4748 (Print), 2668-4756 (Online) Journal volume & issue, vol. 46, no. 1, p. 10-15, 2023.
- [4]. Stanca Simona, *Improving energy efficiency in a building using passive energy-saving measures*, Journal of Applied



Engineering Sciences (JAES), ISSN: 2247-3769, e-ISSN: 2284-7197, vol. 13(26)2, 2023.

[5]. ***, <https://envirocons.ro/amprenta-de-carbon/>, accessed in 2.02.2024.

[6]. ***, <https://financiarul.ro/utile/5-materiale-ecologice-pentru-constructii-sustenabile-si-durabile/>, 2.02.2024.

[7]. ***, <https://floreascapark.ro/>, 2.02.2024.

[8]. ***, <https://inhabitat.com/bedzed-beddington-zero-energy-development-london/>, 4.02.2024.

[9]. ***, <https://mansarda-mea.ro/panourile-fotovoltaice-bramac-economiseste-astazi-pentru-un-viitor-mai-bun/>, 5.02.2024.

[10]. ***, <https://noboring.design/materiale-ecologice-si-durabile-materialele/>, 5.02.2024.

[11]. ***, <https://roxanaid.ro/constructie-sustenabila/>, 5.02.2024.

[12]. ***, <https://www.agerpres.ro/ots/2023/11/20/eficienta-energetica-si-solutii-avansate-pentru-cladiri-sustenabile--652298>, 5.02.2024.

[13]. ***, <https://www.archdaily.com/804408/landform-house-a61architects-plus-yydesign>, 7.02.2024.

[14]. ***, <https://www.archdaily.com/877165/bamboo-sports-hall-for-panyaden-international-school-chiangmai-life-construction>, 7.02.2024.

[15]. ***, <https://www.archdaily.com/888983/the-office-cluj-andreescu-and-gaivoronschi>, 7.02.2024.

[16]. ***, <https://www.architectural-review.com/buildings/bedzed-in-beddington-uk-by-zedfactory>, 8.02.2024.

[17]. ***, <https://www.blogintandem.ro/misiunea-eco-sfaturi-simple-pentru-un-stil-de-viata-sustenabil/>, 8.02.2024.

[18]. ***, <https://www.eesc.europa.eu/ro/news-media/news/constructiile-din-lemn-pot-contribui-la-reducerea-emisiilor-de-co2>, 12.02.2024.

[19]. ***, <https://www.isofoamsistem.ro/termoizolatie-cu-lana-de-oaie>, 12.02.2024.

[20]. ***, <https://www.spatulconstruit.ro/articol/o-casa-deosebita-din-sticla-si-materiale-reciclate/19138>, 12.02.2024.

[21]. ***, <https://www.styleandnature.ro/beneficiile-utilizarii-materialelor-sustenabile-in-constructii/>, 12.02.2024.

STUDIES AND RESEARCH ON THE HARDENING OF SOME INDUSTRIAL BENCHMARKS THROUGH LASER CLADDING

Simona BOICIUC

"Dunarea de Jos" University of Galati, Romania
e-mail: simona_boiciuc@yahoo.com

ABSTRACT

Industrial benchmarks are often subject to the wear and corrosion of the working environment. Laser cladding is a surface modification process that can improve their lifespan by ensuring hard, homogeneous, non-porous layers. The paper presents a series of experiments aimed at testing and calibrating the injection system used, making laser cladding with Ni-Cr-B-Fe-Al alloy on a series of industrial benchmarks and characterizing them in terms of hardness, thickness and microstructure.

KEYWORDS: laser cladding with injected powder, continuous wave laser, hardening

1. Introduction

Industrial applications require benchmarks with special surface properties such as high corrosion resistance, wear resistance and hardness. Alloys with these properties are usually very expensive and there is interest in reducing the cost of parts with these surface properties. This can be achieved by depositing, with the help of a laser beam, of a hard and corrosion-resistant layer on an inexpensive substrate [1].

Laser cladding can be accomplished through a one- or two-step process. In the one-step process, the powder is blown into the area of interaction between the laser beam and the part. In the two-step process, the powder is initially deposited on the part and then processed with the laser. Both techniques have the advantage of the possibility of depositing a wide range of alloys, either by choosing an alloy in powder form or by a mixture of powders with the required composition. Laser powder cladding offers the possibility of developing new combinations of materials in the future.

The injection of the filler material in the form of powder, in the molten metal pool, generated with the laser beam, is a widely used method for modifying the chemical composition and the properties of the superficial layer of the benchmarks made of metallic materials. The method allows direct modification of the dimensions of the deposited layer (height and width).

A number of industrial applications of laser cladding aim to increase the wear resistance of bearings, pivots, axes, cutting tools and other parts that work in very severe conditions.

Duroc AB from Sweden has developed laser cladding technologies on valves for the nuclear industry and the wood industry [1].

To perform cladding on industrial benchmarks, the laser with active gaseous medium ($\text{CO}_2+\text{He}+\text{N}_2$) with electrical excitation is used. It presents a series of features such as: good focus, very high power and high-power density, moderate efficiency, safe operation and excellent beam quality [2].

An injection system is also required, which achieves the controlled supply of the powder. There are several types of powder feeders used in industry. Depending on the principle of operation, they can be classified into the following classes: gravity driven, mechanically driven (with wheels, extruder type - with worm screw for adjusting the speed of powder supply), in fluidized bed, vibrators. Their use depends on the size, shape, physical and mechanical properties of the powders. It was found that as the powder particle size decreases below $15\mu\text{m}$, the fluidity of the powder decreases, which could affect the transport and supply of filler material during the cladding process. Thus, the use of injection systems that include pressure-assisted or vibrating feeders can ensure a continuous flow, with a uniform feed rate and a low feed rate of approx. 0.1 g/min . [2].

It was found that the use of spherical powders, obtained by gas atomization, ensures a better flow through the injection system. Also, the particles must

have a fine surface and a narrow particle size distribution [3, 4].

There is also the possibility of combining the types of feeders mentioned in order to increase the stability of the feed flow rate with filler material and the variation of the powder feed speed [2].

In worm screw feeders, there is the possibility of their premature wear, due to the abrasive effect determined by the powder particles. This aspect can influence the quality and properties of the deposited layer and can increase maintenance costs [2].

The use of fluidized bed feeders eliminates these shortcomings, thus ensuring a continuous supply of filler material, which has the effect of obtaining layers with superior characteristics [2].

Feeders with a vibrating device ensure a feed rate of filler material between 8-2000 g/min. [2].

The injection systems must ensure as continuous a supply of filler material as possible (without pulsations and agglomerations), so as to achieve complete melting of the powder particles and to obtain a compact, homogeneous layer, uniform in thickness, without pores and cracks, with a good metallurgical bond with the substrate and with a low dilution [3, 4].

Thus, there is interest in the development of new powder feeding devices for laser cladding, the main concern being directed towards the direct control of the powder flow rate and feeding speed.

It is also important, for laser cladding with injected powder, and the configuration of the filler nozzle. Thus, nozzles for co-axial feeding of the powder and for lateral feeding can be found.

One of the advantages of the co-axial nozzle is its independence from the direction of movement.

In the case of lateral feeding, surfaces with complex configurations can be processed, and by adjusting the position of the nozzle, the angle of supply of filler material, which is usually between 38 – 45° and the distance between it and the part, the cladding efficiency can be increased.

The paper presents a series of experimental research on the laser cladding of a Ni-Cr-B-Fe-Al alloy (8.9 %Cr; 4.5 %Fe; 5.1 %B; 2.4 %Al; 0.6 %Cu; and the rest Ni) on the wear elements, from the manipulators, which have the role of centring the hot-rolled strip. The program of laboratory experiments included two stages: a. testing and calibration of the injection system of the filler material in the pool melted with the laser, for the identification of constructive improvements, which would ensure the expansion of the range of regulation of the powder flow rates; b. laser cladding of nickel-based alloy layers to ensure high wear and corrosion resistance and their characterization.

2. Experimental conditions

The injection system, used in the experiments, consists of a powder storage tank, a dispenser of the amount of powder used in the unit of time, an element for directing the powder jet and a nozzle to control the divergence of this jet. Under the action of the gravitational force and the gas flow, the powder passes from the tank into the dosing chamber with a worm screw. Here it is picked up by the worm screw and transported to the jet directing element. The powder is transported from the dispenser to the work area by means of a gas flow (argon). The feed speed depends on the speed of the worm screw and its dimensions. Afterwards, the powder is injected into the pool through the nozzle.

The powder injection system in the laser molten pool and its test and calibration stand are shown in Fig. 1 and Fig. 2 [3, 5, 6].

When creating the injection system (Fig. 1), materials with higher thermal conductivity and lower specific heat (copper and copper alloys) were used for the benchmarks exposed to laser radiation.

Also, to improve the transport conditions of the powder in the system until it is taken over by the carrier fluid, an additional source of kinetic energy was introduced by placing a vibrating device at 47 Hz at the top of the tank.

For the testing and calibration research, powder with spherical particles from a nickel-based alloy, with a grain size of 80 μm, was used.

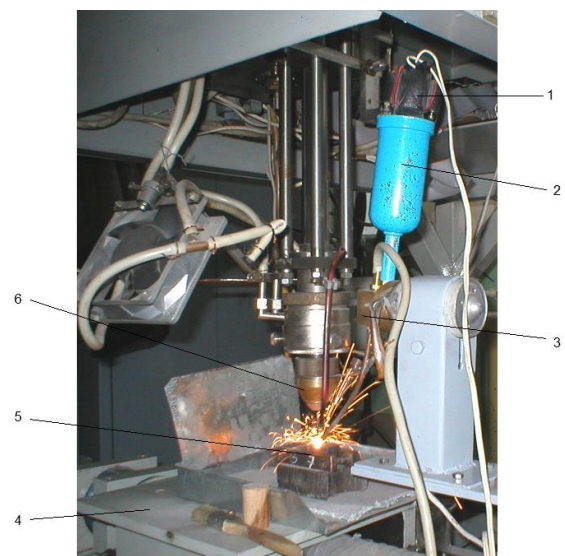


Fig. 1. The powder injection system in the laser molten pool: 1 – vibrator; 2 – tank; 3 – dispenser; 4 – table in x-y coordinates; 5 – processed sample; 6 – laser head



Fig. 2. The test and calibration stand of the injection system: 1 – tank; 2 – dispenser; 3 – direct current electric motor; 4 – directing element; 5 – laboratory beakers; 6 – powder jet; 7 – voltammeter; 8 – autotransformer; 9 – rotameter; 10 – argon cylinder

Before introducing the filler material into the tank of the injection system, the powder was dried at a temperature of 110 °C for 15 minutes. The moment of starting drying must be chosen so that, after extraction from the oven, the powder enters the processing process in a maximum of 30 minutes.

The laser claddings were carried out on the continuous wave CO₂ installation type Laser GT 1400 W (Romania), with transverse gas circulation, in cylindrical geometry, coupled to a work table in x-y-z coordinates ordered by a computer, provided by SC Uzinsider Engineering SA Galati, also provided with a powder injection system on the laser-melted surface.

The thickness of the layers deposited on the industrial benchmarks was determined at five points along each element, with the "SURFIX" SN 2731 device, and the three-point HRC hardness with the EQUOTIP durometer.

The metallographic analysis was carried out with a Philips scanning electron microscope, model XL 30ESEM TMP, resolution 3.5 nm equipped with an EDS spectrometer type EDAX Sapphire.

3. Experimental results

a. Testing and calibration of the filler material injection system: In order to test and calibrate the powder injection system in the molten metal pool with the laser beam, a laboratory stand (Fig. 2) was made consisting of the powder injection system mounted on a stand, voltammeter, autotransformer, rotameter and cylinder with argon. With the help of the autotransformer (position 8) the value of the supply voltage of the direct current electric motor (position 3) is adjusted, which is measured with the voltammeter (position 7). The flow rate of the carrier fluid, provided by the argon cylinder (position 10), is finely adjusted with the help of the rotameter

(position 9). Under the action of the worm driven by the electric motor and the pressure exerted by the argon, the powder is discharged through the nozzle in the form of a jet (position 6).

The change in the supply voltage of the electric motor determines the change in the speed of the worm screw and therefore in the powder flow rate. By changing the argon flow, the character of the powder flow through the nozzle is adjusted. Fig. 3 shows two images of the powder jet at different supply voltages and argon flow rates.

In order to test and calibrate the injection system, respectively to establish the correlation between the supply voltage of the electric motor and the powder flow rate at the exit of the nozzle, several laboratory beakers with known weight were used, in which the discharged powder was collected during the time interval of 1 minute, at different values of the supply voltage. The working parameters (from columns 1 and 2) are presented in Table 1.

Several attempts were made, and the results of the measurements (column 3) are presented in the same Table 1. The working times were timed, and the weighing was carried out with the analytical balance.



Fig. 3. Aspects of the powder jet generated at different supply voltages and argon flow rates

The literature [1, 7, 8] shows that under the conditions of using the laser beam, satisfactory deposits cannot be obtained with powder feeding speeds higher than 150 mg/s.

Comparing the values of the average flow ensured by the designed and realized injection system with the data from the literature, it results that the useful working regimes, when depositing the nickel-based powder, can be obtained by supplying the electric motor with direct current at voltages up to 15 V.

b. Laser cladding of the Ni-Cr-B-Fe-Al alloy on industrial benchmarks: For the hardening of industrial benchmarks, respectively the wear elements from the manipulators that have the role of centring the hot-rolled strip within the S.C. Liberty Steel. Galați, a Ni-Cr-B-Fe-Al nickel base alloy was used (8.9 %Cr; 4.5 %Fe; 5.1 %B; 2.4 %Al; 0.6 %Cu; and

the rest Ni), with liquid phase hardening capacity specific to laser cladding [3, 9].

The hot-rolled strip, having a temperature of 550 °C, is centered on the winding mandrel with the help of manipulators whose wear plates touch the edge of the moving strip. This results in rapid wear through

abrasion and oxidation of these plates. To increase their service life, it is necessary to deposit a superficial layer of material with superior resistance to wear and oxidation. As a result, on the guide plate, the wear elements processed by laser cladding will be mounted in the guides and fixed with bolts.

Table 1. Working parameters for testing and calibrating the powder injection system

No. item	Tension (V)	Pressure (divisions)	Filler material flow			
			Measured values (g)	Average flow (g/min)	Average flow (mg/s)	% of maximum flow
0	1	2	3	4	5	6
1	10	11	6.5840	6.5573	109.3	30.1
2			6.5571			
3			6.6258			
4			6.4622			
5	12.5	7	7.9740	7.8273	130.4	35.9
6			7.7871			
7			7.9458			
8			7.6022			
9	15	7	8.9040	8.9923	149.9	41.3
10			8.9471			
11			9.1058			
12			9.0122			
13	17.5	5	12.09399	12.32476	205.4	56.6
14			12.26713			
15			12.50579			
16			12.43216			
17	20	1	21.79399	21.77553	363.0	100
18			21.68713			
19			21.84579			
20			21.77583			



Fig. 4. The cladding process and a wear element before and after the complete processing

The wear elements and centring bolts were made of steel 1C45, SR EN 10083-1:1994 in improved condition, and the wear plates of steel S355JR, SR EN 10025+A1:1994.

In order to achieve laser cladding, the following were set: laser power 1150 W, active stroke length, number of active strokes (depending on the size of the surface on which the laser cladding is performed), transverse advance step 1.5 mm, active stroke speed 7.5 mm/s and transverse advance (10 mm/s), feed rates with filler material 105 mg/s.

The wear elements were processed by laser cladding of the hard nickel-based alloy, in the form of a thick layer of approx. 2 mm in the 2x20 mm longitudinal channel (specially provided for this purpose).

Fig. 4 shows the cladding process and a wear element before and after laser cladding of the nickel-based alloy.

Each wear element was subjected to cladding quality checks (adherence to the base material, layer thickness and hardness).

The adhesion of the deposited layers was checked with the help of penetrant liquids and the magnifying glass (x10). It was found that the deposits made are adherent, compact and have a good metallurgical bond with the substrate.

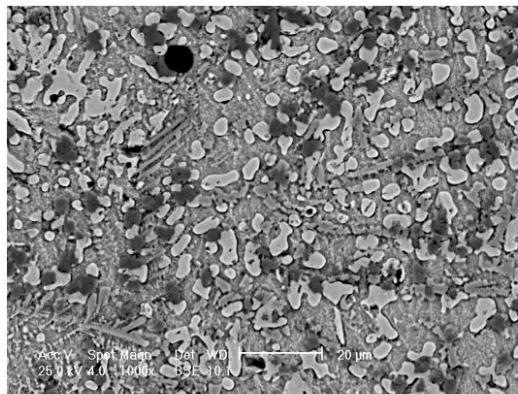
The thickness of the layer was determined at five points along each element, with the "SURFIX" SN 2731 device, and the three-point HRC hardness with the EQUOTIP durometer.

Table 2 presents the results of these determinations.

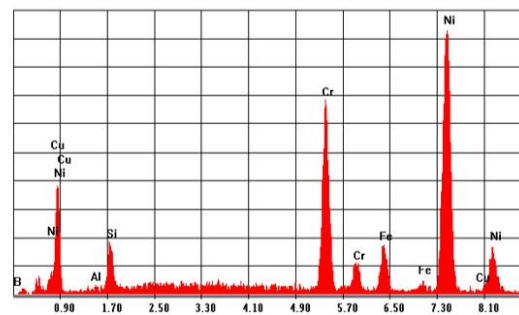
Fig. 5a shows the microstructure of the laser deposited layer with Ni-Cr-B-Fe-Al alloy and Fig. 5b the composition image obtained with the energy dispersive spectrometer.

Table 2. Characteristics of Ni-Cr-B-Fe-Al alloy cladding

No. item	Wear element	Layer thickness (mm)	Adhesion	HRC Hardness
1	Plate 1	2.1÷2.3	without detachments	68.58-66.88-67.73
2	Plate 2	2.2÷2.4	without detachments	69.58-67.72-68.65
3	Plate 3	2.1÷2.3	without detachments	68.89-67.22-68.06
4	Plate 4	2.1÷2.3	without detachments	68.00-67.44-67.72
5	Plate 5	2.1÷2.3	without detachments	69.03-66.44-67.73
6	Plate 6	2.2÷2.4	without detachments	69.05-67.92-67.00



a.



b.

Element	wt. %	At %
B K	0	0
AlK	0.52	1.02
SiK	6.07	11.52
CrK	21.33	21.85
FeK	6.56	6.26
NiK	63.86	57.95
CuK	1.66	1.39

Fig. 5. a. SEM image of the microstructure of the deposited layer; b. composition image of the analysed area obtained with the energy dispersive spectrometer

Analysing Fig. 5a. it can be seen that the microstructure of the achieved cladding is fine, with a dendritic columnar aspect, it also contains eutectic boron colonies (Ni_2B , NiB , CrB , Cr_3B_4 , FeB) dispersed in a nickel-based solid solution. Fig. 5b highlights a high content of chromium and nickel and a minimum of iron and aluminium [3].

4. Conclusions

Laser cladding is a variant of technology that ensures a superior utilization of the processed material and the expansion of the fields of use.

The testing and calibration of the injection system highlighted the fact that by supplying the electric motor with a direct current, at different voltages, different feed rates of filler material can be obtained. By correlating them with the sweeping speed and laser power, deposits with superior properties can be obtained compared to the supports used. For a good, uniform flow of the powders in the tested injection system, it is recommended to use spherical, particle size homogeneous powders, usually obtained by gas atomization.

The deposits made on industrial benchmarks are characterized by compactness, uniformity (dimensional and compositional), adhesion, with a good metallurgical bond with the substrate.

The hardening effect, conferred by the fine and dispersed structure, which contains boron (Ni_2B , NiB , CrB , Cr_3B_4 , FeB) ensures superior wear resistance and improved corrosion resistance.

References

- [1]. **Gedda H.**, *Laser surface cladding - a literature survey*, Lulea University of Technology, Division of Materials Processing, Sweden, July 2000.
- [2]. **Ehsan Toyserkani, Amir Khajepour, Stephen Corbin**, *Laser cladding*, by CRC Press LLC, 2005.
- [3]. **Boiciuc S.**, *Research on laser cladding with injected powder*, PhD thesis, Galați, 2010.
- [4]. **Salehi D.**, *Sensing and control of Nd:YAG laser cladding process*, Ph.D. Thesis, Swinburne University of Technology, Melbourne, Australia, 2005.
- [5]. **Levcovici D. T., Levcovici S. M., Onea I.**, *High speed steel plating process by laser cladding*, Patent 121477 B1 of 04.30.2007.
- [6]. **Levcovici D. T.**, *Plating with high-speed steel of the active surfaces of the tools using laser radiation*, Subcontract no. 78 to the INVENT project, S.C. Uzinsider Engineering S.A., 2004.
- [7]. **Vollertsen F., Partes K., Meijer J.**, *State of the art of Laser Hardening and Cladding*, Proceedings of the Third International WLT – Conference on Lasers in Manufacturing, Munich, June 2005.
- [8]. **Schneider M. F.**, *Laser cladding with powder*, Ph.D. Thesis University of Twente, Enschede, Netherlands, 1998.
- [9]. ***, Contract No. 10/839782/ 2007 – 2009 - *New technologies for increasing the standard duration of use of the component parts of machines and aggregates*, financing: State Budget - Ministry of Economy and Finance, value 50,000 RON, UDJ-Galati-Contractor, with S.C. Uzinsider Engineering S.A., 2007-2009.

MATHEMATICAL MODELING OF THE CuSn12 ALLOY SINTERING PROCESS

Cristian ȘTEFĂNESCU, Petrică ALEXANDRU, Gheorghe GURĂU

"Dunarea de Jos" University of Galati, Romania
e-mail: cristian.stefanescu@ugal.ro

ABSTRACT

The purpose of this study is to use statistical methods, namely active experimental regression analysis, to forecast the size of the intergranular sintering bridge by mathematically modeling the sintering process as it is applied to the CuSn12 alloy powder. A first-order linear design method was used to characterize the correlation between the intergranular sintering bridge and the sintering parameters (temperature and sintering time). Using the free casting of the powder into graphite shapes, nine experiments were scheduled. Following sintering, the intergranular sintering bridge was evaluated metallographically using image analysis software. In order to optimize the sintering process, a regression equation has been established by mathematical modeling that predicts the size of the intergranular bridge with sintering parameters (temperature and time) with a high probability (>95%), within the experimental limits.

KEYWORDS: CuSn12 powder, sintering intergranular bridge, bronze powder filter, mathematical model

1. Introduction

Powder metallurgy (PM) is a technique employed to manufacture products using metal powders. Refractory metals, high alloys, and particle composites are commonly produced by PM. These materials are challenging to manufacture using traditional metal processing methods. PM allows for the production of porous materials, such as bronze bearings and filters, with the porosity manipulated by the compaction and sintering processes. One of the benefits of the PM process is its cost-effectiveness in production, along with its ability to create intricate features and achieve high-quality surface finishes [1-3].

The PM processing variables are crucial aspects that directly impact the resulting material properties. Compaction pressure, sintering duration, and sintering temperature are a few of the processing variables. Agarwal et al. demonstrates in their review how conventional sintering affects the sintered density of premixed and pre-alloyed bronze (CuSn12) in relation to compaction pressure. Results showed that the sintered density trend for pre-alloyed and premixed bronze improved with increasing compaction pressure. Additionally, the sintered density of the pre-alloyed bronze was found to be

higher compared to the premixed bronze [4]. According to Keraghel *et al.*, the mechanical properties of the material can be enhanced by increasing the compaction pressure [5]. Adnan states that the qualities of porous bronze got better when the sintering time and temperature were increased [6]. In their study, Nakrod *et al.* examined the impact of compaction pressure and sintering time on a pre-alloyed bronze powder (CuSn10). Based on the findings, it was observed that the density of the samples rose as the compaction pressure increased [7]. Cojocaru et al. conducted a study on the impact of influencing the raw materials and sintering parameters on the porosity of sintered tin bronzes. They compared the use of mechanically pre-alloyed CuSn10 powders to a mixture of pure CuSn10 components, and varied the temperature and time of the sintering process. The relationship between these parameters has been mathematically defined [8].

The purpose of this study is to use statistical methods, namely active experimental regression analysis, to forecast the size of the intergranular sintering bridge by mathematically modeling the sintering process as it is applied to the CuSn12 alloy powder.

preventing the powder from welding to it. The mould was made up of two semi-cylindrical components. A cavity of the shape parallelepiped (38 x 4 x 1.5 mm) was machined into one of the components (Figure 2) [9].



Fig. 2. The mould with the two semi-cylindrical components used for the free casting of CuSn12 powder samples

2.3. Free casting in graphite moulds

To obtain the samples for this work, free casting in graphite moulds was opted upon. It is the simplest method for creating pieces with high porosity from powders that does not involve compression of the particles. Following the deposition of the powder into the mould cavity, a gentle vibration was induced by administering delicate impacts to the mould and the

excess was removed by scraping. Figure 2 shows the powder prepared for sintering before mounting the "cap" to close the mould cavity. The form was placed in an aluminium tube to preserve the graphite-generated reducing environment during sintering. Ceramic felt plugs were used to seal up the ends of the tube [9].



Fig. 3. The graphite mould with the powder that was ready to be sintered

2.4. Sintering

The production of sintering bridges (Figure 4) is a result of the following transport mechanisms: diffusion (surface, at grain boundaries, in volume), viscous flow, and evaporation-condensation [10].

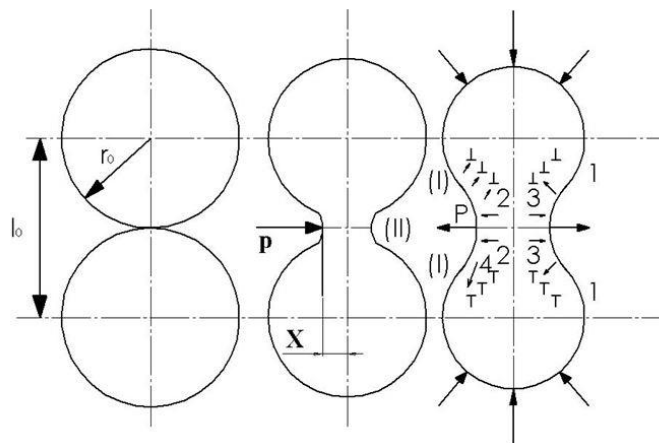


Fig. 4. Schematic illustrating how intergranular bridges form during the sintering process

The studies of the sintering process on regular geometric models of the ball-ball type, led to the establishment of the general form of the law of growth of sintering bridges (Kuczinski's equation) [10]:

$$\frac{x^n}{r^m} = k(t) \cdot \tau \quad (1)$$

where:

- x - half-thickness of the sintering bridge;
- r - radius of the powder particle;

τ - sintering time;
 $k(t)$ - coefficient depending on the sintering temperature, t ;
 n, m - constants dependent on the type of material transfer mechanism during sintering.

The LENTON tubular enclosure electric furnace was used for sintering, and the heating regime was controlled automatically (Figure 5).



Fig. 5. The furnace LENTON used for sintering

The powder and sintered samples were examined and measured using a stereomicroscope (Carl Zeiss Jena) fitted with a TOUPCAM L3CMOS14000KPA digital camera. The software

used for image acquisition and processing was TouPCam TouPView [9].

Nine experiments were scheduled (3 temperatures x 3 durations). By using optical microscopy, the sizes of the intergranular bridges ($2x$ [μm]) and the particle diameters (d_1, d_2 [μm]) they connect were determined in the sintered samples (Figure 6).

An optical micrograph of one of the sintered samples ($t = 880$ °C, $\tau = 60$ min) is shown in Figure 7.



Fig. 6. Appearance of a sintered sample

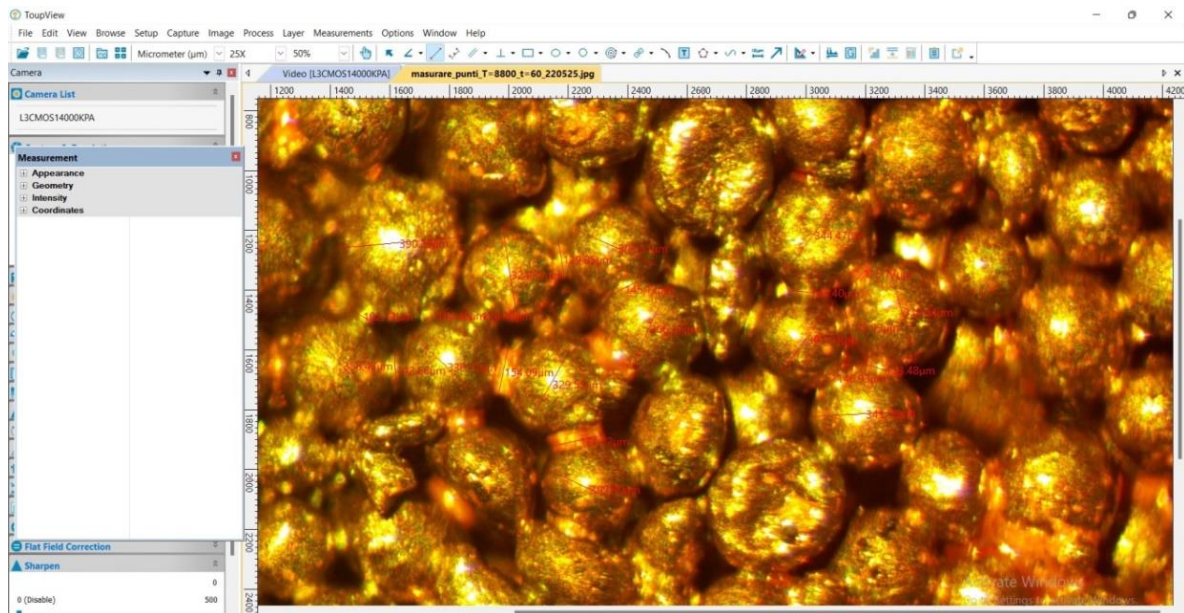


Fig. 7. Microscopic image of a sintered sample ($t = 880$ °C, $\tau = 60$ min)

For each of the 9 samples, corresponding to the experienced sintering regimes, 38 sets of measurements were made. A set includes the size of the bridge between two particles and their diameters.

Table 2 summarizes the results of the statistical analysis of the measurements taken on the 9 sintered samples in accordance with the specified experimental program.

Table 2. The average sizes of the intergranular bridges

Sample	Sintering parameters temperature, t [°C]; time, τ [min]	Average values (intergranular bridge)
		x [μm]
1	$t = 880; \tau = 20$	61
2	$t = 880; \tau = 40$	65
3	$t = 880; \tau = 60$	67
4	$t = 900; \tau = 20$	72
5	$t = 900; \tau = 40$	76
6	$t = 900; \tau = 60$	82
7	$t = 920; \tau = 20$	82
8	$t = 920; \tau = 40$	73
9	$t = 920; \tau = 60$	84

3. Results and discussion

The objective of this research is to predict the size of the intergranular sintering bridge by mathematical modeling of the sintering process applied to CuSn12 powder. This will be done by using statistical methods, namely regression analysis by active experiment. The equation of the elaborated mathematical model is of the form: $Y = f(z_1, z_2)$.

Table 3. The correspondence between the values of the influence factors expressed in natural units and coded units

Factors Levels	Process temperature		Duration of the process	
	Natural units [°C]	Coded values	Natural units [min]	Coded values
Basic level	$u_{01} = 900$	$\frac{900 - 900}{20} = 0$	$u_{02} = 40$	$\frac{40 - 40}{20} = 0$
Interval of variation	$\Delta u_1 = 20$	0	$\Delta u_2 = 20$	0
Upper level	$u_{1s} = 920$	$\frac{920 - 900}{20} = +1$	$u_{2s} = 60$	$\frac{60 - 40}{20} = +1$
Lower level	$u_{li} = 880$	$\frac{880 - 900}{20} = -1$	$u_{2i} = 20$	$\frac{20 - 40}{20} = -1$

For the coded representation of the experiment, the following notations and symbols were used:

- o independent variables:
 - z_1 - sintering temperature, t , [°C];
 - z_2 - sintering time, τ , [min];
- o Dependent variables (parameters to be optimized):
 - Y_1 - the intergranular bridge size, x [μm], of Cu Sn12 alloy powder obtained after the sintering process.

3.1. Establishing the influencing factors and the parameter to be optimized

We considered the following sintering technological parameters as main influencing factors (independent variables):

1. sintering temperature - t , [°C];
2. holding time at sintering temperature - τ , [min].

The intergranular bridge size, x [μm], of Cu Sn12 alloy powder is taken into account as a design parameter to be optimized.

We established the experimental conditions as follows:

- for sintering temperature: - base level: $u_{01} = 900$ °C;
- interval of variation: $\Delta u_1 = 20$ °C;
- for the sintering time: - basic level: $u_{02} = 40$ min;
- interval of variation: $\Delta u_2 = 20$ min;

Table 3 shows the correspondence between the different levels of the factors expressed in natural values with those expressed in coded values, for the two factors used in the sintering process.

The link between the natural and coded values is achieved through correlation:

$$Z_1 = \frac{t - t_0}{\Delta t}; Z_2 = \frac{\tau - \tau_0}{\Delta \tau} \quad (2)$$

3.2. Determination of the first-order mathematical model

Since the influence of the two factors on the performance of the process (Y) is being studied, a full

factorial experiment of type 2² was carried out. Table 4 presents the linear design matrix of the factorial experiment 2².

Considering the function Y_i as the analytical expression of the first-order model, it is of the form [11]:

$$Y_i = c_0 + \sum_{i=1}^k c_i z_i + \sum_{\substack{i=1 \\ j=1 \\ i \neq j}}^k c_{ij} z_i z_j \quad (3)$$

Table 4. The expanded linear design matrix of the 2² full factorial experiment

Factor	u ₀	Temperature t [°C] u ₁	Time, τ [min] u ₂	u ₁ u ₂	Dependent parameter intergranular bridge, x[μm]
Code	z ₀	z ₁	z ₂	z ₁ z ₂	Y ₁
Basic level, u ₀	-	900 (0)	40 (0)	-	-
Interval of variation, Δu _j	-	20	20	-	-
Upper level u ₀ +Δu _{0i}	-	920 (+1)	60 (+1)	-	-
Lower level u ₀ -Δu _i	-	880 (-1)	20 (-1)	-	-
Exp.1	+1	+1/(920)	+1/(60)	+1	84
Exp.2	+1	-1/(880)	+1/(60)	-1	67
Exp.3	+1	+1/(920)	-1/(20)	-1	82
Exp.4	+1	-1/(880)	-1/(20)	+1	61
Exp.5	+1	+1/(920)	0/(40)	0	73
Exp.6	+1	-1/(880)	0/(40)	0	65
Exp.7	+1	0/(900)	+1/(60)	0	82
Exp.8	+1	0/(900)	-1/(20)	0	72
Exp.9	+1	0/(900)	0/(40)	0	76

For the present case, the linear function (4) has the following particular form:

$$Y_1 = c_0 + c_1 z_1 + c_2 z_2 + c_{12} z_1 z_2 \quad (4)$$

Equation (5) can be written in matrix form as follows:

$$Y = Z \cdot C \quad (5)$$

Where: Z is the matrix of experimental conditions;

$$Z = \begin{pmatrix} +1 & +1 & +1 & +1 \\ +1 & -1 & +1 & -1 \\ +1 & +1 & -1 & -1 \\ +1 & -1 & -1 & +1 \\ +1 & +1 & 0 & 0 \\ +1 & -1 & 0 & 0 \\ +1 & 0 & +1 & 0 \\ +1 & 0 & -1 & 0 \\ +1 & 0 & 0 & 0 \end{pmatrix}$$

- C - the column vector of the coefficients c_i
 $C = [c_0, c_1, \dots, c_n]^T$

T - the symbol for matrix transposition;

- Y - matrix of experimental results

- $Y = [Y_1, Y_2, \dots, Y_n]^T$

- $Y = [Y_1]^T$

- $Y_1 = [84 \ 67 \ 82 \ 61 \ 73 \ 65 \ 82 \ 72 \ 76]$

Solving equation (5) using the Matlab R2016a software, the coefficients of the first-order model for property Y₁, presented in Table 5, are obtained.

Table 5. The values of the coefficients of the first-order mathematical model

Y _i	Y ₁
c ₀	73.55
c ₁	7.66
c ₂	3.00
c ₁₂	-1.00

Substituting in relation (4) we obtain:

$$Y_1 = 73,55 + 7,66z_1 + 3z_2 - z_1z_2 \quad (6)$$

By replacing the variables z_i with relations (2) in the above equation, we obtain:

$$Y_1 = 73,55 + 7,66 \frac{(t - t_0)}{\Delta t} + 3 \frac{(\tau - \tau_0)}{\Delta \tau} - \frac{(t - t_0)(\tau - \tau_0)}{\Delta t \Delta \tau} \quad (7)$$

The final form of the first-order mathematical model is obtained by replacing the values of t_0 , Δt , τ_0 , $\Delta \tau$ in equation (7).

Using equation (8) in Table 6 and Table 7 are presented the measured and calculated values of the property Y_1 , as well as data necessary to verify the adequacy of the model by calculation.

$$Y_1(t, \tau) = 73,55 + 7,66 \frac{(t - 900)}{20} + 3 \frac{(\tau - 40)}{20} - \frac{(t - 900)(\tau - 40)}{20 \cdot 20}$$

$$Y_1(t, \tau) = 73,55 + \frac{7,66t - 6894}{20} + \frac{3\tau - 120}{20} - \frac{(t\tau - 40t - 900\tau + 36000)}{400}$$

$$Y_1(t, \tau) = \frac{(40 \cdot 73,55) + 20(7,66t - 6894) + 20(3\tau - 120) - t\tau + 40t + 900\tau - 36000}{400}$$

$$Y_1(t, \tau) = \frac{29420 + 153,2t - 137880 + 60\tau - 2400 - t\tau + 40t + 900\tau - 36000}{400}$$

$$Y_1(t, \tau) = \frac{-146860 + 193,2t + 960\tau - t\tau}{400}$$

$$Y_1(t, \tau) = -367,15 + 0,483t + 2,4\tau - 0,0025t\tau \quad (8)$$

Table 6. Measured and calculated values for Y_1 (SP_{rez})

Exp.	$Y_{1measured}$ [μm]	$Y_{1calculated}$ [μm]	$Y_{1measured} - Y_{1calculated}$ [μm]	$(Y_{1measured} - Y_{1calculated})^2$ [μm]
1	84	83.21	0.79	0.6241
2	67	69.89	-2.89	8.3521
3	82	79.21	2.79	7.7841
4	61	61.89	-0.89	0.7921
5	73	81.21	-8.21	67.4041
6	65	65.89	-0.89	0.7921
7	82	76.55	5.45	29.7025
8	72	70.55	1.45	2.1025
9	76	73.55	2.45	6.0025
SUM (SP_{rez} – the sum of the squares of the residuals):				123.5561

Table 7. Measured values and their average for Y_1 obtained at the base level

No.	$Y_{01measured}$ [μm]	$Y_{01medium}$ [μm]	$Y_{01measured} - Y_{01medium}$ [μm]	$(Y_{01measured} - Y_{01medium})^2$ [μm]
1	73	73.60	-0.60	0.36
2	65	73.60	-8.60	73.96
3	82	73.60	8.40	70.56
4	72	73.60	-1.60	2.56
5	76	73.60	2.40	5.76
SUM (SP_{er} – the sum of squared errors):				153.20

3.3. Verification of model adequacy

A model is considered adequate if:

$$F_{ci} < F_T(f_{in}, f_{er}, 95\%) \quad (9)$$

where:

$- F_T(f_{in}, f_{er}, 95\%) = F_T(1,4,95\%) = 7.71$,
 represents the value of the Fischer criterion adopted from the tables of the Fischer distribution [11];

$$- F_{ci} = -0,77$$

The values calculated with the relations above are centralized in Table 8.

Table 8. Sizes calculated to check the model's adequacy

Terms	Calculation relation	Calculated values
SP_{rez} (Sum of squares of residuals)	Table 6	123.56
PM_{rez} (Mean square of residuals)	$PM_{rez} = \frac{SP_{rez}}{f_{rez}} = \frac{SP_{rez}}{5}$	24.71
SP_{er} (Sum of squared errors)	Table 7	153.20
PM_{er} (Mean square of errors)	$PM_{er} = \frac{SP_{er}}{f_{er}} = \frac{SP_{er}}{4}$	38.30
SP_{in} (Mean square of inadequacy)	$SP_{in} = SP_{rez} - SP_{er}$	-29.64
PM_{in} (Mean square of inadequacy)	$PM_{in} = \frac{SP_{in}}{f_{in}} = \frac{SP_{in}}{1}$	-29.64
F_{ci} (Value of Fischer's criterion)	$F_{ci} = \frac{PM_{in}}{PM_{er}}$	-0.77
$F_T(f_{in}, f_{er}, 95\%)$		7.71
Concordance $F_{ci} < F_T(1,4,95\%)$		Concord

3.4. Verification of the statistical significance of coefficients

The c_i coefficients are considered significant for which: $F_{csi} > F_T(1, f_{rez}, (1 - \alpha)\%)$.

In the present case: $F_T(1, 5, 95\%) = 6,61$ [11], so:

$$F_{csi} = \frac{PM_{ci}}{PM_{rez}} > 6,61 \quad (10)$$

PM_{ci} is the mean square of the coefficients that are calculated with the matrix relationship:

$$PM_{ci} = D_i(Z^t Y) \quad (11)$$

where:

- D_i is the diagonal matrix having as elements of the main diagonal the model coefficients, the other elements of the matrix being null, Z is transposed to the matrix of experimental conditions at the considered levels (-1,0,1);

- Y is the matrix of experimental results at the considered levels (-1,0,1).

For the equation of the mathematical model considered, the diagonal matrix D_i , has the following form:

$$D_1 = \begin{vmatrix} 73,55 & 0 & 0 & 0 \\ 0 & 7,66 & 0 & 0 \\ 0 & 0 & 3 & 0 \\ 0 & 0 & 0 & -1 \end{vmatrix}$$

The matrix calculation was performed using the MATLAB R2016a software, and the results are presented in Table 8.

Table 9. The values of the F_{csi} report

c_i	c_0	c_1	c_2	c_{12}
F_{csi}	1970.4614	14.259814	2.1853501	0.1618778

Analysing the F_{csi} report data from Table 9, shows that:

- The calculated values are strongly influenced by the terms which are preceded by the coefficients c_0 and c_1 for the equation of the mathematical model considered;
- The term which is preceded by the c_2 coefficient has a relatively low influence;
- The term which is preceded by the c_{12} coefficient has a negligible influence.

Considering the above, the equation of the mathematical model written without the terms whose influence is negligible can be considered as viable. Thus, the form of equation (6), without the term preceded by the coefficient c_{12} , becomes:

$$Y_i = 73,55 + 7,66z_1 + 3z_2 \quad (12)$$

The transformation of equation (12) into an equation with natural variables is done starting from the conversion relations (2), relations that correspond to the data presented in Table 3 and we obtain the relation:

$$Y_1(t, \tau) = 73,55 + 7,66 \frac{(t - 900)}{20} + 3 \frac{(\tau - 40)}{20} = 73,55 + \frac{7,66t - 6894}{20} + \frac{3\tau - 120}{20}$$

$$= \frac{1471 + 7,66t - 6894 + 3\tau - 120}{20} = \frac{-5543 + 7,66t + 3\tau}{20}$$

$$Y_1(t, \tau) = -277,15 + 0,383t + 0,15\tau \quad (13)$$

Equation (13) represents the first-order mathematical model of the studied process valid for $t = 880-920$ °C and $\tau = 20-60$ min (the definition domain of the functions).

3.5. Results obtained

Table 10 and Table 11 show the values of the analysed factor ($Y_1 = x$), calculated with the equation above, for different values of the sintering parameters (t and τ) and the graphs shown in Figures 8-13.

Table 10. Calculated $Y_1 = f(t)$ for $\tau = 20$ min; $\tau = 40$ min; $\tau = 60$ min

Intergranular bridge [μm]		$Y_1 = f(t)$ $\tau = 20$ min			$Y_1 = f(t)$ $\tau = 40$ min			$Y_1 = f(t)$ $\tau = 60$ min		
		Temperature t [°C]			Temperature t [°C]			Temperature t [°C]		
		880	900	920	880	900	920	880	900	920
Calculated	62.89	70.55	78.21	65.89	73.55	81.21	68.89	68.89	84.21	
Measured	61.00	72.00	82.00	65.00	76.00	73.00	67.00	82.00	84.00	
Graph	Figure 8			Figure 9			Fig. 10			

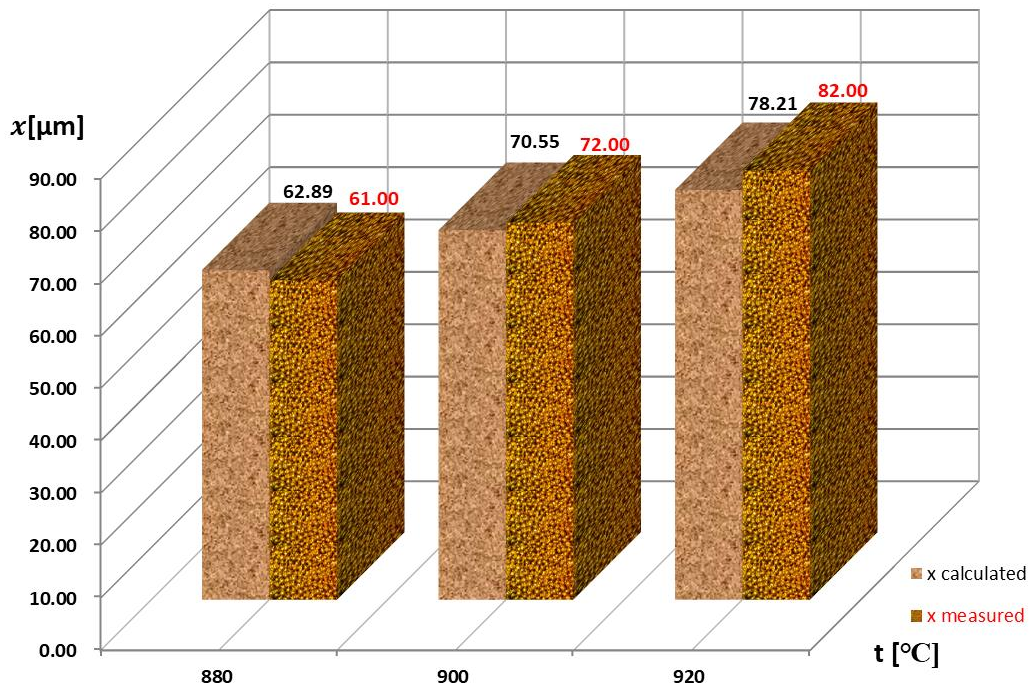


Fig. 8. $Y_1 = f(t)$ for $\tau = 20$ min

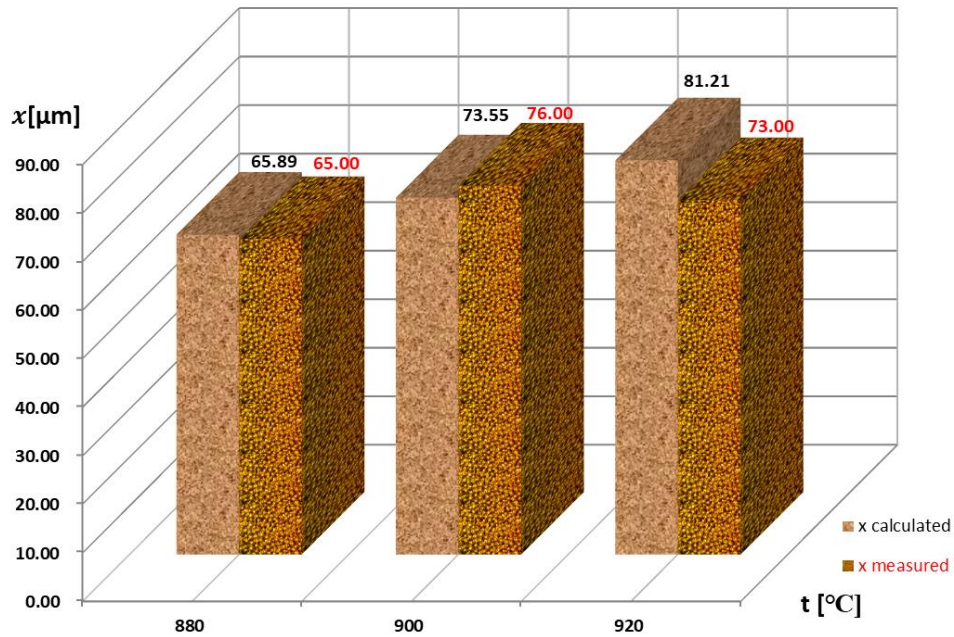


Fig. 9. $Y_1 = f(t)$ for $\tau = 40$ min

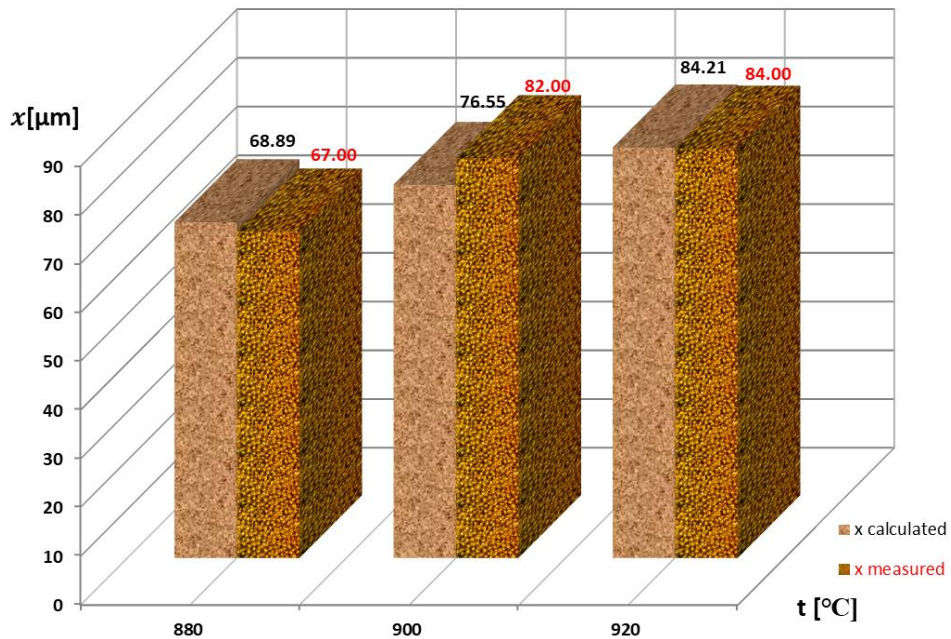


Fig. 10. $Y_1 = f(t)$ for $\tau = 60$ min

Table 11. Calculated $Y_1 = f(\tau)$ for $t = 880$ °C; $t = 900$ °C; $t = 920$ °C

Intergranular bridge [μm]		$Y_1 = f(\tau)$ $t = 880$ °C			$Y_1 = f(\tau)$ $t = 900$ °C			$Y_1 = f(\tau)$ $t = 920$ °C		
		Sintering time, τ [min]			Sintering time, τ [min]			Sintering time, τ [min]		
		20	40	60	20	40	60	20	40	60
Graph	Calculated	62.89	65.89	68.89	70.55	73.55	76.55	78.21	81.21	84.21
	Measured	61.00	65.00	67.00	72.00	76.00	82.00	82.00	73.00	84.00
Graph		Figure 11			Figure 12			Figure 13		

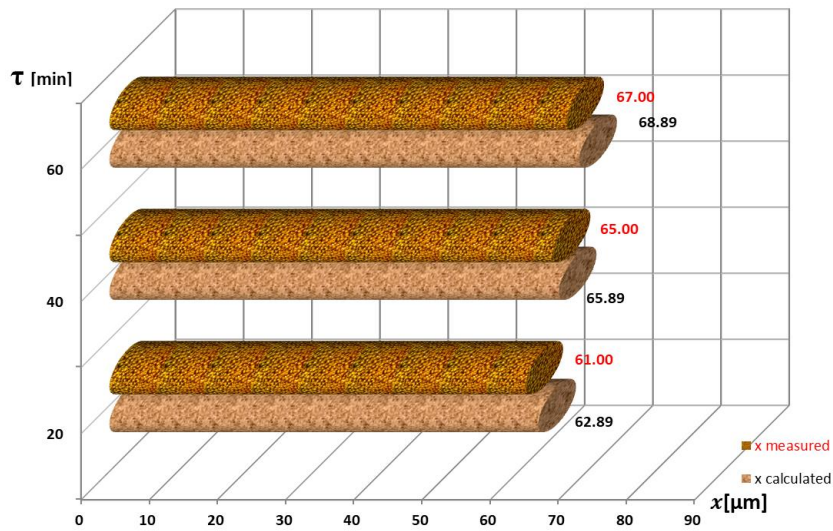


Fig. 11. $Y_1 = f(\tau)$ for $t = 880\text{ }^\circ\text{C}$

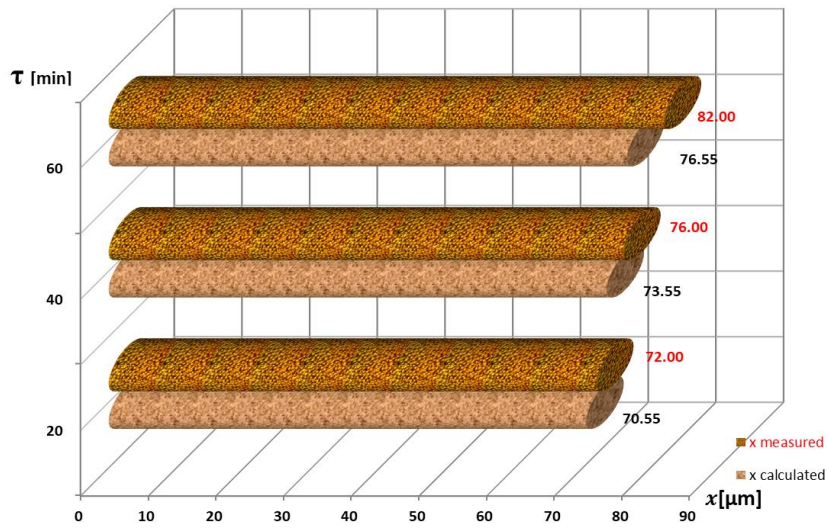


Fig. 12. $Y_1 = f(\tau)$ for $t = 900\text{ }^\circ\text{C}$

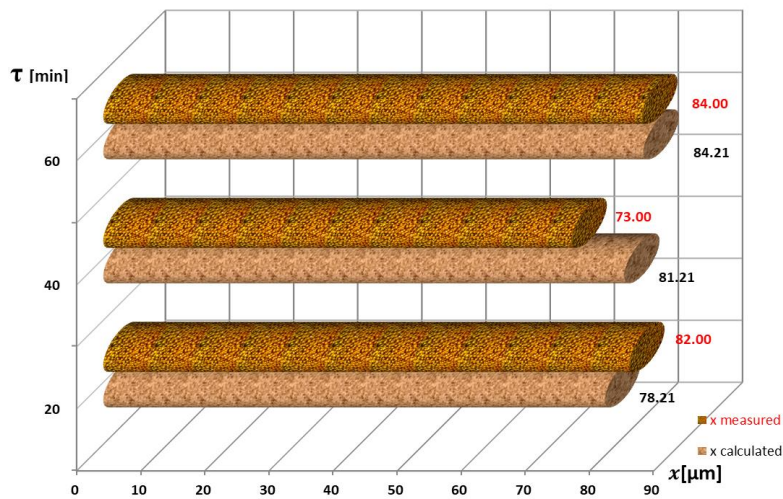


Fig. 13. $Y_1 = f(\tau)$ for $t = 920\text{ }^\circ\text{C}$

Based on the regression equation of the mathematical model obtained, we created an application in MATLAB R2016a that can make a prediction of the value of the intergranular bridge (x)

in the range $t = 880-920$ °C and $\tau = 20-60$ min. Figures 14 and 15 show some images with simulations performed with this application.

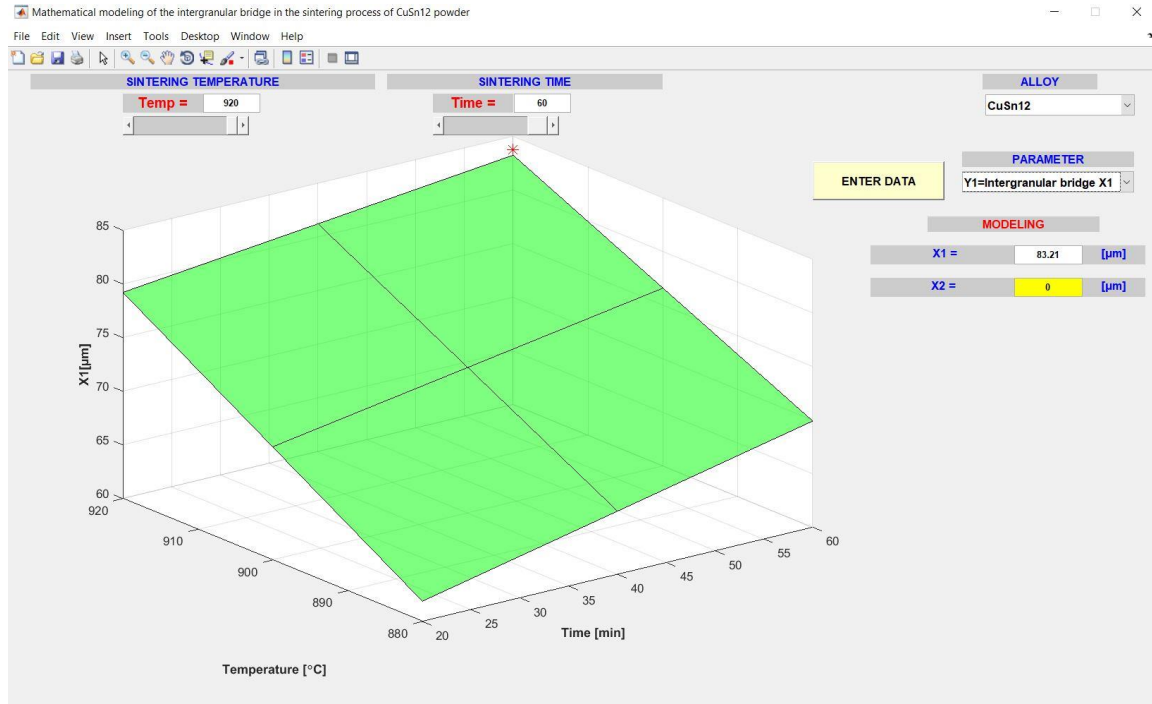


Fig. 14. Prediction of the value of the intergranular bridge x_1 for $t = 920$ °C and $\tau = 60$ min calculated with the regression equation (8)

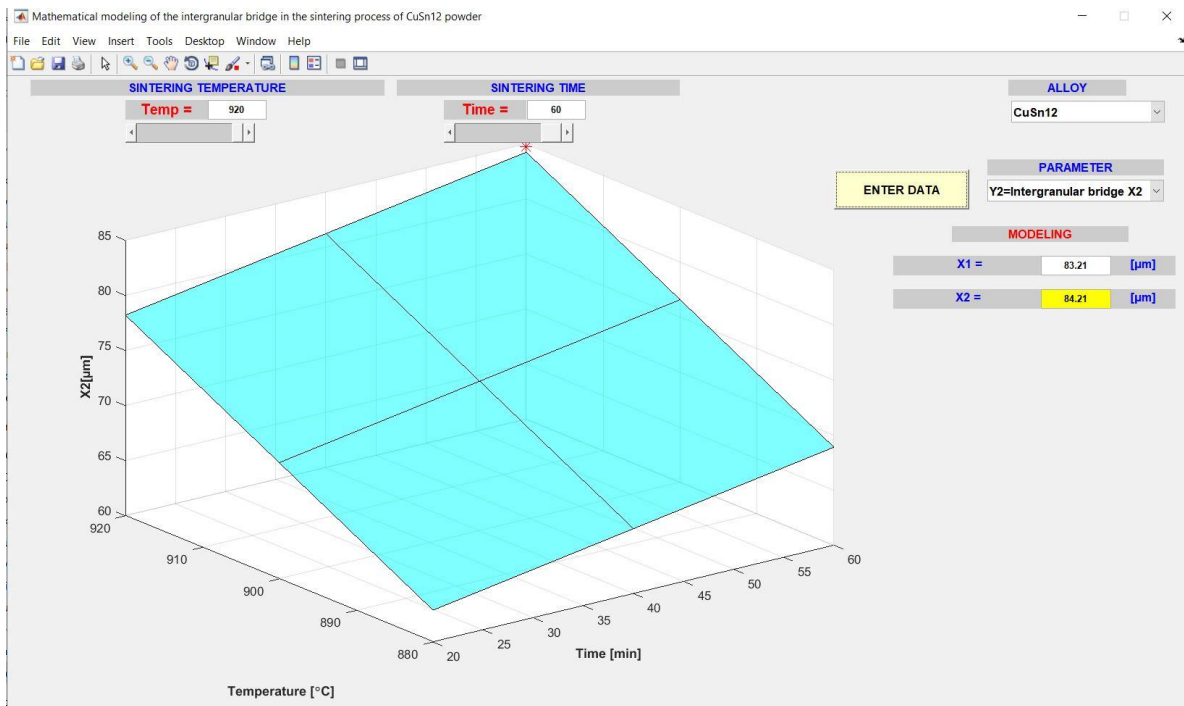


Fig. 15. Prediction of the value of the intergranular bridge x_2 for $t = 920$ °C and $\tau = 60$ min calculated with the regression equation (13)

4. Conclusions

As can be seen from Tables 10 and 11, the calculated values for the intergranular sintering bridge (x) are very close to the measured values, so the first-order mathematical model described by equation (13) allows the simulation of the sintering process of the CSn12 powder, by the variation of the technological parameters, t and τ , within the experienced limits.

It is noted, as expected, the much greater influence of the temperature factor than the time factor on the sintering process, represented by the evolution of the size of the intergranular sintering bridge.

The application made in MATLAB R2016a uses the two forms of the regression equation, (8) and (13) of the obtained mathematical model and can make predictions, with a high probability (>95%) of the size of the intergranular bridge in the interval $t = 880-920$ °C (with a variation $\Delta t = 5$ °C) and $\tau = 20-60$ min (with a variation $\Delta \tau = 10$ min).

References

- [1]. ***, *Friction Lubrication and Wear Technology*, ASM Handbook, vol. 18, p. 801-811, 1992.
- [2]. ***, *Powder Metal Technologies and Applications*, ASM Hand Book, vol. 7, p. 343-348, 2572-2599, 1998.
- [3]. Suresh A. L., Mahendran S. K. R., Krupashankara M. S., *Influence of Powder Composition & Morphology on Green Density for Powder Metallurgy Processes*, Int. J. Innov. Res. Sci. Eng. Technol., vol. 04, no. 01, p. 18629-18634, doi: 10.15680/ijirset.2015.0401037, 2015.
- [4]. Sethi G., Upadhyaya A., Agrawal D., *Microwave and conventional sintering of premixed and prealloyed Cu-12Sn Bronze*, Sci. Sinter., vol. 35, no. 2, p. 49-65, doi: 10.2298/SOS0302049S, 2003.
- [5]. Keraghel F., Loucif K., Delplancke M. P., *Study of bronze porous alloy Cu-Sn worked out by metallurgy of the powders*, Phys. Procedia, vol. 21, p. 152-158, doi: 10.1016/j.phpro.2011.10.023, 2011.
- [6]. Jabur A. S., *Effect of powder metallurgy conditions on the properties of porous bronze*, Powder Technol., vol. 237, p. 477-483, doi: 10.1016/j.powtec.2012.12.027, 2013.
- [7]. Nakrod N., McCuiston R., Auechaltanukul C., *Effect of compaction pressure and sintering time on the properties of sintered Cu-10Sn bronze*, Key Eng. Mater., vol. 751 KEM, p. 37-41, doi: 10.4028/www.scientific.net/KEM.751.37, 2017.
- [8]. Cojocaru M. O., Druga L. N., Dragomir D., Tudose F., *Porosity of sintered tin bronzes*, UPB Sci. Bull. Ser. B Chem. Mater. Sci., vol. 79, no. 1, p. 163-172, 2017.
- [9]. Alexandru P., Ștefănescu C., *Experimental Determination of the Kuczynski Equation for the Case of CuSn12 Alloy Sintering*, Ann. "Dunarea Jos" Univ. Galati. Fascicle IX, Metall. Mater. Sci., vol. 45, no. 4, p. 81-86, doi: 10.35219/mms.2022.4.13, 2022.
- [10]. Demian C., Nicoară M., Vida-Simiti I., *Esențial în Metalurgia Pulberilor*, Cluj-Napoca, U.T. Press, 2009.
- [11]. Taloi D., Florian E., Bratu C., Berceanu E., *Optimizarea proceselor metalurgice*, București, Editura Didactică și Pedagogică, 1983.

MANUSCRISELE, CĂRȚILE ȘI REVISTELE PENTRU SCHIMB, PRECUM ȘI ORICE
CORESPONDENȚE SE VOR TRIMITE PE ADRESA:

MANUSCRIPTS, REVIEWS AND BOOKS FOR EXCHANGE COOPERATION,
AS WELL AS ANY CORRESPONDANCE WILL BE MAILED TO:

LES MANUSCRIPTS, LES REVUES ET LES LIVRES POUR L'ECHANGE, TOUT AUSSI
QUE LA CORRESPONDANCE SERONT ENVOYES A L'ADRESSE:

MANUSKRIPTEN, ZIETSCHRIFTEN UND BUCHER FUR AUSTAUCH SOWIE DIE
KORRESPONDENZ SIND AN FOLGENDE ANSCHRIFT ZU SEDEN:

After the latest evaluation of the journals by the National Center for Science Policy and Scientometrics (**CENAPOSS**), in recognition of its quality and impact at national level, the journal will be included in the B⁺ category, 215 code (http://cncsis.gov.ro/userfiles/file/CENAPOSS/Bplus_2011.pdf).

The journal is already indexed in:

DOAJ: <https://doaj.org/>

SCIPIO-RO: <http://www.scipio.ro/web/182206>

EBSCO: <http://www.ebscohost.com/titleLists/a9h-journals.pdf>

Google Academic: <https://scholar.google.ro>

Index Copernicus: <https://journals.indexcopernicus.com>

Crossref: <https://search.crossref.org/>

The papers published in this journal can be viewed on the website:
<http://www.gup.ugal.ro/ugaljournals/index.php/mms>

Name and Address of Publisher:

Contact person: Prof. Dr. Eng. Elena MEREUȚĂ
Galati University Press - GUP
47 Domneasca St., 800008 - Galati, Romania
Phone: +40 336 130139
Fax: +40 236 461353
Email: gup@ugal.ro

Name and Address of Editor:

Ș. L. Dr. Eng. Marius BODOR
"Dunarea de Jos" University of Galati, Faculty of Engineering
111 Domneasca St., 800201 - Galati, Romania
Phone: +40 336 130208
Phone/Fax: +40 336 130283
Email: marius.bodor@ugal.ro

AFFILIATED WITH:

- **THE ROMANIAN SOCIETY FOR METALLURGY**
- **THE ROMANIAN SOCIETY FOR CHEMISTRY**
- **THE ROMANIAN SOCIETY FOR BIOMATERIALS**
- **THE ROMANIAN TECHNICAL FOUNDRY SOCIETY**
- **THE MATERIALS INFORMATION SOCIETY**
(ASM INTERNATIONAL)

**Edited under the care of
the FACULTY OF ENGINEERING
Annual subscription (4 issues per year)**

Fascicle DOI: <https://doi.org/10.35219/mms>

Volume DOI: <https://doi.org/10.35219/mms.2024.1>

Editing date: 15.03.2024

Number of issues: 200

Printed by Galati University Press (accredited by CNCSIS)
47 Domneasca Street, 800008, Galati, Romania